Potential vorticity and moisture in extratropical cyclones: climatology and sensitivity experiments

Dissertation
zur Erlangung des Grades
”Doktor der Naturwissenschaften”

am Fachbereich Physik, Mathematik und Informatik
der Johannes Gutenberg-Universität
in Mainz

Jana Čampa
geb. in Kranj, Slowenien

Mainz, August 2012

1. Gutachter:
2. Gutachter:

Tag der mündlichen Prüfung: 13.8.2012

D77 – Mainzer Dissertation

Kurzzusammenfassung

Die Entwicklung außertropischer Zyklonen kann als ein Wechselspiel dreier positiver Anomalien der potenziellen Vorticity (PV) gesehen werden: die Intrusion der stratosphärischen Luft in den höheren Schichten, die diabatisch produzierte PV-Anomalie in der unteren Troposphäre und die Warmanomalie am Boden, die als Ersatz für eine positive PV-Anomalie dienen kann. Zum Zeitpunkt der maximalen Intensität überlagern sich diese drei Anomalien und bilden so einen sogenannten "PV-Turm", der mit starker zyklonaler Zirkulation verbunden ist. Dieses Modell der Entwicklung außertropischer Zyklonen stellt die Grundlage dieser Doktorarbeit dar. Sie nutzt einen klimatologischen Datensatz und numerische Modellexperimente um die Amplitude der drei Anomalien und die Prozesse zu untersuchen, die insbesondere zur Bildung der diabatisch erzeugten PV-Anomalie in der unteren Troposphäre führen.

Im ersten Teil dieser Arbeit wurde die Amplitude der drei PV-Anomalien in reifen außertropischen Zyklonen in verschiedenen Regionen der Nordhemisphäre klimatologisch quantifiziert. Dazu wurden ERA-Interim Reanalysen des Europäischen Zentrums für mittelfristige Wettervorhersage (ECMWF) verwendet. Ein Verfolgungsalgorithmus identifizierte und verfolgte die Zyklonenzugbahnen im Feld des Bodendrucks auf der Meeresoberfläche. Bodenwarmanomalien $\Delta\theta$ und vertikale Profile der PV Anomalien $\Delta\mathrm{PV}$ in einem vertikalen Zylinder mit dem Radius 200 km wurden zum Zeitpunkt der höchsten Intensität der Zyklone und in der 24 Stunden davor liegenden Intensivierungsphase berechnet. Um ihre Charakteristiken vergleichen zu können, wurden sie nach Ort (8 Regionen) und Intensität in Gruppen eingeteilt, wobei der minimale Bodendruck auf der Meeresoberfläche im Zentrum der Zyklone als Intensitätsmaß benutzt wurde. Komposite der Profile der $\Delta\mathrm{PV}$ und der $\Delta\theta$ wurden für jede Region und jede Intensitätsklasse berechnet, zum Zeitpunkt der maximalen Intensität und während der Intensivierungsphase.

Während der Zyklonenentwicklung wuchsen alle drei Amplituden im Durchschnitt. Im Reifestadium sind alle drei Anomalien größer für intensive als für schwächere Zyklonen [e.g., 0.6 versus 0.2 potential vorticity units (PVU; $1\,\mathrm{PVU} = 10^{-6}\mathrm{m}^2\mathrm{s}^{-1}\mathrm{Kkg}^{-1}$) in den unteren Schichten und 1.5 versus 0.5 PVU in den oberen Schichten]. Die regionale Variabilität der vertikalen Struktur der Zyklonen ist markant (Zyklonen verschiedener Regionen zeigen sich durch eine bestimmte Anomalie mehr beeinflusst als durch andere). $\Delta\theta$ und $\Delta\mathrm{PV}$ in der unteren Troposphäre sind im Durchschnitt größer in den westlichen als in östlichen Teilen der Ozeane. Zusätzlich wurde eine große saisonale Variabilität gefunden mit weniger und schwächeren Zyklonen, besonders im Sommer. Sie sind verbunden mit höheren PV-Werten in den unteren Schichten, höherer Tropopause und schwächeren Bodenanomalien der potenziellen Temperatur im Vergleich zum Winter.

Im zweiten Teil steht der untere, diabatische Teil des PV-Turmes im Vordergrund. Verdunstungsquellen der Feuchte, die an der PV-Produktion durch Kondensation beteiligt waren, wurden identifiziert. Lagrangesche Rückwärtstrajektorien wurden von der Region mit hohen PV-Werten im Zyklonenzentrum berechnet. Regionen der PV-Produktion wur-

den entlang der Trajektorien identifiziert und von diesen aus wurde ein neues Set der Trajektorien berechnet. Entlang dieser Trajektorien wurden Quellenregionen diagnostiziert. Der Hauptbeitrag der Oberflächenverdunstung zur spezifischen Feuchte der Trajektorien wurde 12-72 Stunden vor dem Zeitpunkt der PV-Produktion aufgenommen. Die Quellregionen für schwächere Zyklonen mit weniger PV im Zentrum sind typischerweise umliegend und kleiner und haben niedrigere Werte als für intensivere Zyklonen. Jedoch unterscheiden sich die Werte der Feuchteaufnahme und andere Variablen entlang einzelner Trajektorien nicht stark für unterschiedlich starke Zyklonen verschiedener Regionen.

Eine Sensitivitätsstudie mit dem COSMO Modell stellt den dritten Teil dieser Arbeit dar. Die Studie untersucht den Einfluss der Veränderung der Feuchte in der Umgebung der Zyklone in verschiedenen Stadien der Entwicklung. In drei Regionen wurde Feuchte entzogen, die vorher als Quellregionen für die PV-Produktion definiert wurden. Die Eliminierung der Feuchte hatte den größten Effekt in der frühesten Phase der Zyklonenentwicklung. Sie führte kurz nach der Entstehung der Zyklone zur Zyklolyse. Eine neue Zyklone entstand auf der anderen Seite der trockenen Box, entwickelte sich relativ schnell und ersetzte die primäre Zyklone. Auch in anderen Experimenten führte die Eliminierung der Feuchte zu starker Reduktion der Intensivität der Bodenzyklone, beschränkter Entwicklung an der Tropopause und verspäteter oder ausgebliebener Wechselwirkung zwischen den beiden.

Diese Arbeit bietet eine neue Sicht auf die Struktur außertropischer Zyklonen mit unterschiedlichen Intensitätskategorien aus der PV-Perspektive, die die Erkenntnisse vorangehender Fallstudien bestätigt. Sie macht deutlich, dass alle drei PV-Anomalien in intensiveren Zyklonen typischerweise größer sind mit wichtigen regionalen Unterschieden die relative Amplitude der drei Anomalien betreffend. Die Analyse der Feuchtequellen ist die erste solche Untersuchung des Verdunstungs-Kondensations-Kreislaufs in Bezug auf die Intensivierung außertropischer Zyklonen. Interessanterweise geschieht die meiste Verdunstung während der drei Tage vor dem Zeitpunkt der maximalen Zyklonenintensität und ist typischerweise über ein relativ großes Gebiet entlang der Zyklonenzugbahn ausgebreitet. Die Fallstudie mit einem numerischen Modell ergänzt diese Untersuchung durch die Analyse des Einflusses regional begrenzter Feuchtequellen für die Zyklonenentwicklung.

Abstract

The development of extratropical cyclones can be seen as an interplay of three positive potential vorticity (PV) anomalies: an upper-level stratospheric intrusion, low-tropospheric diabatically produced PV, and a warm anomaly at the surface acting as a surrogate PV anomaly. In the mature stage they become vertically aligned and form a "PV tower" associated with strong cyclonic circulation. This paradigm of extratropical cyclone development provides the basis of this thesis, which will use a climatological dataset and numerical model experiments to investigate the amplitude of the three anomalies and the processes leading in particular to the formation of the diabatically produced low-tropospheric PV anomaly.

The first part of this study, based on the interim ECMWF Re-Analysis (ERA-Interim) dataset, quantifies the amplitude of the three PV anomalies in mature extratropical cyclones in different regions in the Northern Hemisphere on a climatological basis. A tracking algorithm is applied to sea level pressure (SLP) fields to identify cyclone tracks. Surface potential temperature anomalies $\Delta\theta$ and vertical profiles of PV anomalies $\Delta\mathrm{PV}$ are calculated at the time of the cyclones' minimum SLP (t_0) and during the intensification phase 24 hours before t_0 in a vertical cylinder with a radius of 200 km around the surface cyclone center. To compare the characteristics of the cyclones, they are grouped according to their location (8 regions) and intensity, where the central SLP is used as a measure of intensity. Composites of $\Delta\mathrm{PV}$ profiles and $\Delta\theta$ are calculated for each region and intensity class at the time of minimum SLP and during the cyclone intensification phase.

During the cyclones' development stage the amplitudes of all three anomalies increase on average. In the mature stage all three anomalies are typically larger for intense than for weak winter cyclones [e.g., 0.6 versus 0.2 potential vorticity units (PVU; $1\,\mathrm{PVU} = 10^{-6}\mathrm{m^2s^{-1}Kkg^{-1}}$) at lower levels, and 1.5 versus 0.5 PVU at upper levels]. The regional variability of the cyclones' vertical structure and the profile evolution is prominent (cyclones in some regions are more sensitive to the amplitude of a particular anomaly than in other regions). Values of $\Delta\theta$ and low-level $\Delta\mathrm{PV}$ are on average larger in the western parts of the oceans than in the eastern parts. In addition, a large seasonal variability can be identified, with fewer and weaker cyclones especially in the summer, associated with higher low-tropospheric PV values, but also with a higher tropopause and much weaker surface potential temperature anomalies (compared to winter cyclones).

In the second part, we were interested in the diabatic low-level part of PV towers. Evaporative sources were identified of moisture that was involved in PV production through condensation. Lagrangian backward trajectories were calculated from the region with high PV values at low-levels in the cyclones. PV production regions were identified along these trajectories and from these regions a new set of backward trajectories was calculated and moisture uptakes were traced along them. The main contribution from surface evaporation to the specific humidity of the trajectories is collected 12-72 hours prior to the time of PV production. The uptake region for weaker cyclones with less PV in the centre is typically more localized with reduced uptake values compared to intense cyclones.

However, in a qualitative sense uptakes and other variables along single trajectories do not vary much between cyclones of different intensity in different regions.

A sensitivity study with the COSMO model comprises the last part of this work. The study aims at investigating the influence of synthetic moisture modification in the cyclone environment in different stages of its development. Moisture was eliminated in three regions, which were identified as important moisture source regions for PV production. Moisture suppression affected the cyclone the most in its early phase. It led to cyclolysis shortly after its genesis. Nevertheles, a new cyclone formed on the other side of a dry box and developed relatively quickly. Also in other experiments, moisture elimination led to strong intensity reduction of the surface cyclone, limited upper-level development, and delayed or missing interaction between the two.

In summary, this thesis provides novel insight into the structure of different intensity categories of extratropical cyclones from a PV perspective, which corroborates the findings from a series of previous case studies. It reveals that all three PV anomalies are typically enhanced for more intense cyclones, with important regional differences concerning the relative amplitude of the three anomalies. The moisture source analysis is the first of this kind to study the evaporation-condensation cycle related to the intensification of extratropical cyclones. Interestingly, most of the evaporation occurs during the 3 days prior to the time of maximum cyclone intensity and typically extends over fairly large areas along the track of the cyclone. The numerical model case study complements this analysis by analyzing the impact of regionally confined moisture sources for the evolution of the cyclone.

Contents

Chapter 1

Introduction

Extratropical cyclones are the most important actors in determining daily weather in mid-latitudes due to strong wind and intense precipitation that is typically associated with them. Therefore understanding of their structure and dynamics is of great importance for providing a reliable weather forecast. The objective of this thesis is to contribute to an improved understanding of cyclone dynamics, in particular of the interaction of the cyclone evolution and the associated moist processes, by performing diagnostic and numerical modeling studies. In the following sections, a brief overview is given on the state-of-the-art of climatological cyclone analyses, on the dynamics of cyclogenesis, and on the potential vorticity (PV) perspective, which will be extensively used in this thesis. At the end of this introductory section, the main objectives of this thesis will be briefly outlined.

1.1 Cyclone climatologies and climatologies of their characteristics

Several recent climatological studies deal with extratropical cyclones and their properties. Most of them present regions of enhanced cyclone track density and regions of cyclone genesis or lysis (e.g., Whittaker and Horn 1984; Hoskins and Hodges 2002; Wernli and Schwierz 2006). Although using different methods of cyclone identification and tracking, they all found some pronounced features such as, e.g., the North Atlantic and the North Pacific storm tracks and a secondary maximum of cyclone frequency over the Gulf of Genoa.

Some climatological studies also consider other cyclone characteristics such as cyclone size, intensity, propagation velocity, asymmetry (e.g., Simmonds and Keay 2000; Gulev et al. 2001; Rudeva and Gulev 2007; Lim and Simmonds 2007; Rudeva 2008), or associated precipitation (Chang and Song 2006; Field and Wood 2007; Rudeva and Gulev 2011). The latter studies found the maximum of precipitation immediately to the northeast of the cyclone centre. Chang and Song (2006) investigated North Pacific and North Atlantic cyclones and found large seasonal differences in the amount of precipitation.

North Pacific cyclones have the highest amount of precipitation in fall and the lowest in summer, but the spatial extent of precipitation around the cyclone is the largest in winter. Comparisons between seasons show that the differences are largest in the area of highest precipitation rate. North Atlantic cyclones are slightly weaker and have also all in all less precipitation. The maximum is approximately equal in fall and winter and weaker in spring and summer. The differences are equally distributed over the whole cyclone area. Field and Wood (2007) composited cyclones according to their intensity (in terms of surface wind speed) and moisture content. They show that for the cyclones of the same wind speed intensity, those with more moisture have a slightly higher SLP than the drier ones. Therefore the dynamical effect of precipitation processes is to produce stronger winds also in cyclones with not very low SLP. Also Rudeva and Gulev (2011) found a similar distribution of precipitation in North Atlantic cyclones of different intensity. They also combined cyclones according to the stage of the lifecycle and showed that precipitation is particularly strong in the front part of the cyclones (i.e., in the region where the cyclone is moving to) during the first half of the lifecycle, and is reduced rather rapidly after the cyclone enters the decaying phase. They also found differences in the precipitation pattern in cyclones in different regions in the North Atlantic. Besides precipitation they also investigated the distributions of the surface heat fluxes, heat content and precipitable water in North Atlantic cyclones. Recently Mass and Dotson (2010) considered the structure of the strongest cyclones in the Northwest USA. They found the strongest winds south-east of the cyclones and interestingly a cold temperature anomaly at 850 hPa in the centre. A bent-back warm front was found to be a typical feature of these storms.

Considering the structure of extratropical cyclones is also an important aspect when evaluating climate model simulations. Bauer and Del Genio (2006) and Catto et al. (2010) compared composites of extratropical cyclones in general circulation models (GCMs) with those from ERA-40 reanalyses. Bauer and Del Genio (2006) found fewer, weaker and more slowly moving cyclones in their GCM. In addition, vertical velocities were underestimated, which has consequences on the evolution of water vapour, clouds and precipitation associated with extratropical cyclones. Catto et al. (2010) evaluated a higher resolution GCM and found that the general structure of the 50 strongest cyclones in the North Pacific and the North Atlantic in the GCM compared well with those in ERA-40, although the vertical velocity and relative humidity were not very well represented. This indicates that the realistic representation of intense extratropical cyclones is still challenging for present-day climate models.

A key element for the dynamical understanding and classification of extratropical cyclones is their vertical structure. Classically, cyclones develop along the leading edge of a pronounced upper-level trough moving over an intense baroclinic zone leading to a westward tilt with height of the axis of minimum geopotential or of the axis connecting the surface warm anomaly with the upper-level potential vorticity (PV) anomaly (Hoskins et al. 1985). Early studies emphasized this role of large-amplitude upper-level disturbances and made use of satellite imagery to investigate the structure of cyclones (see, e.g., the review by Reed 1990). Later, with the focus shifting to studying rapidly intensifying ex-

tratropical cyclones, low-level processes (e.g., thermal advection and surface fluxes) were also considered essential for understanding the evolution and structure of the storms (e.g., Uccellini 1990). Comparatively little attention has been paid so far to investigating the climatology of the vertical PV structure of extratropical cyclones. Wang and Rogers (2001) first presented composite vertical structures of PV and wind speed for explosively deepening cyclones in the North Atlantic. They showed an upper-level anomaly approaching before the deepening phase and a low-level PV generation shortly before the cyclones attain maximum intensity. At the time when both anomalies are developed, they create a coherent cyclonic circulation around the centre from the tropopause all the way to the surface. This aspect of the generation of vertically coherent "PV towers" will be discussed in detail in Chapter 3. Lim and Simmonds (2007) investigated cyclone characteristics on different levels between sea level and 500 hPa in the Southern Hemisphere. In their study vertically well organized cyclones are larger, deeper, and last longer than shallow systems. Most of the cyclones have a westward tilt in their mature stage and the surface centre and the centre at 500 hPa are 300 km apart. They found especially explosive cyclones to be vertically well organized, with a slightly larger tilt than for "normal" cyclones, which assists in releasing baroclinic energy in favor of the development of these cyclones. However, these explosive cyclones reach their maximum intensity earlier at the surface than at 500 hPa, which highlights the importance of surface fluxes, diabatically produced positive PV anomalies and reduced static stability for the rapid development.

Deveson et al. (2002) classified 16 cyclones from the FASTEX field experiment according to the contributions of the forcing from upper and lower levels to the vertical motion (expressed by the U/L ratio) and their vertical tilt. In addition to previously known type A and type B cyclones (Petterssen and Smebye 1971), they identified a new category of type C cyclones. These are strongly upper-level dominated cyclones with an increasing tilt during the development phase and an intense cloud condensational processes. Gray and Dacre (2006) applied this classification to a larger set of cyclones. They found that cyclones with a small upper- to lower-tropospheric forcing ratio (U/L) and higher values of low-level vorticity are more likely to be developing cyclones. Another detailed climatology of North Atlantic cyclones by Dacre and Gray (2009) showed that most developing cyclones are generated over the sea, which may be because of the availability of a moisture source and of reduced friction compared to continental regions. Their study also showed that the cyclones generated in the eastern North Atlantic have lower SLP and higher relative vorticity in the centre at the time of genesis than western North Atlantic cyclones, but the latter start in an environment with a stronger horizontal SST and wet-bulb potential temperature gradient. They found that PV at a height of 1 km at the time of maximum cyclone intensity is higher for cyclones generated in the western North Atlantic and their U/L ratio is lower throughout their life cycle than for eastern North Atlantic cyclones.

The next sections summarize the theoretical background on cyclogenesis, potential vorticity and on the influence of moist processes on extratropical cyclone development.

1.2 Cyclogenesis

Baroclinic instability (Charney 1947, Eady 1949) is considered the basic mechanism responsible for the genesis and growth of extratropical cyclones. It states that midlatitude weather systems grow as a consequence of an intrinsic instability of baroclinic atmospheres, as indicated by the exponential growth of the most unstable wave (normal mode). The analytical solution of the so-called "Eady problem" (atmosphere of uniform baroclinicity sandwiched between a horizontal surface and tropopause) shows the fastest growing mode to have a wave length of approximately 4000 km, which corresponds to the typical wavelength of surface high and low pressure systems in the atmosphere.

The Eady model considers a strongly simplified representation of the atmosphere, which enables an analytical solution. In order to introduce additional complexity to the problem, several idealized modelling studies were performed investigating normal mode growth of more realistic baroclinic atmospheres (i.e., jet-like flows) (e.g., Hoskins and West 1979, Davies et al. 1991, Thorncroft et al. 1993). Their solutions actually resemble the basic structure of extratropical cyclones. These solutions however did not develop fast enough to be able to describe explosive cyclogenesis. Farrel (1982, 1984) suggested a different approach (initial value problem) to investigate baroclinic growth. He used an initial perturbation consisting of a continuous spectrum of waves including normal modes (as opposed to using only normal modes). He showed that an initial perturbation in this setup can grow much faster than the normal mode alone (proper phasing is important). This led to the use of localized, finite amplitude initial perturbations (e.g., an upper-level trough) to trigger baroclinic instability in idealized simulations, which typically precede cyclogenesis in the real atmosphere. This approach was used by, e.g., Warrenfeltz and Elsberry (1989), Schär and Wernli (1993), and Wernli et al. (1998).

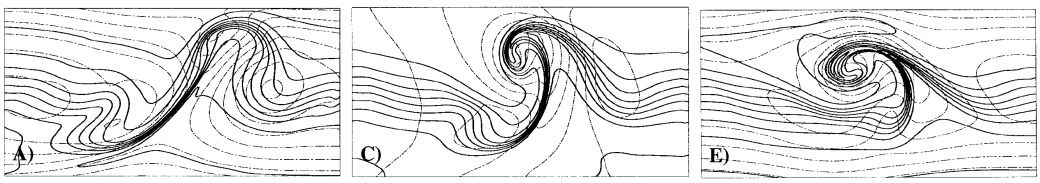

Figure 1.1: The surface flow evolution at day 4 for simulations with a symmetric baroclinic jet (middle) and with additional barotropic anticyclonic shear (left) and cyclonic shear (right). Solid lines represent insentropes (contour interval 2.1 K) and dash-dotted lines the pressure distribution at the surface (contour interval 6.5 hPa). Figure from Wernli et al. (1998).

Considering the detailed structure and evolution of cyclones and their attendant fronts, it turned out that the meridional asymmetry of the basic state baroclinic jet (barotropic wind shear) plays an important role. Davies et al. (1991), Thorncroft et al. (1993), and Wernli et al. (1998) showed radically different results when adding cyclonic or anticyclonic barotropic shear to a symmetric basic state jet. Figure 1.1 shows surface flow pat-

terns after four days of integration for simulations with differing basic state wind shear. In the case with a symmetric jet a cyclone develops with two accompanying anticyclones up- and down-stream. Both surface fronts are well developed. The simulation with additional anticyclonic shear produces a very pronounced cold front southwest of a weak cyclone and two strong anticyclones. With cyclonic shear a cyclone develops with similar intensity as in the unsheared case. A faster propagation of the cold front towards the warm front results in an occlusion process.

1.3 Diabatic processes in cyclones

We have seen in the previous section that already highly idealized dry simulations are able to produce structures similar to those found in real weather systems. These studies confirm the essential role of baroclinicity for cyclogenesis. However, there is strong evidence in the literature that diabatic processes (especially latent heating due to condensation) can accelerate the deepening. Already early case studies emphasized the presence of moisture in rapid cyclogenesis (Manabe 1956, Bosart 1981, Anthes et al. 1983, Gyakum 1983a,b, Rogers and Bosart 1986). They suggested that latent heat release in combination with baroclinic processes can lead to rapid cyclone deepening. The climatological study of Roebber (1984) showed that rapidly deepening cyclones develop differently from weaker cyclones and suggested that in addition to baroclinic instability another mechanism has to be involved in explosive cyclogenesis.

Latent heat release leads to stronger vertical motion in cyclones through reduction of stability (Martin 2006). Lower stability enables a greater response to a given large-scale forcing for upward motion. Most explosively deepening cyclones in the northern hemisphere occur over warm ocean currents in the western parts of the oceans (Roebber 1984). These regions are characterized by lower static stability. Furthermore, latent heat release adds energy into an evolving system. It can also modify the PV distribution and produce positive PV anomalies in the lower troposphere and negative PV anomalies in the upper troposphere, as discussed in more detail below.

The effect of moisture on cyclone development has been studied in idealized model studies as well as observational studies. Theoretical studies with linear and nonlinear models and different representations of latent heating have shown that condensational heating results in an increased growth rate and a reduced scale of the most unstable wave (Mak 1982, Emanuel et al. 1987, Whitaker and Davis 1994). Figure 1.2 shows a comparison between the baroclinic developments in a dry and moist simulation. Inclusion of moist processes results in stronger cyclone deepening and frontogenesis. Both fronts are much more narrow in the moist simulation and especially the warm front is very intense. This goes along with very strong lifting of air along the warm front. Whitaker and Davis (1994) also performed simulations with a localized initial perturbation and found that the rapid growth started earlier than in the normal mode simulations, however the rate was very similar. A faster development in the presence of moisture was also confirmed recently by

Lambaerts et al. (2012).

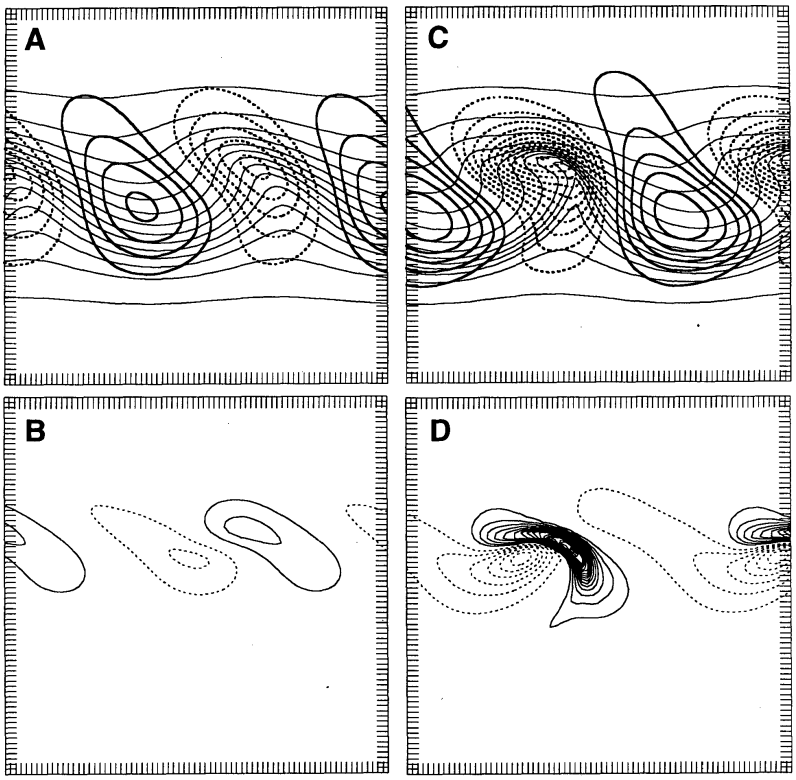

Figure 1.2: Comparison of dry (left) and moist (right) baroclinic wave simulations at day 4.5. Upper panels: surface streamfunction (thick contours, interval $2 \times 10^6\,\mathrm{m^2 s^{-1}}$) and potential temperature (thin contours, interval 2 K); Bottom panels: Vertical velocity (contour interval $0.01\,\mathrm{ms^{-1}}$). Negative contours are dashed. Figure 8 from Whitaker and Davis (1994).

Many idealized studies focused on moist effects on frontogenesis. Mak and Bannon (1984) addressed the frontogenesis problem analytically. Even in their very simple model the vertical motion along the front was strongly enhanced and concentrated in a smaller region by including latent heating. It also caused a faster propagation of the cold front. Hsie et al. (1984) found a stronger temperature gradient and stronger ageostrophic circulation at the surface cold front in a moist simulation with a two-dimensional model compared to a dry simulation. The vertical motion and precipitation pattern in the warm sector showed a banded structure, a feature that was not present in the dry simulation. Similarly to Mak and Bannon (1984), the propagation speed of the surface cold front was increased due to convection. This was confirmed also by Baldwin et al. (1984), Dudhia (1993), Reeves and Lackmann (2004). Xu (1988, 1990) found strong influence of moist processes on cyclogenesis, especially at the warm front and rapid deepening of a cyclone in a moist region. The vertical motion and frontal circulation were enhanced in the moist region. The ascent was nearly vertical along the cold front and slantwise along the warm

front. They suggested systematic studies of the sensitivity of frontogenesis to the moisture distribution. Similar results were also found by Balasubramanian and Yau (1994, 1996) for idealized simulations of explosive cyclogenesis, who additionally found a bent-back warm front as a typical feature of explosive development. However, Balasubramanian and Yau (1996) claimed that the dynamics of the moist cyclone is very similar to the dry cyclone, but enhanced, which diminishes the importance of nonlinearity which was stressed in some other studies. Frontogenesis and cyclogenesis are concurrent processes (Martin 2006), therefore the influence of latent heat release on both has to be accounted for.

Gyakum (1983b) tried to quantify the dynamical effects of latent heating on the development of the Queen Elizabeth II storm. They found heating to be responsible for a large part of the warming in the cyclone core, low-level PV production and explosive deepening. Using an idealized vertical profile of latent heating he showed that the height of the heating is important, the same amount of heating produces different vertical motion rates at different heights. The strongest vertical motion was driven by the heating with maximum amplitude at 700 hPa. Anthes et al. (1983) confirmed the influence of the vertical distribution of latent heating through simulations with different initial conditions.

Kuo et al. (1991), for the same storm, found latent heating directly contributing to the warming of air at the warm side of the front, which accelerated frontogenesis. Additionally, diabatically induced vertical motion caused the low-level cross-frontal convergence which reinforced the low-level frontogenesis. They also suggested that the vertical motion associated with latent heat release could act in phase with the secondary circulation arising from rapid (adiabatic) frontogenesis, thereby providing a positive feedback mechanism. Their results indicated that effects of latent heating should not be treated as a linear addition to the adiabatic dynamics, but rather account for strong nonlinear interaction between dry dynamics and diabatic processes.

Kuo et al. (1991) and others already employed potential vorticity (PV) as a key variable in their studies. This variable is very suitable for investigating the dynamics of midlatitude weather systems. The PV concept is briefly introduced in the next subsection and then further studies will be presented and discussed, which consider the influence of diabatic processes in terms of PV.

1.4 PV view

1.4.1 Definition and properties

Since the seminal study of Hoskins et al. (1985), PV has been established as the key variable to study large- and synoptic-scale atmospheric flows, which enables a fruitful view of dynamical processes. It has been used in many studies on cyclogenesis. The PV concept allows to combine dynamic and thermodynamic characteristics of weather systems. It is defined as (Ertel 1942):

$$PV = \frac{1}{\rho}\vec{\eta} \cdot \nabla\theta,$$

where ρ is air density, $\vec{\eta}$ the absolute vorticity vector and Θ potential temperature. For synoptic-scale systems, the equation can be simplified as:

$$PV \simeq \frac{1}{\rho}(f+\zeta)\frac{\partial\theta}{\partial z}.$$

Here f stands for the Coriolis parameter and ζ for the vertical component of the relative vorticity. PV is therefore mainly a product of vorticity (kinematic component) and static stability (thermodynamic component). PV is expressed in PV units (PVU), where $1\,\mathrm{PVU} = 10^{-6}\mathrm{m}^2\mathrm{s}^{-1}\mathrm{Kkg}^{-1}$. Typical values in the troposphere are about 0.5 PVU. PV values in the startosphere are much higher due to strong stratification. The 2 PVU isoline is often defined as the dynamical tropopause. This definition is also used in this work.

Three fundamental principles characterize PV:

- **Conservation**

  PV is conserved in an adiabatic and frictionless flow:

  $$\frac{D}{Dt}PV = 0$$

  Under these conditions an air parcel moves on isentropic surfaces and represents a passive tracer. These conditions are usually fulfilled in the upper troposphere and lower stratosphere.

- **Invertibility**

  The PV distribution in the atmosphere contains all information about the associated balanced flow. Balanced wind and temperature fields can be deduced, provided that boundary conditions, balance conditions defining the relation between the wind, temperature and pressure field, and a reference state are known.

- **Partition**

  The three-dimensional PV distribution can be decomposed into isolated PV anomalies. An anomaly can be defined as a deviation from the climatological value, from balanced background flow in the vicinity of the system or a difference between two model simulations. The associated flow and temperature field can be inferred for each component separately. Thus the contribution of different processes contributing to the flow can be assesed via PV inversion of each anomaly and their mutual interaction.

Figure 1.3 shows wind and potential temperature fields of inverted positive PV anomalies at different levels. A positive PV anomaly is always associated with a cyclonic wind field around it and reduced static stability above and below. The isentropes above and below the PV anomaly are therefore bent towards the anomaly (e.g., Fig. 1.3b). Hoskins et al. (1985) showed that also a positive potential temperature anomaly at the surface can be

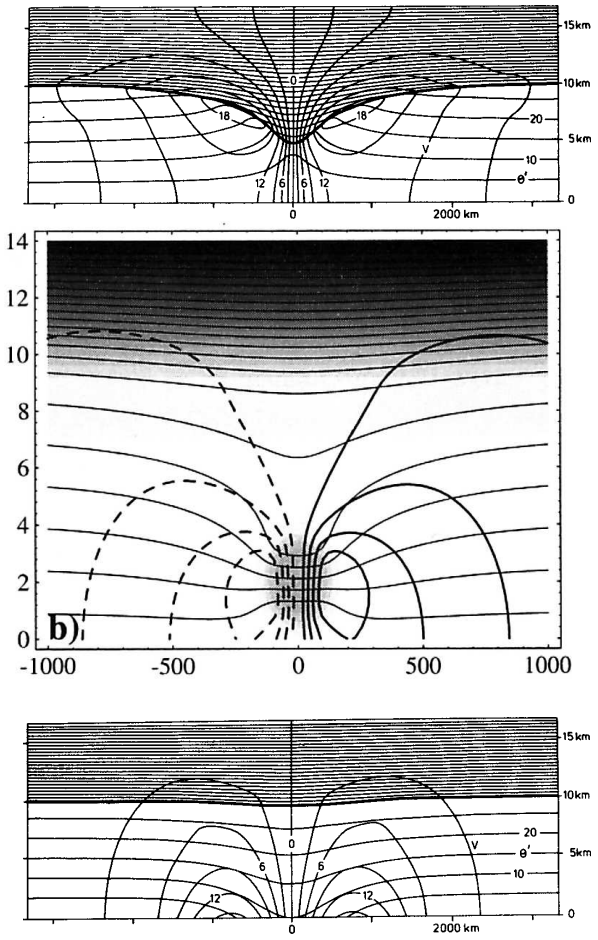

Figure 1.3: Potential temperature and horizontal wind field associated with a positive PV anomaly at the tropopause (above), in the lower troposphere (middle), and at the surface (in the form of a boundary positive potential temperature anomaly; bottom). The stratosphere is represented by very dense isentropes. Horizontal lines denote isentropes and circular lines represent the induced velocity field. Top and bottom panels are from Thorpe (1986), and the middle panel is from Fehlmann (1997).

regarded as a positive PV anomaly (Fig. 1.3c). In analogy to an electric charge (Bishop and Thorpe 1994) a PV anomaly has a far-field effect, i.e., the effects of the PV anomaly seen in the circulation and temperature fields extend over a much larger region than the anomaly itself. Its reach is determined by the so-called Rossby penetration depth, which depends on static stability. In the troposphere the anomaly field reaches further than in the more stably stratified stratosphere (Fig. 1.3a).

In electrostatics theory, the principle of superposition can be used to calculate the electric field of several charges (Bishop and Thorpe 1994). Analogously, a superposition of three PV anomalies is shown here in Fig. 1.4. A superposition of several anomalies results in a stronger and larger anomalous wind and temperature field. As seen in Fig. 1.4,

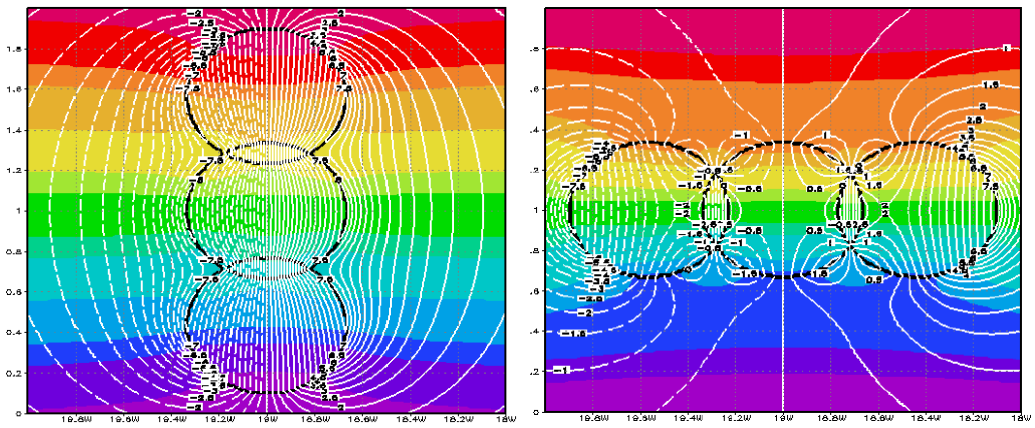

Figure 1.4: Similar to 1.3 for a superposition of several PV anomalies. After Thorpe (1986), courtesy Sarah Jones.

the vertical superposition of PV anomalies affects in particular the wind field and the horizontal superposition the temperature field. The wind anomaly associated with a PV anomaly is largest at the level of the anomaly, while the temperature field is disturbed most strongly above and below the PV anomaly.

In the presence of diabatic processes (latent heating, friction, radiation, ...) PV is no longer materially conserved. The material change of PV can be expressed as:

$$\frac{DPV}{Dt} = \frac{1}{\rho}\vec{\eta}\cdot\nabla\dot{\Theta} + \frac{1}{\rho}(\nabla\times\vec{F})\cdot\nabla\Theta.$$

The equation introduces two sources of PV: a frictional force $\vec{F}$ and diabatic heating $\dot{\Theta}$. The friction term is negligible in the free atmosphere. The diabatic term in the troposphere is primarily due to latent heating due to cloud microphysical processes. In the diabatic term, the third component of the scalar product is typically the largest, therefore the change of PV can be written approximatively as

$$\frac{DPV}{Dt} \sim \frac{1}{\rho}(f+\zeta)\frac{\partial\dot{\Theta}}{\partial z}.$$

PV is produced in regions with a positive vertical gradient of diabatic heating, i.e., underneath the maximum of diabatic heating. Above the maximum of latent heating, PV is destroyed. This is shown schematically in Fig. 1.5a. In the presence of vertical motion the air with PV production is advected upwards so that the positive PV anomaly is located approximately at the location of maximum latent heating in a cloud (Fig. 1.5b). Analogously, further lifting air advects the negative PV tendency to upper levels and influences the PV distribution there.

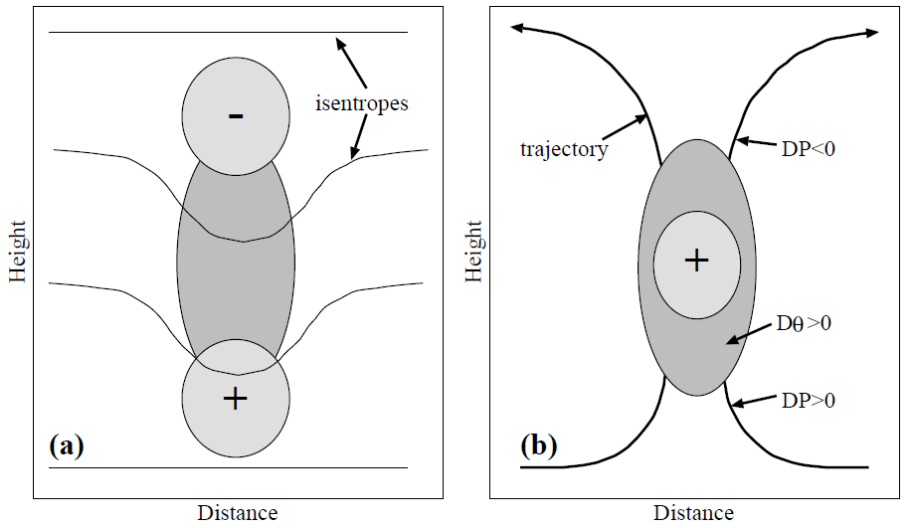

Figure 1.5: Schematic vertical cross-sections through diabatically produced PV anomalies. Shown are latent heating (dark shading) and the resulting positive and negative PV anomalies (light shading) for a) "impulsive diabatic heating" and b) "steady condensation". Figure 4 from Wernli and Davies (1997).

1.4.2 PV view of cyclogenesis

From the PV point of view, cyclogenesis can be seen as a result of superposition and mutual reinforcement of upper- and lower-level PV anomalies. A typical situation in the atmosphere is shown schematically in Fig. 1.6, taken from Hoskins et al. (1985). An upper-level positive PV anomaly (a trough; a southward deflection of a Rossby wave) arrives over a low-level baroclinic zone. The PV anomaly induces cyclonic rotation at low levels, which advects warm air from the south and creates a warm anomaly downstream of the upper-level anomaly. As we have seen in Fig. 1.3c, this warm anomaly acts as a positive PV anomaly. It induces its own corresponding cyclonic circulation and intensifies the upper-level anomaly, which in turn (via its own induced wind field) intensifies the low-level anomaly. This mutual interaction and growth results in the amplification of the cyclone. As long as the two anomalies are in a proper phase, they will continue to intensify each other (e.g., Hoskins et al. 1985, Davis and Emanuel 1991, Huo et al. 1999).

When moisture comes into play in this process, it enhances the interplay of these two anomalies. Condensation in moist rising air in the region of reduced stability below an upper-level positive PV anomaly further reduces the stability in the region. Therefore the Rossby penetration depth and the contribution of both anomalies to circulation increase. Diabatic heating hence leads to a tighter coupling between the upper and lower levels and thereby to more intense development (Hoskins et al. 1985). As seen above, PV is produced in the presence of condensational processes in the lower troposphere. Stoelinga (1996) showed for a case of an intense Atlantic cyclogenesis that the low-level positive

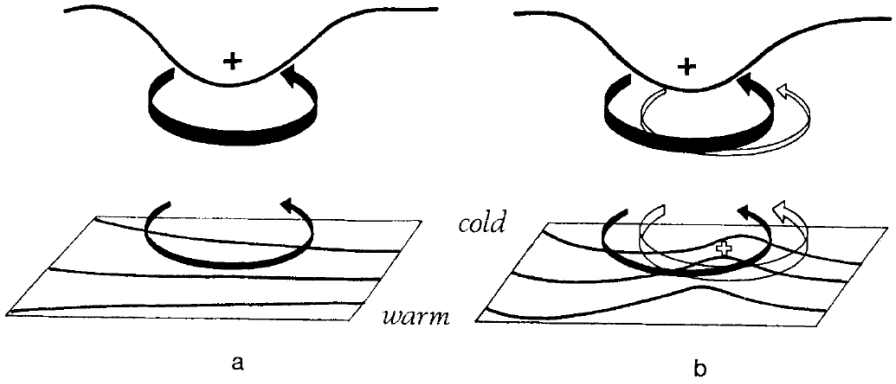

Figure 1.6: A schematic of cyclogenesis associated with the arrival of an upper-air PV anomaly over a low-level baroclinic region. Figure from Hoskins et al. (1985).

PV anomaly was produced by non-conservative diabatic processes. These low-level diabatic PV anomalies can reach a considerable magnitude in intense extratropical cyclones, sometimes more than 6 or 7 PVU. We expect that such an intense PV anomaly would significantly influence cyclone development and contribute to an intense low-level cyclonic circulation.

Several case studies highlighted the crucial role of this diabatically produced part of the PV structure for the structure and evolution of extratropical cyclones. Numerical simulations with suppressed latent heating (e.g., Uccellini et al. 1987; Kuo et al. 1991, 1995; Wernli et al. 2002) produced much weaker cyclones than the full-physics control simulations, in agreement with the fact that in these simulations the low-level PV anomaly was missing. Moist processes therefore play an important role in the evolution of (intense) extratropical cyclones.

In the mature stage of the cyclone development the three involved anomalies often become vertically aligned and form a so-called "PV tower", representing a troposphere-spanning column of air with anomalously high PV-values (typically 1-4 PVU = $10^{-6}\mathrm{m}^2\mathrm{s}^{-1}\mathrm{Kkg}^{-1}$). It induces a strong cyclonic circulation reaching from the surface to the tropopause. In this framework, cyclone formation and intensification can be regarded as the generation and interplay of these PV anomalies that form through both adiabatic (upper-level PV) and diabatic (low-level PV) processes.

Davis and Emanuel (1991) were the first to use the technique of PV inversion to study the relative contribution of the three anomalies constituting a PV tower to the overall cyclonic circulation. Each anomaly contributed to the vorticity in the lower troposphere, but the contribution of the diabatically produced low-level PV was the largest, followed by the surface potential temperature anomaly. The upper-level anomaly accounted only for a small amount of the lower-tropospheric vorticity. Davis (1992) and Davis et al. (1996) used the same method to estimate the relative contributions from different levels to the intensification of a continental and a marine cyclone, respectively. In the continental cy-

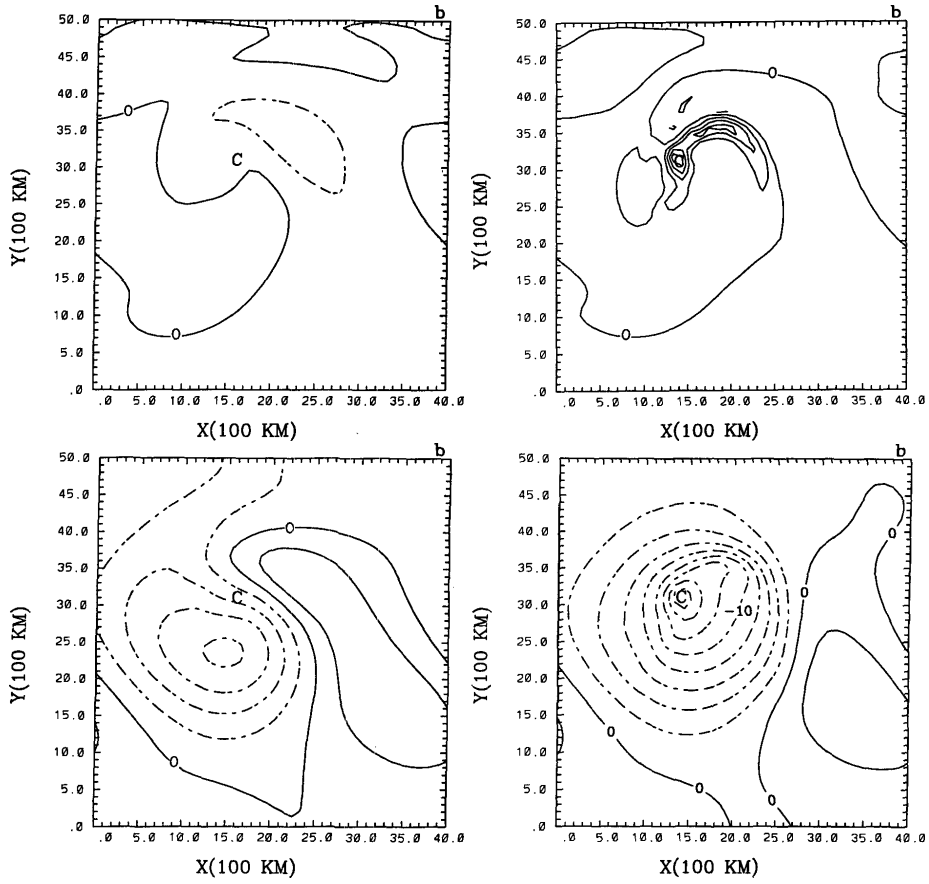

Figure 1.7: Low-level PV in dry and moist baroclinic waves. Upper panels: PV at 800 hPa in the dry (left; contour interval 0.2 PVU) and moist (right; contour interval 0.2 PVU) simulation. Lower panels: geopotential anomaly at 900 hPa (every $2\mathrm{m}^2\mathrm{s}^{-2}$) calculated via inversion of the low-level PV anomaly. The cyclone centre is denoted by the label C. Figure from Balasubramanian and Yau (1994).

clone, the largest contribution came from the surface anomaly, whereas in the marine cyclone both the tropopause-level and the low-level PV anomalies contributed more to the surface circulation than the warm surface anomaly. This indicates that because of their direct access to water, marine cyclones can typically produce a positive low-level PV anomaly sooner and more strongly than continental cyclones, which is most likely of relevance for the fact that most intense cyclones occur over the oceans (e.g., Wang and Rogers 2001; Dacre and Gray 2009). Later, several other cyclones were investigated with the piecewise PV inversion technique (e.g., Huo et al. 1999) to diagnose the horizontal and vertical interaction of the distinct PV anomalies. Besides simulations of real cyclones the method was aplied also to idealized simulations. Balasubramanian and Yau (1994) showed for an idealized marine cyclone that a large part of the intense circulation can be assigned to the diabatically produced PV. In Fig. 1.7 the low-level PV and the

corresponding inverted contribution to the geopotential at 900 hPa in a dry and moist simulation are compared. First of all, the low-level PV is almost completely missing in the dry simulation. In the moist simulation a pronounced PV anomaly can be seen directly in the cyclone centre and along the warm front. Accordingly, the corresponding perturbation of the near-surface geopotential from the low-levels is much larger than in the dry case and contributes the most to the total geopotential anomaly.

1.5 Aims and outline

The brief summary above of the state-of-the-art of extratropical cyclogenesis and the role of diabatic processes also points to a series of open questions that will be examined in this thesis. Most of the knowledge on the role of latent heating on cyclone evolution is based upon detailed case studies, typically of intense marine cyclones, and a more climatological investigation is missing. Therefore, this work will adopt a PV perspective to investigate in a climatological way the vertical structure of mature extratropical cyclones and the relationship between the cyclones' vertical PV structure and their intensity and geographical region. This climatological investigation will be presented in Chapter 3. In Chapter 4 special attention is payed to the diabatic part of PV in the cyclone centre. Using a recently developed Lagrangian diagnostic, sources of moisture are identified that are involved in the production of low-level PV. Finally, the methodology from these two chapters will be combined in order to study a case of explosive cyclogenesis in Chapter 5 to test the sensitivity of the cyclone to modified humidity in its environment with the aid of a mesoscale model.

Chapter 2

Data and tools

2.1 Data and models

2.1.1 ECMWF

The main part of this work is based on the ERA-Interim dataset (Dee et al. 2011a), the latest global reanalysis dataset from the ECMWF (European Centre for Medium-range Weather Forecasts). It is a successor of the well-known ERA-40 reanalysis and is an intermediate step on the way to a new long term atmospheric reanalysis planned at ECMWF.

Analyses are appreciated as the best approximation of the real state of the atmosphere. They are produced as a combination of observations and a short range model forecast to achieve global coverage, which is not possible with observations only. Since weather models and data assimilation systems develop constantly, operational analyses cannot offer a consistent dataset for climatological investigations. Reanalyses are computed using state-of-the-art data assmilation systems including all available observations over a longer time perid and present the most comprehensive and consistent data set at the moment. Of course, availability and density of observations changes through time (e.g., satellite observations) which produces inhomogeneous time series. However, this problem applies also when using only observational data. Much progress has been made in data assimilation to address this issue (Dee et al. 2011b, Dee and Uppala 2009).

ERA-Interim data are available since 1979 and are continuously updated in near real-time. At the beginning of this study data from 1989 till 2009 was available and this time period is used in the study. ERA-Interim is produced using cycle 31r2 of ECMWF's IFS (Integrated Forecast System) with the spectral resolution T255 for the basic dynamic fields and a reduced N128 Gaussian grid with the resolution of approximately 79 km for other fields. The model uses the hybrid Σ vertical coordinate with 60 levels. Observational data is included by a 4D-var assimilation technique with a 12 hour window (ECMWF 2007). The most important improvements for this study compared to ERA-40 are the use of 4D-var instead of 3D-var technique, a revised humidity analysis and improved representation of the hydrological cycle.

The reanalysis data are available every 6 hours. The original fields were interpolated onto a $1^\circ \times 1^\circ$ regular grid.

2.1.2 COSMO

Model simulations in Chapter 5 were performed with the COSMO model (Steppeler et al. 2003). It is a non-hydrostatic limited-area numerical weather prediction model initially developed at the German Weather Service (DWD) and now further developed and supported by the COnsortium for Small-scale MOdelling (COSMO, more information at www.cosmo-model.org). Here COSMO version 4.18 from May 2011 has been used. Model description in the following is based on COSMO documentation (Doms and Schättler 2002, Doms et al. 2005)

a) Model equations

The basis of the COSMO model are the primitive thermo-hydrodynamical equations in advection form describing compressible flow in a moist atmosphere. The thermodynamic variables are divided into a height dependent basic state and a time dependent deviation. The basic state is a horizontally homogeneous, vertically stratified dry atmosphere at rest and in hydrostatic balance.

Prognostic variables include all three wind components, temperature and pressure perturbations, as well as specific humidity and cloud water content and other liquid and frozen moist variables. Diagnostic equations take care of all other variables, such as total air density, precipitation fluxes of rain and snow, 2 m temperature, etc.

b) Numerical Implementation

The equations are reformulated in geographical coordinates with a non-varying generalised terrain following vertical coordinate. The differential operators are spatially discretised using second-order centered finite differences. The model variables are calculated on an Arakawa-C grid with Lorenz vertical grid staggering (Arakawa and Lamb 1981). All scalar variables (e.g., temperature) are calculated at the centre of a grid box and vector variables (wind components) on the corresponding cell faces, halfway between the grid points.

Spherical coordinates cause problems due to convergence of the meridians towards the poles. COSMO uses rotated spherical coordinates to avoid too strong variations in the size of grid boxes. The pole is displaced such that the equator crosses the model domain. The rotated grid together with external data (e.g., topography, soil type, roughness length,...) was provided by DWD.

The time integration was carried out with a variant of a 3rd order two time-level Runge-Kutta split-explicit scheme (Wicker and Skamarock, 2002). The time splitting allows for separate handling of high- and low-frequency modes and therefore enhances

computing efficiency. A time step $\Delta t = 40\,s$, which is also used operationally, is used for the slow modes. A time step for the fast propagating waves is calculated automatically inside the program.

c) Model physics

With current computer ressources not all relevant processes on the whole range of scales can be resolved. These processes (especially subgrid processes such as cloud microphysics, turbulence, radiation, surface fluxes,...) are treated by parameterization schemes.

In our model configuration, grid-scale precipitation is represented by a Kessler-type bulk water continuity formulation including cloud water and cloud ice, rain and snow. Formation of clouds is controlled by a saturation adjustment technique: when a grid box becomes supersaturated, temperature, water vapour and cloud water are adjusted to a saturated state, i.e., the surplus of water vapour condenses. The subgrid–scale cloud formation is parametrised by an empirical function depending on relative humidity and height and the sub-grid moist convection is parameterised by the Tiedtke mass-flux convection scheme (Tiedtke 1989). Turbulence and surface fluxes are based on the turbulent kinetic energy closure.

d) Initial and Boundary data

Regional models need initial and boundary data provided by a host model to incorporate larger scale processes outside the model domain. This information is provided by the ECMWF's IFS and interpolated on the COSMO grid. Boundary conditions are updated every 6 hours to ensure consistency with the large scale flow. They are applied through a lateral boundary relaxation scheme (Davies 1976) to avoid numerical noise.

2.2 Tools

2.2.1 Cyclone identification and tracking

To collect information on cyclone position, intensity and area a cyclone tracking algorithm was applied. Although manual tracking is possible, the large amount of data requires the use of an objective numerical tracking algorithm.

Several cyclone tracking algorithms were developed and used in climatological studies (Raible et al. 2008 and references therein). Identification methods use either geopotential height at 1000 hPa, SLP or (smoothed) low-level vorticity field or a combination of them. Also the tracking methods differ. Some define the cyclone position at the next time step as the position of the closest neighbour, other use a prediction and matching method or a variational method.

In this work, we use the method introduced by Wernli and Schwierz (2006) to derive a cyclone climatology for the Era-40 reanalysis. It uses SLP field for the cyclone identifi-

cation and a prediction-matching method for cyclone tracking. In the first step, it searches for all local minima in a SLP field. To call a certain point a minimum, all neighbour points must have higher SLP values. No additional criteria are applied to the search for minima. Further, the program determines the outermost closed contour that encloses only one minimum. The closed contour search proceeds from the centre (with a value of p_0 in steps of Δp. All the points with the SLP value of p_0 + Δp comprise a polygon of points around the centre (line $C_{1,1}$ in Fig. 2.1). The contour following algorithm proves whether the last point found along the contour is close enough to the starting point. If the last point is closer to the starting point than to the previous one, the closed contour is found. The search continues along points with SLP values of p_0 + 2Δp, and continues untill it reaches an open contour or another minimum is found inside of the contour. The area enclosed by the outermost closed contour is defined as the cyclone. The same procedure is repeated for all minima and only the minima which are enclosed by at least one closed contour count as cyclones.

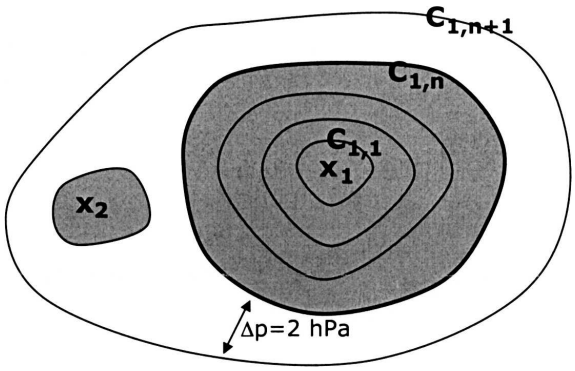

Figure 2.1: Schematic representation for the cyclone identification procedure. Figure 1 from Wernli and Schwierz (2006).

In the second step, the tracking algorithm connects matching minima at subsequent time steps into cyclone tracks. At the first time step, the algorithm links two sufficiently nearby points at subsequent times. For all further steps the first guess for the new cyclone position is calculated as a reduced linear continuation of the track in the previous step: $x(t_{n+1}) = x(t_n) + 0.75 \cdot (x(t_n) - x(t_{n-1}))$. The minimum closest to the first guess is taken as the continuation of the track, if the distance does not exceed a certain threshold D. If more minima fullfil the vicinity criterion D the nearest one is chosen to extend the track. The factor of 0.75 accounts for slowing down of the cyclone propagation during its life cycle.

Here, we used the same parameter values as Wernli and Schwierz (2006), i. e., D=1000 km and Δp = 2 hPa.

Input data for trajectory calculation is available every 6-hours in ERA-Interim, and every hour for COSMO simulations.

2.2.2 LAGRANTO

The Eulerian approach, based on spatially fixed coordinates, is a suitable framework to investigate different synoptic phenomena, e.g., cyclones, anticyclones and fronts. However, the system that moves with the flow is physically more meaningful since it gives an insight to the material changes in an air parcel. The Lagrangian approach enables us to follow the changes in the characteristics of air parcels along their path.

Trajectories in the investigated systems in this study were calculated using the trajectory model LAGRANTO (LAGRangian ANalysis TOol, Wernli and Davies 1997). It is a three-step method: In the first step trajectories that originate in a previously defined domain are calculated over a certain time period using the three dimensional wind field. Afterwards, additional variables are interpolated onto the trajectory positions. In the third step, a set of trajectories is selected according to selection criteria.

The position of an air parcel in a subsequent time step is calculated by a predictor-corrector method. The first guess for the new position at time $n+1$ is estimated using the wind field at time n: $\vec{r}^{*n+1} = \vec{r}^{n} + \vec{v}(\vec{r}^{n}) \cdot \Delta t$. This position is then corrected in an iterative process using the mean of the wind fields at times n and $n+1$: $\vec{r}^{*} = \frac{1}{2}[\vec{v}(\vec{r}^{n}) + \vec{v}(\vec{r}^{*n+1})]$. The wind at the intergrid locations is obtained by linear interpolation. The trajectory time step Δt equals one twelfth of the data time step, hence 30 min for ERA-Interim and 5 min for COSMO data. Backward trajectories are calculated analogously.

In the next step, specific criteria are applied to the set of trajectories to reduce the number of trajectories and select only those that are of interest for the investigation. Three types of selection criteria are implemented. A priori criteria are based upon physical properties of the air parcels at the initial time, e.g., the value of PV or relative humidity at the beginning of the trajectory. A posteriori criteria consider the position and physical properties of air parcels along the path, e.g., ascent or descent larger than a certain threshold or a certain change of a chosen variable. The third option is a combination of these criteria.

Lagrangian backward and forward trajectories are applied in this study to trace the history of the air parcels with high PV values in the cyclone centre and to identify moisture uptake regions in chapter 4, and to investigate streams of lifting air in the vicinity of cyclones in chapter 5.

2.2.3 Moisture uptake diagnostics

In chapter 4 and 5 moisture source regions for PV production in extratropical cyclones are identified. We used a Lagrangian diagnostic introduced by Sodemann et al. (2008). The script and support were provided by Stephan Pfahl (ETHZ). Its advantage compared to other methods is that it does not only find moisture sources but also accounts for moisture loss by precipitation along trajectories.

Moisture sources along a trajectory are diagnosed by the change of specific humidity q within one trajectory time step $\Delta q(t) = q(\vec{x}(t)) - q(\vec{x}(t-6h))$. Δq is a net result of evaporation and precipitation in a 6h interval, hence a negative Δq is a consequence

of precipitation and a positive Δq implies evaporation. In this way, all moisture uptakes along trajectories are detected until the trajectory is almost dry or the end of the trajectory is reached.

In the troposphere many mixing processes take place where moisture is involved. This method only considers exchange processes in the boundary layer, because only these can be assigned to the evaporation from the surface. The sources of other moisture increases above the boundary layer are more difficult to identify and can come from a variety of physical and numerical processes, such as convection, evaporation of precipitating hydrometeors, subgrid-scale turbulent fluxes, numerical diffusion, numerical errors associated with the trajectory calculation, or physical inconsistencies between two ECMWF analysis time steps (Sodemann et al. 2008a). In order to reduce the possibility of including uptakes due to numerical noise, only uptakes where $\Delta q > 0.2$ g/kg in 6 hours are considered.

In Fig. 2.2 the method is demonstrated graphically. The thick black line represents the air parcel trajectory. It goes through several evaporation-precipitation cycles. The first two moisture uptakes (at t = -48h and -36h) take place in the boundary layer and the third one (at t = -18h) above.

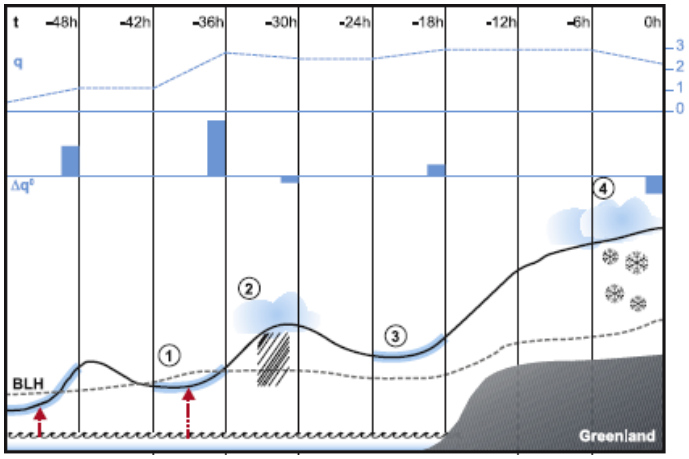

Figure 2.2: Schematic of the method for identifying moisture uptakes along a backward trajectory of an air parcel on the way from the Atlantic ocean to Greenland (black line). Time before arrival is given at the top. q (dashed line): specific humidity in the air parcel (g/kg); Δq^0: changes in specific humidity of an air parcel between two time intervals; BLH: boundary layer height. Thick blue sections along the trajectory denote sections of moisture increase, and red arrows point to identified evaporation locations. Figure 1 from Sodemann et al. (2008).

When all uptake locations along trajectories are identified and stored, the method has an option of assigning weights to each uptake. This way, it can evaluate a relative contribution of each uptake to the moisture in the air parcel at the end of the trajectory. Namely, each new uptake reduces the importance of a previous uptake and after each precipitation

event, earlier sources will relatively contribute less to the moisture at the end (a lesser percent of moisture at the end). Also each uptake above boundary layer reduces the weight of all previous uptakes. However, our goal was to assess the total amount of moisture in the air parcels at the location of PV production, therefore the calculation of relative contributions was opted out, only moisture reduction due to precipitation was considered. Each moisture uptake Δq was reduced proportionally to the amount of precipitation from the air parcel after the uptake.

Moisture uptake data are finally gridded onto a $1^\circ \times 1^\circ$ grid with the latitudinal correction. From these fields composite moisture uptake regions were calculated for the cyclones in the specified regions.

Chapter 3

PV tower climatology

3.1 Introduction

From a PV point of view, mainly three distinct positive PV anomalies determine the evolution of an extratropical cyclone: an upper-level stratospheric intrusion, a low-tropospheric diabatically produced PV anomaly, and a warm surface anomaly of potential temperature (θ) that corresponds to a positive PV anomaly (e.g., Davis and Emanuel 1991; Kuo et al. 1991). A positive PV anomaly at the tropopause moves over a region of enhanced baroclinicity at the surface and induces formation of the surface anomaly. They intensify through the mutual interaction. The presence of the diabatically produced low-level PV anomaly intensifies this interaction. When vertically aligned in a mature cyclone, these anomalies form a PV tower, a structure often found in intense extratropical cyclones.

Several studies of rapidly deepening extratropical cyclones found such a pronounced PV tower in the center of the cyclone, for example case studies of the "October storm" (Hoskins and Berrisford 1988), the "Presidents' Day Cyclone" (Uccellini et al. 1987; Whitaker et al. 1988), the "Superstorm of 1993" (Dickinson et al. 1997), and the winter storm "Lothar" (Wernli et al. 2002). A very recent example is the North Atlantic cyclone "Xynthia" that led to extreme winds in Western Europe on 27/28 February 2010. Figure 3.1 shows vertical cross-sections of PV through the centres of the mature cyclones "Superstorm", "Lothar" and "Xynthia", respectively. The fields shown are calculated from ERA-Interim reanalyses from the European Centre for Medium-Range Weather Forecasts (ECMWF). In all cases we can distinguish two distinct PV features: one at upper levels of stratospheric origin and one at low levels that has been diabatically produced. PV values at lower levels reach up to more than 3 PVU, which is much higher than climatological tropospheric values of about 0.5 PVU. The corresponding surface θ anomalies are given in Table 3.1 together with the amplitude of the upper-level and lower-level anomalies, calculated as the vertical average between 200 and 400 hPa, and 650 and 900 hPa, respectively. The anomalies, $\Delta\mathrm{PV}$ and $\Delta\theta$, are defined as a deviation from the climatological value at the same location. All variables are averaged within a circle with a radius of 200 km around the cyclone. All three storms have a low-level PV anomaly in approxi-

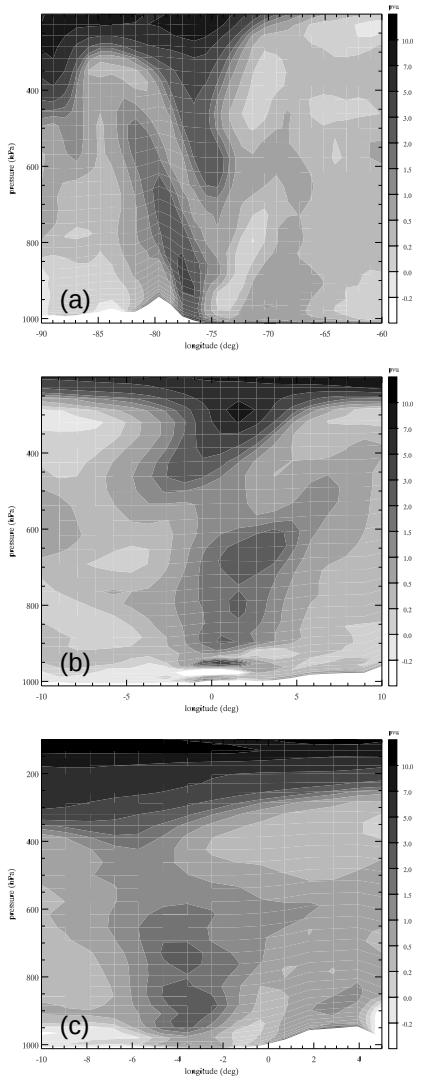

Figure 3.1: West-east oriented vertical sections of PV (in PVU) across the centre of three mature extratropical cyclones for a) the "Superstorm of 1993" at 39°N at 00 UTC 14 March 1993, b) "Lothar" at 49°N at 06 UTC 26 December 1999, and c) "Xynthia" at 46°N at 00 UTC 28 February 2010.

mately the same range. The anomaly in "Lothar" seems to be weaker, but this is due to the fact that the maximum of a low-level PV anomaly lies above the averaging interval. The surface anomaly of the "Superstorm" is clearly smaller than of "Lothar" and "Xynthia", but its upper-level anomaly is particularly pronounced. These examples illustrate on the one hand the presence of the three aforementioned PV anomalies in intense cyclones, and on the other hand indicate a significant case-to-case variability in the relative importance of the three anomalies.

Table 3.1: Upper-level ΔPV (vertical average between 200 and 400 hPa, in PVU), low-level ΔPV (vertical average between 900 and 650 hPa, in PVU), and surface $\Delta\theta$ (in K) for the three mature cyclones shown in Fig. 1.

	ΔPV (200-400 hPa) [PVU]	ΔPV (650-900 hPa) [PVU]	surface $\Delta\theta$ [K]
"Superstorm"	3.14	1.16	2.76
"Lothar"	1.13	0.79	5.24
"Xynthia"	0.99	1.13	6.60

All these storms were extremely strong and caused considerable damage and casualties. However, a PV tower is also a typical feature of most "normal" mature cyclones. Rossa et al. (2000) investigated the life cycle of such a PV tower associated with a North Atlantic cyclone that developed from a frontal wave disturbance. Using a Lagrangian analysis technique they found that the high PV air constituting the tower came from three separate regions: An adiabatic intrusion of stratospheric air at upper levels, a mid-tropospheric component originating from diabatically produced PV along the cold front, and a low-tropospheric component due to diabatic PV production in an airstream moving along the prominent warm front. A similar study of Reed et al. (1992) considered also the surface thermal anomaly. They found that the surface anomaly was primarily caused by northward transport of warm air into the vicinity of the cyclone. Similarly to the study of Rossa et al. (2000), the upper-level high-PV air subsided from the stratosphere and the low-level positive anomaly resulted from condensational PV production during the rapid ascent of air at the warm front.

This study will investigate the vertical PV structure of mature extratropical cyclones and the amplitude of the surface potential temperature anomaly on a climatological basis in the Northern Hemisphere, for all four seasons. A comprehensive set of cyclones will be investigated to address the following four main questions:

1. Is there a difference in the vertical structure between strong and weak mature extratropical cyclones (where cyclone intensity will be measured in terms of minimum SLP)?

2. Are there any structural differences between mature extratropical cyclones in different regions?

3. How does the PV profile typically evolve during the intensification of extratropical cyclones?

4. How do PV profile characteristics vary between different seasons?

The answers to these questions will shed light on the relative importance of the processes involved in the formation of mature cyclones.

3.2 Data and Methods

3.2.1 Data and cyclone tracking

This study is based upon the ERA-Interim Dataset from 1989 to 2009. The data are available every 6 hours. The original fields were interpolated onto a $1^\circ \times 1^\circ$ regular grid and the PV field was calculated from the wind and temperature fields on the model levels and then interpolated on a stack of pressure levels (every 25 hPa between 1000 and 100 hPa).

The cyclones were identified and tracked using the algorithm introduced by Wernli and Schwierz (2006). For the description of the method see Section 2.2.

3.2.2 Calculation of PV profiles

For every cyclone track, vertical profiles of PV anomalies ($\Delta\mathrm{PV}$) and potential temperature anomalies at the surface ($\Delta\theta$) were calculated for each time step during the 24 hours before the cyclone reached its minimum SLP. If a cyclone's track prior to reaching its minimum SLP is shorter than 24 hours, then only the available time steps were considered. Anomalies were defined as deviations from a climatological background value at the same location, taken as the 21-year ERA-Interim seasonal average (DJF, MAM, JJA, SON). At each point of the 24-hour cyclone track interval and at all levels between 975 and 100 hPa, PV was horizontally averaged in a circle with a radius of 200 km around the cyclone centre. The resulting values at each level (every 25 hPa) constitute the cyclone's PV profile at the given time. Horizontal averaging has been done in order to obtain a robust measure of PV in the cyclone center. Accordingly, anomalies of potential temperature at the surface were calculated within circles with a radius of 200 km around each cyclone. The choice of this particular radius will be shortly commented on in the results section. For the climatological investigation composites were computed from the individual $\Delta\mathrm{PV}$ profiles and $\Delta\theta$ at the surface for different categories of cyclones and during different stages of the cyclone evolution. The categories are based upon cyclone intensity (measured in terms of minimum SLP) and the cyclones' geographical position.

3.2.3 Intensity measure

There is no single definition of cyclone's intensity. Several authors use very different intensity measures. They are based either on SLP, low-level relative vorticity or wind speed, etc. In climatological studies the first two options are the most common. However, using the low-level relative vorticity as intensity measure is not very useful in our case because of the small-scale structure and inhomogeneity of its field in extratropical cyclones. When using SLP, several options are possible: measuring intensity by central SLP (e.g., Mass and Dotson 2010), SLP deviations from climatology (Simmonds and Wu 1993, Chang and Song 2006), difference between the SLP in the centre and on the last closed contour (Rudeva 2008), SLP gradient (Schubert et al. 1998, Trigo et al. 1999), Laplacian of

the SLP field or cyclone depth (Simmonds and Keay 2000, Lim and Simmonds 2007) or a multivariate approach - combinations of several other measures (Bauer and del Genio 2006). We shortly want to comment on some of them and explain our choice of using a simple approach and considering the SLP minimum as a measure for cyclone intensity.

Figure 3.2 shows us a climatological distribution of SLP. The features are reminiscent of the well known storm tracks. In the regions with high cyclone frequency also the climatological SLP is low. Therefore, if we used deviations of SLP from climatological mean as an intensity measure, the cyclone intensity would be underestimated in these regions.

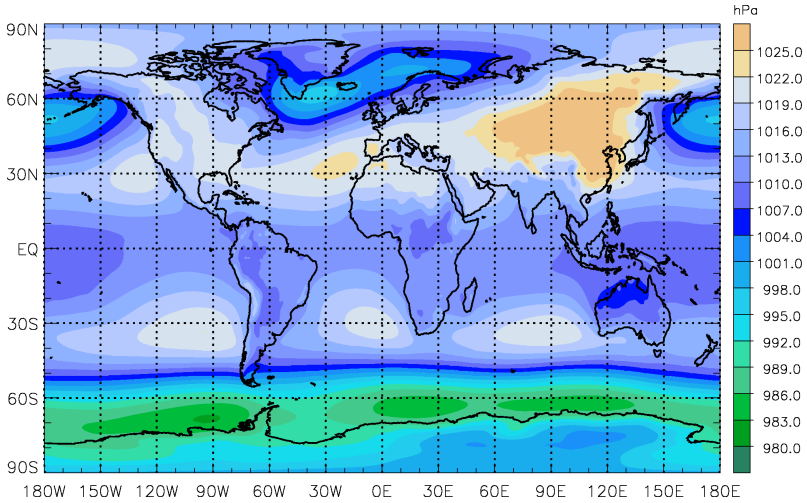

Figure 3.2: SLP climatology for winter months (DJF) in ERA-Interim data.

We compared three potential intensity measures in more detail: minimum central SLP (referred to as SLPmin), maximum difference between the central SLP and the SLP on the last closed contour (SLPdiff) and maximum average gradient of SLP in the cyclone (SLPgrad; defined as SLPdiff divided by average radius of the area enclosed by the outermost closed contour). The statistical analysis was done using all identified Northern Hemisphere winter (DJF) cyclones in the ERA-Interim dataset between 1989 and 2009. Fig. 3.3 shows the distribution of time lags between the maximum intensities measured by these variables. In almost 30 % of all cyclones the times coincide and the rest is equally distributed in both directions. However, some time lags are large, up to $\pm$ 180 hours. This artefact might appear in SLPdiff because of merging and splitting of the cyclones which suddenly changes SLP difference and cyclone radius, or because a cyclones moves into a region with different background SLP. The splitting or merging of cyclones often occurs close to the time when they reach the minimum central SLP. Another cause for the time lag between the SLPmin and the SLPgrad could be the size of cyclones at the beginning and the end of their lifecycle. At these points they are usually small and a smaller radius leads to a larger gradient. Interestingly, the time lags between the SLPmin and SLPdiff and between the SLPmin and the SLPgrad are often far apart for the same cyclone, some-

times the one long before and the other long after the SLP minimum. The time lags are relatively evenly distributed between the cyclones with different SLPmin.

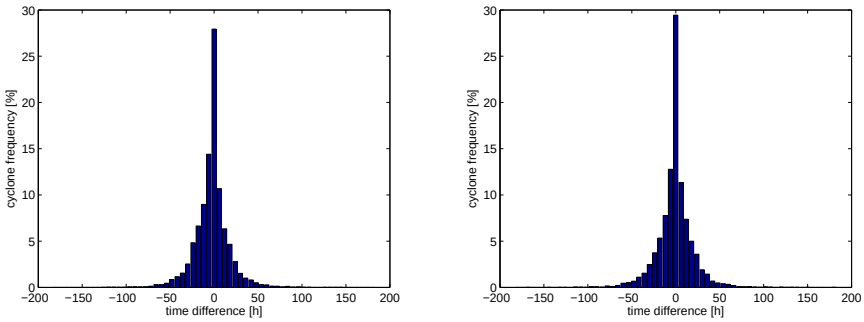

Figure 3.3: Time lag between the time of maximum intensity for a) SLPmin and SLPdiff and b) SLPmin and SLPgrad.

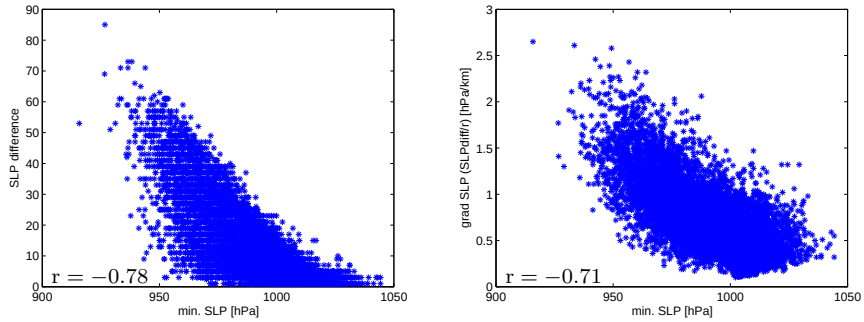

Figure 3.4: Comparison between the intensities calculated with different methods: a) SLPmin vs. SLPdiff, b) SLPmin vs. SLPgrad.

In Fig. 3.4 we compare the intensities calculated with different methods (time lags are accounted for!). The agreement between the methods is quite high. The correlation coefficients for the two pairs of intensity measures are -0.78 between SLPmin and SLPdiff and -0.71 between SLPmin and SLPgrad. In a similar analysis, Trigo et al. (1999) found the correlation coefficient of -0.63 between minimum central SLP and SLP gradient (defined as change of SLP per 100 km) for all Mediterranean cyclones in their reanalysis dataset. However, the points where the two intensity measures do not agree again make clear that the definition of cyclone intensity is not trivial.

These issues corroborate the decision to use SLP in cyclone's centre as our intensity measure. It is not optimal because we look at cyclones in different regions, but it is the most straightforward for our needs.

3.3 Results

3.3.1 The "Superstorm of 1993"

First, as an illustrative example, we consider the PV profile around the centre of the "Superstorm of '93" at 00 UTC 14 March 1993, when the cyclone reached maximum intensity, and 12 and 24 hours prior to this time. The profiles of PV and $\Delta\mathrm{PV}$ are shown in Fig. 3.5. One day before the time of maximum intensity, the central SLP was 994 hPa (according to the ERA-Interim data) and a significant positive low-level PV anomaly was already present. Averaged PV values between 900 and 650 hPa ranged between 1.3 and 1.5 PVU, about 1.1 PVU above the climatological background value. Above this anomaly, there was a region of low-PV air between 500 and 300 hPa and the dynamic tropopause (2 PVU line) was located near 250 hPa. This indicates the absence of a stratospheric intrusion directly above the cyclone centre at this early time of the cyclone intensification. Note that the profiles are calculated vertically at the position of the surface cyclone centre and therefore stratospheric air is only considered if it comes closer than 200 km to the centre. This happened in the next 24 hours, which was also the time period of the strongest cyclone intensification. Between 00 UTC 13 March and 00 UTC 14 March the central SLP decreased by 33 hPa and reached a minimum value of 961 hPa. In this period a very pronounced stratospheric anomaly became located above the surface centre, and also the low-level PV anomaly further increased. Approaching of stratospheric air with high PV values can be seen in Fig. 3.5a as lowering of the profile (and the tropopause) and in Fig. 3.5b as lowering and growth of the upper-level anomaly, which, in the end, is largest between 200 and 300 hPa. At 00 UTC 14 March the PV values are higher than 1 PVU throughout the whole troposphere, which Rossa et al. (2000) referred to as a "PV-tower". The low-level PV values are higher than 2 PVU and the 2-PVU tropopause pressure is approximately at 550 hPa. There is a PV minimum at approximately 700 hPa, which is the consequence of the fact that the two anomalies are not perfectly vertically aligned (compare Fig. 3.1a). They are also slightly tilted and therefore not the whole anomalies lie within the averaging radius. Surface θ anomaly in the core region of the cyclone increased in this 24 hour time period from around -1 K to 2.76 K at the time of maximum intensity. Compared to other intensive extratropical cyclones, this value is not particularly high (see later). Therefore it appears that the two PV anomalies in the interior of the atmosphere are more important for the high intensity of this particular cyclone.

3.3.2 Composites of Northern Hemisphere cyclones

A similar analysis was performed for all cyclones with a minimum lifetime of 24 hours (and not lasting longer than 10 days) in the whole Northern Hemisphere. Figure 3.6 shows composite PV anomaly profiles for two intensity categories of Northern Hemisphere winter (DJF) cyclones at the time of maximum intensity. The black line represents the mean value on each level, and the interval between the 10th and the 90th percentile is shaded.

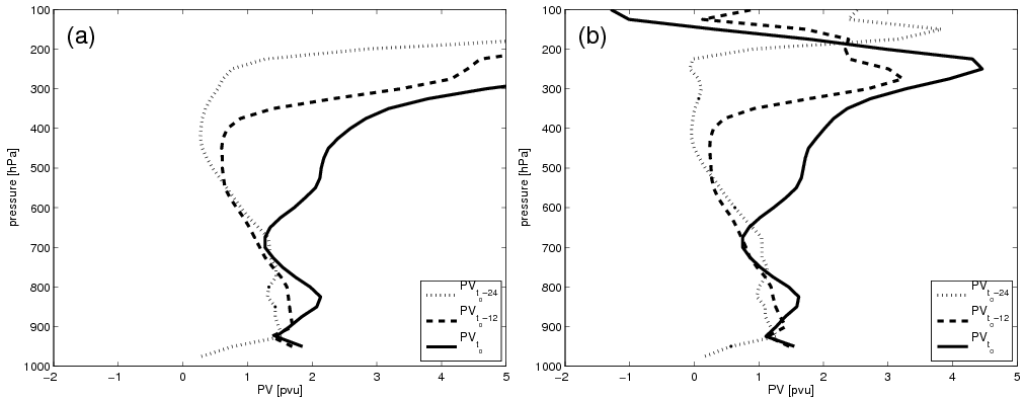

Figure 3.5: Time evolution of the vertical profile of a) PV and b) ΔPV (in PVU) averaged around the centre of the "Superstorm of 1993" at 00 UTC 13 March 1993 (dotted line), 12 UTC 13 March 1993 (dashed line), and 00 UTC 14 March 1993 (solid line).

The mean value and the percentiles are calculated on each level separately. Therefore the lines denoting the mean and the percentiles do not represent single profiles, but just connect the separately calculated values on different levels.

In the left panel the profile for 1367 intense cyclones with minimum SLP between 930 and 970 hPa is shown. The composite mean low-level PV anomaly has its maximum of 0.7 PVU at 825 hPa and the 90th percentile reaches up to 1.3 PVU. On average, PV anomalies are positive throughout the whole troposphere and higher than 0.5 on many levels. Note that climatological tropospheric PV values are approximately 0.5 PVU. The PV anomaly at upper levels is the largest at 300 hPa (2.5 PVU). In contrast, for relatively weak cyclones (4222 cyclones with a minimum SLP between 990 and 1010 hPa) shown in the right panel, the average upper level anomaly is much smaller (0.8 PVU) and the variability is larger. At the lower levels, the average PV anomaly values are about 0.3 PVU.

Surface θ anomalies are very similar for these two cyclone classes. The value for the strong cyclones on the left is 5.7 K, and for the weaker cyclones 4.91. Overall are the surface θ anomalies of the first three intensity classes very similar when we look at the average over all the cyclones in the Northern Hemisphere and only the weakest cyclones have a distinctly lower surface anomalies (see fig.3.12c).

We have calculated all these profiles using the same radius of 200 km. Figure 3.7 shows the same profiles calculated for different radii from r=100 km to r = 300 km. The smaller the radius, the larger the ΔPV values, which points to the fact, that high PV air is really concentrated in the centre of a cyclone. Differences between the profiles are only in the amplitude and not in the structure of the PV anomaly. Therefore we decided to use r=200 km, which approximately covers the spatial extent of the cyclone centre and it also does not smear the differences between the profiles.

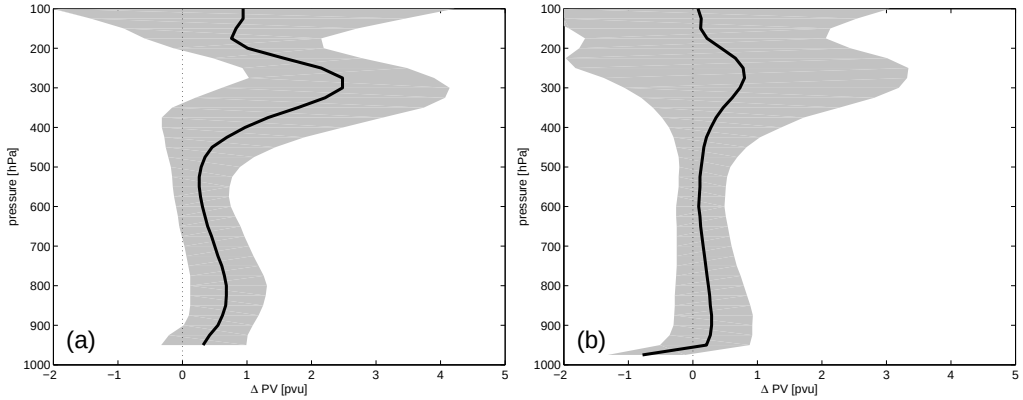

Figure 3.6: Composite PV profiles for Northern Hemisphere winter (DJF) cyclones with minimum SLP in the range of a) $930 - 970$ hPa and b) $990 - 1010$ hPa. The black line connects the mean values of PV on each level (every 25 hPa) and the shaded area marks the interval between the 10th and 90th percentile on each level.

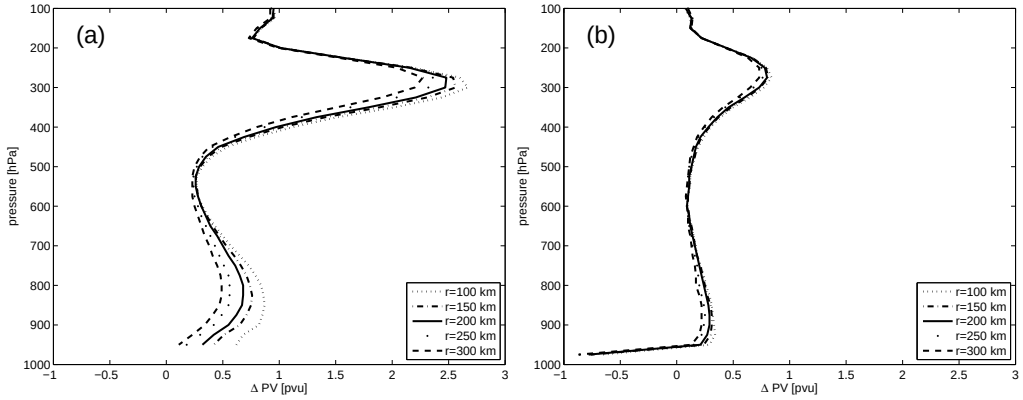

Figure 3.7: Composite ΔPV profiles for Northern Hemisphere winter (DJF) cyclones with minimum SLP in the range of a) $930 - 970$ hPa and b) $990 - 1010$ hPa for different averaging radii. Only average values at each level are shown.

3.3.3 Regional differences

In investigating the regional variability of PV profiles associated with mature cyclones we focus on the regions shown in Fig. 3.8. The regions were subjectively chosen based upon the cyclone frequency climatology of Wernli and Schwierz (2006). The cyclones are assigned to a certain region if they reach their maximum intensity within this region. Already here we notice that the number and the intensity of cyclones differ strongly between the various regions. For instance, there are relatively few cyclones that reach their maximum intensity in the western North Atlantic (referred to as Watl) and eastern North Pacific

(Epac) region, while the regions in the eastern North Atlantic (Eatl), between Greenland and Iceland (Green), and in the Gulf of Alaska (Alas) are well occupied. The strongest cyclones appear more often in the northerly regions (the tracks in Fig. 3.8 are colored with their central SLP value). The Mediterranean cyclones are quite numerous but they are much weaker compared to the cyclones in the other regions. We have found no cyclones with minimum SLP below 970 hPa in the Mediterranean. The numbers of cyclones in different regions and seasons and for various intensity categories are summarized in Table 3.2. In the continuation we only consider the categories with at least 5 cyclones to assure some statistical reliability.

Table 3.2: The number of cyclones for different regions and intensity classes.

Winter (DJF)									
	All_nh	Alas	Green	Weur	Med	Wpac	Epac	Watl	Eatl
$930 - 970$ hPa	1367	89	218	33	0	21	5	7	59
$970 - 990$ hPa	2331	144	134	64	18	47	36	23	80
$990 - 1010$ hPa	4222	49	46	75	283	92	76	54	96
$1010 - 1030$ hPa	1298	7	14	10	48	8	11	4	21
Spring (MAM)									
	All_nh	Alas	Green	Weur	Med	Wpac	Epac	Watl	Eatl
$930 - 970$ hPa	369	17	45	2	0	10	0	5	26
$970 - 990$ hPa	2175	109	131	58	14	56	13	26	79
$990 - 1010$ hPa	7370	87	75	101	311	115	51	98	136
$1010 - 1030$ hPa	483	4	26	7	10	6	5	12	23
Summer (JJA)									
	All_nh	Alas	Green	Weur	Med	Wpac	Epac	Watl	Eatl
$930 - 970$ hPa	25	1	6	1	0	0	0	0	0
$970 - 990$ hPa	1634	28	105	16	0	14	1	3	21
$990 - 1010$ hPa	9606	130	145	99	126	177	26	76	104
$1010 - 1030$ hPa	323	13	12	15	10	3	8	29	44
Autumn (SON)									
	All_nh	Alas	Green	Weur	Med	Wpac	Epac	Watl	Eatl
$930 - 970$ hPa	609	47	88	17	0	2	2	2	22
$970 - 990$ hPa	2191	151	141	56	5	16	9	13	48
$990 - 1010$ hPa	5808	71	58	100	213	77	37	54	122
$1010 - 1030$ hPa	718	2	19	7	22	10	15	13	21

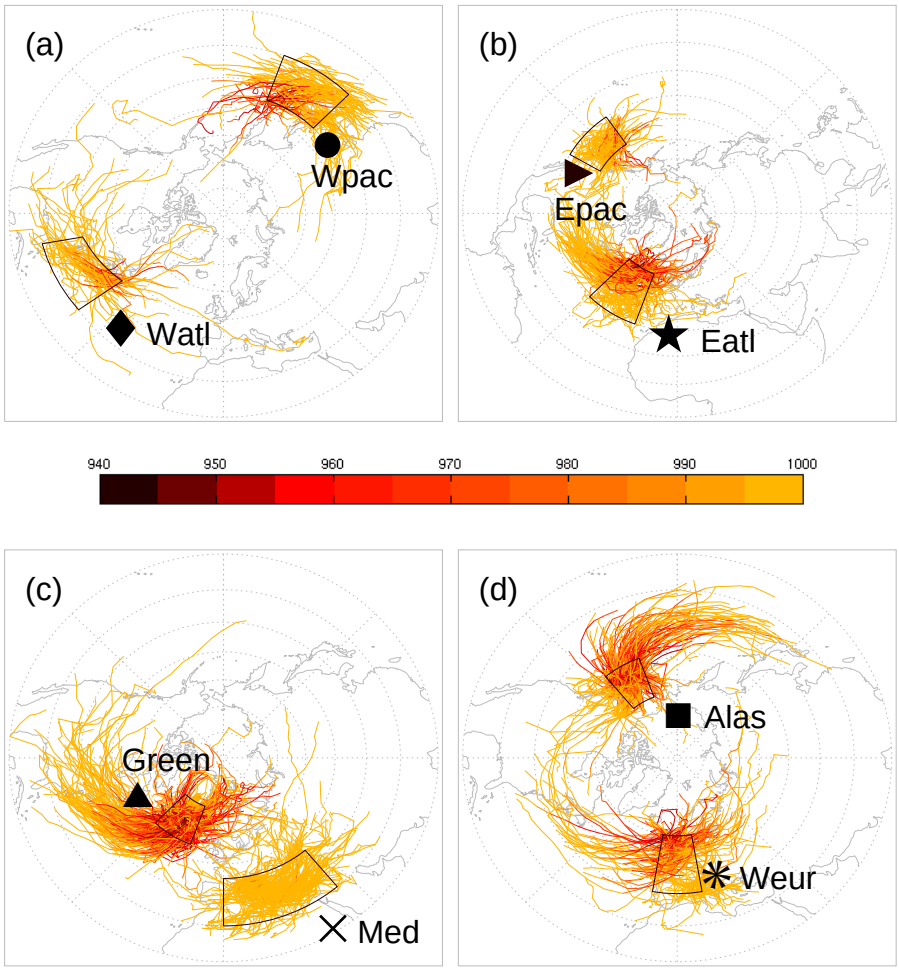

Figure 3.8: Regions where cyclone profiles have been evaluated. The symbols are used to mark cyclones from these regions in the following figures. The considered regions (see black boxes) are a) the western North Atlantic (diamond) and the western North Pacific (circle), b) the eastern North Pacific (horizontal triangle) and the eastern North Atlantic (pentagram), c) the region between Greenland and Iceland (triangle) and the Mediterranean (cross), d) the Gulf of Alaska (square) and western Europe (asterisk). Cyclone tracks are shown for all winter (DJF) cyclones that reach their minimum SLP within the specified regions. They are coloured according to their central SLP (in hPa).

In Fig. 3.9 we compare the PV profiles of cyclones in the western North Pacific and in the eastern North Atlantic, again for deep and moderately intense DJF cyclones. The most pronounced differences between the two regions occur for the strongest cyclones. While the average ΔPV values in the lower troposphere reach up to 1.5 PVU in the western Pacific, they are less than 0.7 PVU in the eastern Atlantic. In both ocean basins, cylones in the western part exhibit higher values of low-level PV than those in the eastern part (not

shown). This is consistent with the results from Dacre and Gray (2009) who found that average PV values at 1 km height in cyclones in the eastern North Atlantic are slightly lower than those in the western North Atlantic cyclones. The weaker cyclones in the two regions have on average very similar values of low-level PV.

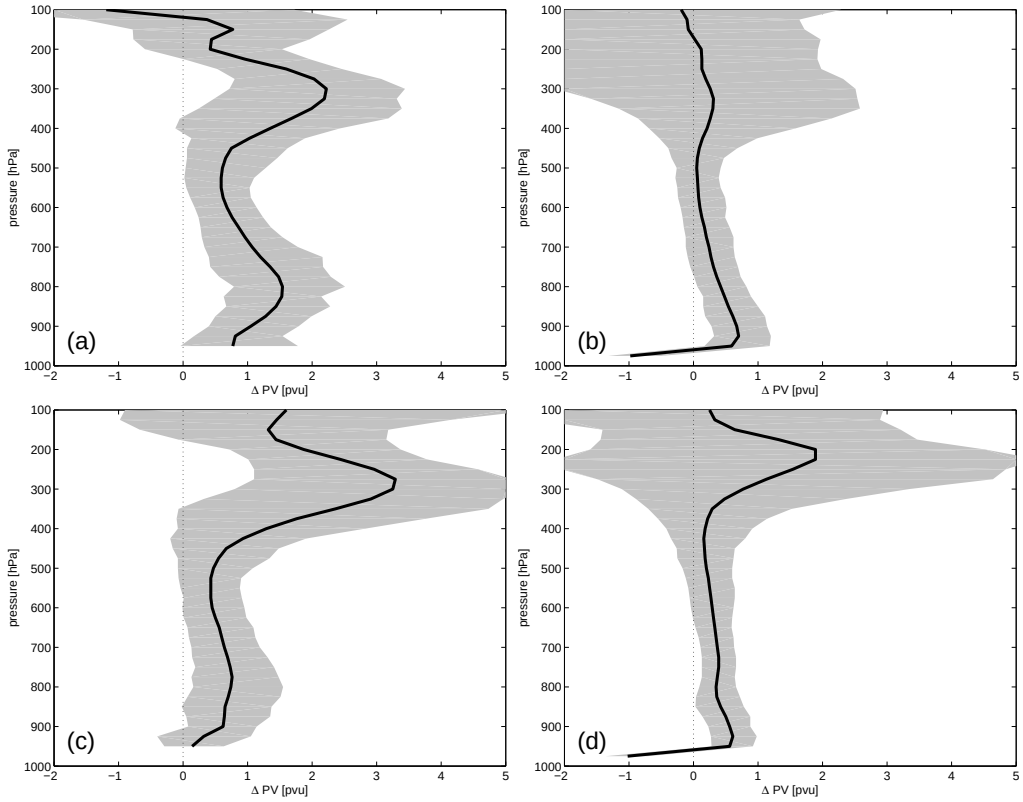

Figure 3.9: Average $\Delta\mathrm{PV}$ profiles for cyclones with a minimum central SLP in the range of (a,c) $930 - 970$ hPa and (b,d) $990 - 1010$ hPa for cyclones in (a,b) the western North Pacific and (c,d) the eastern North Atlantic. Shaded area as in Fig. 3.6.

A comparison between the upper-level anomalies in each region reveals that $\Delta\mathrm{PV}$ in the upper part of the profile differs strongly in both regions. The overall values are much higher in the eastern North Atlantic but the differences are larger in the western North Pacific. Variability of upper-level $\Delta\mathrm{PV}$ is especially large for the weaker cyclones. The shaded area ranges from -2 to 5 PVU in the eastern part of North Atlantic and in the western North Pacific it is shifted to even more negative values. This could imply that some cyclones in these regions can develop in the absence of significant upper level forcing. The height of the upper level average $\Delta\mathrm{PV}$ maximum in the eastern North Atlantic varies between 225 (weak cyclones) and 275 hPa (strong cyclones). We cannot see such a clear difference in the height of the upper-level anomaly in the western North Pacific, but the course of the 90th percentile suggests that the height is very variable for weaker cyclones

there.

Surface θ anomalies are higher in the western North Pacific but more variable in the eastern North Atlantic. Strong western Pacific cyclones are very warm with $\Delta\theta$ of 6.5 K in the centre while the anomaly in the centre of weaker cyclones reaches 4.5 K. Strong eastern Atlantic cyclones are only slightly warmer than that, their $\Delta\theta$ is 4.8 K and 2 K for the weaker cyclones (compare Fig. 3.12).

Figure 3.10 compares the profiles in the region to the east of Greenland and over western Europe. The low-level PV anomalies are of similar amplitude in both regions although we can see some structural differences for the weaker cyclones. $\Delta\mathrm{PV}$ at the upper-levels varies strongly between cyclones from different intensity classes in the Greenland region. The amplitudes of the upper-level anomalies are also much lower than in the western Europe, where even weak cyclones still have high $\Delta\mathrm{PV}$ values above.

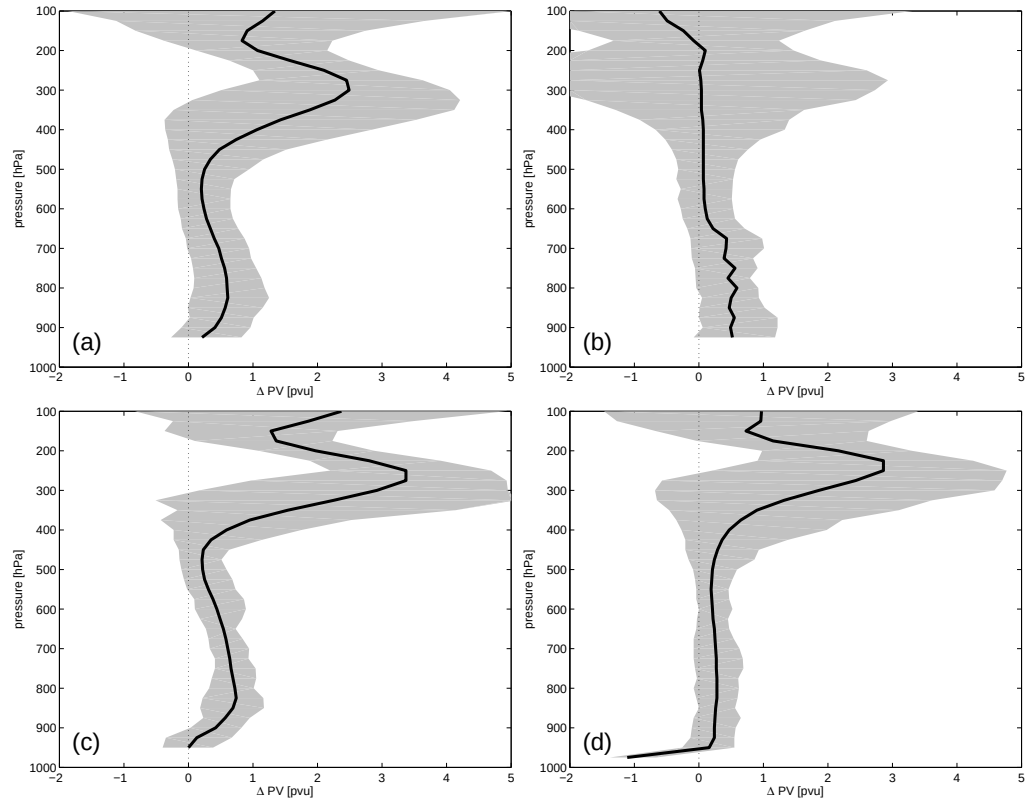

Figure 3.10: Average $\Delta\mathrm{PV}$ profiles for cyclones with a minimum central SLP in the range of (a,c) $930 - 970$ hPa and (b,d) $990 - 1010$ hPa for cyclones (a,b) east of Greenland and (c,d) in western Europe. Shaded area as in Fig. 3.6.

It is noteworthy that the formation of positive upper-level PV anomalies goes along with a lowering of the dynamical tropopause. Typically, more intense upper-level PV anomalies correspond to a higher tropopause pressure. For instance, the upper-level max-

imum of the 90th percentile is always lower than the 10th percentile in all mentioned regions. We will compare the height of the tropopause in different regions in Figs. 3.12 - 3.15.

3.3.4 Profile evolution

So far the investigation of the $\Delta\mathrm{PV}$ profiles and associated surface θ anomalies focused at the time when cyclones reached their maximum intensity. In this section some consideration is given to the temporal evolution of the cyclones' PV profiles during the 24 hours prior to the time of minimum central SLP.

Figure 3.11 presents the time evolution of the $\Delta\mathrm{PV}$ profiles, the surface $\Delta\theta$, and the central SLP for two selected intensity categories and regions. The selected cyclone categories are the very intense western North Pacific cyclones with minimum SLP between 930 and 970 hPa (Fig. 3.11a,c) and moderately intense cyclones with central pressure between 990 and 1010 hPa over western Europe (Fig. 3.11b,d). For the first category we can see large and rapid changes with time. $\Delta\mathrm{PV}$ in the lower troposphere increases on average by 0.7 PVU in 24 hours and the upper-level anomaly by 2.3 PVU. The low-level anomaly slightly rises and approaches the upper-level anomaly. The surface $\Delta\theta$ anomaly increases from 5.3 to 6.5 K (Fig. 3.11c) 12 hours prior to SLP minimum and then slightly decreases. This development is reflected in the evolution of SLP, which shows a rapid drop by more than 30 hPa in 24 hours. Some of the cyclones in this region can therefore be categorized as rapidly deepening cyclones or "bombs" (Sanders and Gyakum 1980). However, most of the cyclones do not undergo such a strong development, and the vertical PV structure of most of the weaker cyclones in all regions changes only slightly during the considered 1-day time period, as illustrated in Fig. 3.11b. The surface θ anomaly does, on average, increase only from about 0 to 1.5 K (Fig. 3.11d). Accordingly, the minimum SLP of these cyclones deepens only slightly during the same time period.

Fig. 3.11 presents only two very different developments. Also here, there is large variability between regions (also for cyclones of the same intensity). In certain regions one part of the profile develops much faster than the other and also $\Delta\theta$ can increase much more than in the selected regions.

The key characteristics of the $\Delta\mathrm{PV}$ profiles and surface θ anomalies of cyclones in different regions are summarized in Figs. 3.12 - 3.15. For various cyclone intensity categories the height of the tropopause (the 2 PVU line) is displayed along the vertical axis and vertically averaged low-level PV (averaged between 650 and 900 hPa) along the horizontal axis in the panels on the left. The middle panels display upper-level PV anomaly (averaged between 200 and 400 hPa) along the vertical axis and vertically averaged low-level PV anomaly (averaged between 650 and 900 hPa) along the horizontal axis. Surface $\Delta\theta$ is shown in the right panels. This representation allows us to easily compare the vertical PV structure of cyclones in different regions, different intensity classes and stages of cyclone development. The top panels in Fig. 3.12 present the characteristics of the PV profiles at the time of the maximum intensity t_0, the following rows include the results

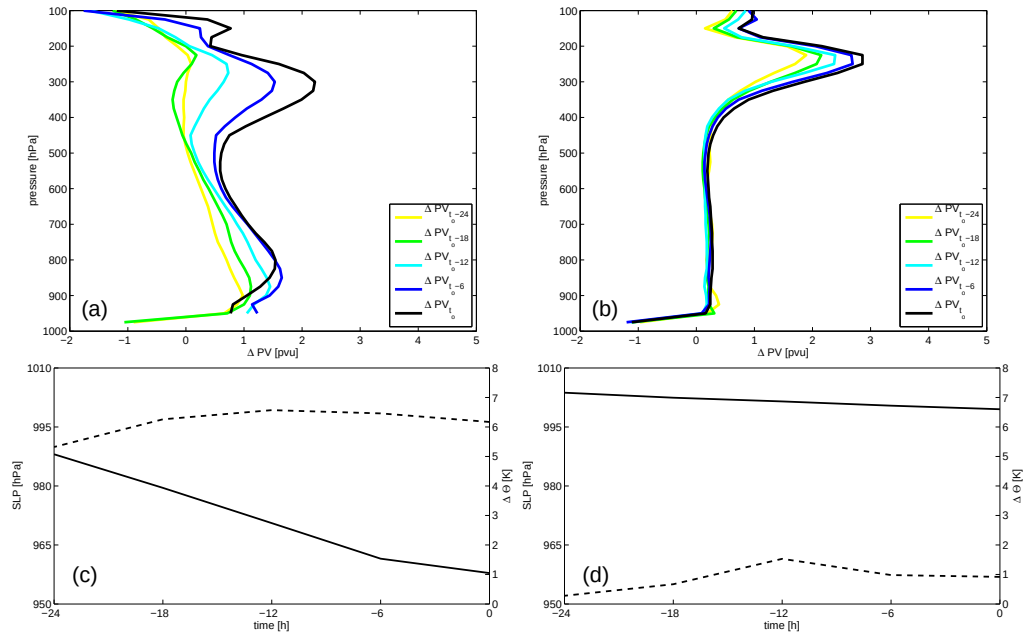

Figure 3.11: Composite time evolution of ΔPV profiles (a,b), surface θ anomalies (dashed line) and central SLP (solid line) (c,d) for: (a,c) cyclones in the western North Pacific with minimum SLP between 930 and 970 hPa, and (b,d) cyclones over western Europe with minimum SLP between 990 and 1010 hPa. Colors indicate different times of the cyclone evolution: time of minimum SLP t_0 (black), t_0-6 h (blue), t_0-12 h (cyan), t_0-18 h (green) and t_0-24 h (yellow).

for $t_0 - 6\text{h}$, $t_0 - 12\text{h}$, $t_0 - 18\text{h}$ and $t_0 - 24\text{h}$. The panels for the t_0, which will be most thoroughly discussed here, are framed.

The results for the winter cyclones show that at the time of maximum intensity (framed panels in Fig. 3.12) both the positive PV anomaly at upper levels and the diabatically produced PV at lower levels are important for determining cyclone intensity. The most intense cyclones (blue symbol) have clearly higher values of all three variables than the weak ones (orange symbol). The averaged low-level ΔPV (middle panel) in weak cyclones in the whole Northern Hemisphere (symbols with a black edge) amounts to 0.2 PVU on average, while strong cyclones exhibit mean values of about 0.6 PVU. Surface θ anomaly ranges from 2.7 to 5.7 K (right panel). The tropopause reaches down to more than 400 hPa in some regions (left panel). Note that these values are lower than the values mentioned in the comparison of the PV profiles, because here we are interested in the vertically averaged values and do not refer to the maxima. In this way it is easier to compare the different cyclones because the maxima are not always at the same height. It is also important to note that for the amplitude of the induced cyclonic circulation not only the maximum PV value in the vertical profile is relevant but also the contributions from several levels.

Again a look at characteristic values in different regions confirms the large regional

variability. The symbols in Fig. 3.12 correspond to those used in Fig. 3.8. Comparing again four intensity categories, the western North Pacific cyclones (circles) have the largest variation in terms of low-level $\Delta\mathrm{PV}$ (from 0.2 to 1.25 PVU) pointing to the crucial importance of this parameter for cyclone intensity in this region. Also cyclones in the eastern North Pacific and western North Atlantic exhibit large variability in this parameter. Differences in the upper-level $\Delta\mathrm{PV}$ values are largest in the western North Pacific, eastern North Atlantic and Greenland. This anomaly is the largest in the eastern North Pacific for all intensity classes (all values above 2 PVU). The upper-level $\Delta\mathrm{PV}$ values in the western North Pacific are not very high (1.6 PVU), but the anomalies reach the furthest into the troposphere (440 hPa). Surprisingly, the tropopause is not the lowest in Greenland and Alaskan cyclones, as we would expect because of their location to the north where climatological dynamical tropopause is much lower than in the south. The tropopause height for most intense cyclones in the eastern North Pacific is approximately 20 hPa smaller than for Alaskan cyclones even though they lie directly to the south-east of the Alaskan region. The situation is similar for intense Greenland and eastern North Atlantic cyclones. However, in the three weaker intensity classes, the tropopause is lower in the region further north. Western European, Mediterranean and Alaskan (except the weakest) cyclones of different intensity categories exhibit less variability in both directions.

The weakest cyclones near Greenland have rather high low-level PV values. These are stationary features above Greenland. Their low-level PV values peak between 700 and 800 hPa (average values up to 4 PVU). Greenland is approximately 3000 m high and PV values on its surface can reach extreme values, probably because of increased stratification due to diabatic cooling at the surface.

Figure 3.12 shows on the right the corresponding surface anomalies of potential temperature. As expected, the strongest cyclones have the highest positive potential temperature anomaly. The values are between 4 K in western Europe and 7 K in the western North Atlantic. $\Delta\theta$ for the weakest cyclones is close to 0 K in most regions, except in the western North Pacific, where it is higher than 3 K. The variability between the cyclones of different intensity is the largest for cyclones near Greenland and the smallest for cyclones in both Pacific regions. The weakest Greenland cyclones even have a negative anomaly in the centre, but since these are stationary cyclones above Greenland, this result might not be very representative of oceanic cyclones. We find the largest positive anomalies in the western parts of both oceans.

In the panels below the top row in Fig. 3.12 we can follow the development of these features in the last 24 hours of the cyclone development (before it reaches the maximum intensity). 24 hours earlier cylones are more similar to each other, the PV anomalies are smaller and the tropopause is higher. In the next hours the point cloud grows toward the upper right corner in the middle panels, but its base remains at approximately the same position. The anomalies in the stronger cyclones grow much faster than in the weaker cyclones and the spread gets larger. The symbols of the weaker cyclones do not move much with time, those cyclones therefore do not undergo any strong development. In the development of the weaker cyclones it is more the upper level PV anomaly that grows

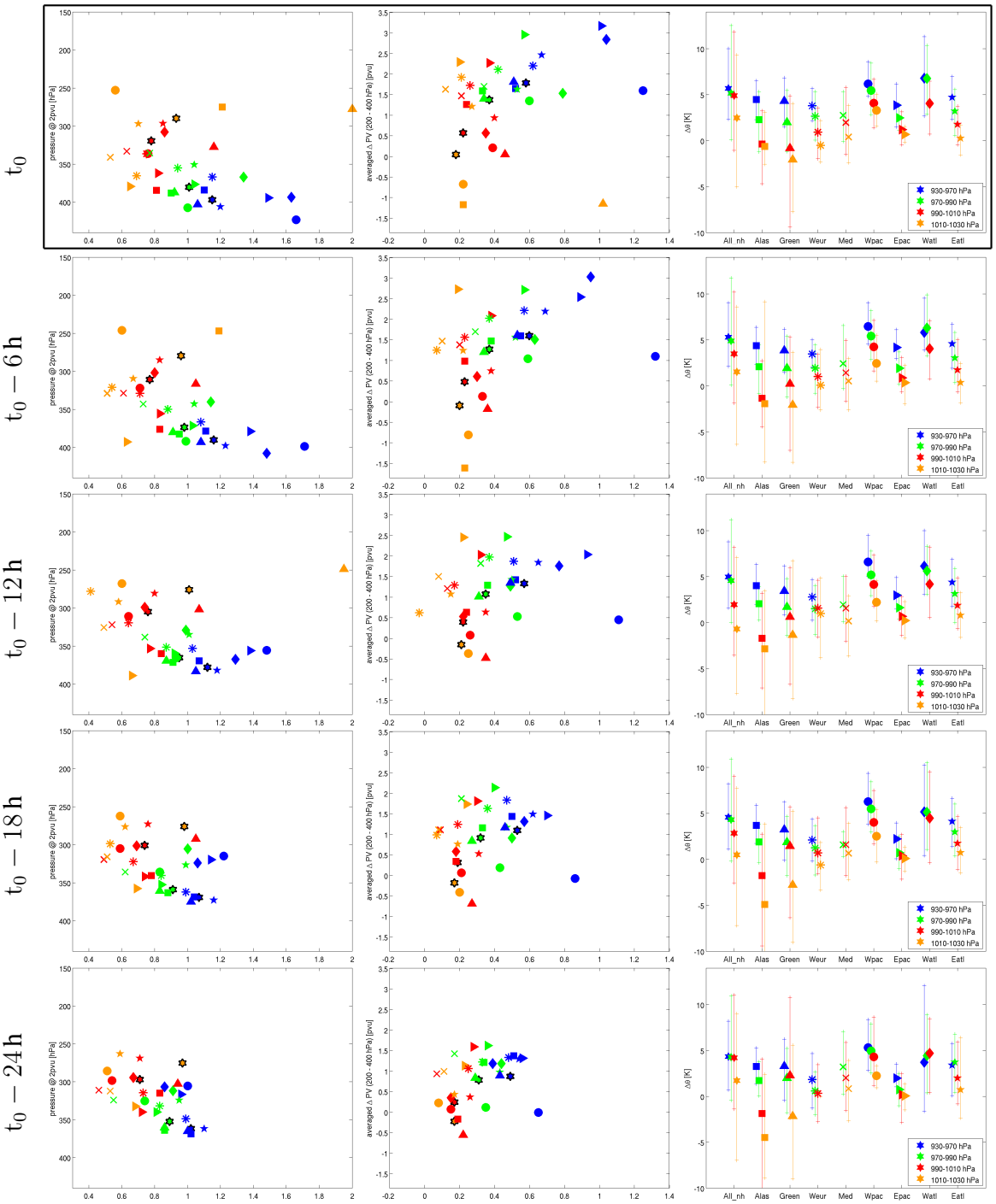

Figure 3.12: Time evolution of profile characteristics for DJF cyclones for 24 hours before the maximum intensity. Left: Average absolute PV at low-levels and the tropopause height. Middle: upper- and low-level PV anomaly. Right: Anomaly of surface potential temperature. Time runs from bottom to upper panel (every 6 hours).

and less the low-level PV anomaly. In the eastern North Pacific, for instance, it grows from 1.1 PVU to 2.3 PVU in 24 hours. In the Mediterranean, it reaches 1.6 PVU after growing for 0.7 PVU in 24 hours. However, it is negative all the time for the weakest cyclones in the western North Pacific and over Alaska. The most of the weakest Alaskan and Greenland cyclones appear or move over mountainous regions. There, climatological PV values are not defined at the lower pressure levels (up to 750 hPa in Alaska and even higher over Greenland) and consequently also the lowest part of $\Delta\mathrm{PV}$ profile in cyclones' centres could not be calculated. Data were missing in the interval where low-level $\Delta\mathrm{PV}$ was vertically averaged. These anomalies are therefore missing in the middle panels of Fig. 3.12 for the first 12 hours of the intensification phase although absolute low-level PV values are shown in the right panels. Potential temperature anomaly does not grow strongly in most regions, except for the weak cyclones around Alaska and the intense western North Atlantic cyclones where it grows for about 3 K in 24 hours.

Several case studies have shown that very intense cyclones require diabatically produced low-level PV for their extreme deepening. This seems to be confirmed on a climatological basis by the results in Fig. 3.12. In the same area, more intense cyclones are on average associated with higher values of low-tropospheric PV (weak cyclones near Greenland being an exception). Interestingly, in particular the framed middle panel indicates sort of a kink in the relationship between the amplitudes of upper- and low-level PV anomalies, we cannot fit a straight line to the points in the plot. Obviously, the strongest cyclones (blue) differ from moderately strong cyclones (green) mainly in terms of the amplitude of low-level PV (and less so in terms of upper-level PV). This highlights the particular relevance of diabatic PV production for very intense cyclones. (Note that most case studies in the literature on the role of diabatically produced PV have been made for very strongly intensifying systems.) This behavior also confirms the nonlinearity of the processes that determine cyclone intensity. Clearly, cyclones with strong anomalies on one level have the potential to strongly influence the flow on the other level, leading to strong nonlinear feedbacks. It is also noted that cyclones that have a potential to become very strong often possess a significant low-level PV anomaly already at the beginning of the deepening phase (e.g., Gyakum et al. 1992). It can be seen here in the development of low-level PV anomaly for western and eastern North Pacific cyclones, which is very pronounced already 24 hours before t_0 (middle panels in in Fig. 3.12).

Climatological studies (e.g., Wernli and Schwierz 2006) show that the cyclone frequency distribution changes with seasons. This is what we notice in this study, too. The numbers of cyclones in different seasons were displayed in Table 3.2. In Figs. 3.13 - 3.15 the same scatter plots as in Fig. 3.12 are presented for the spring (MAM), summer (JJA) and autumn (SON) season, respectively. The numbers of cyclones in several selected regions are lower than in the winter, in particular the number of strong cyclones. Compared to the winter plot, some marks are missing in the other plots because there were no (or too few) cyclones with a certain intensity detected.

The patterns are similar as in winter, but we can notice some variations. In MAM (Fig. 3.13), the upper-level PV anomaly tends to be stronger than in winter and also the

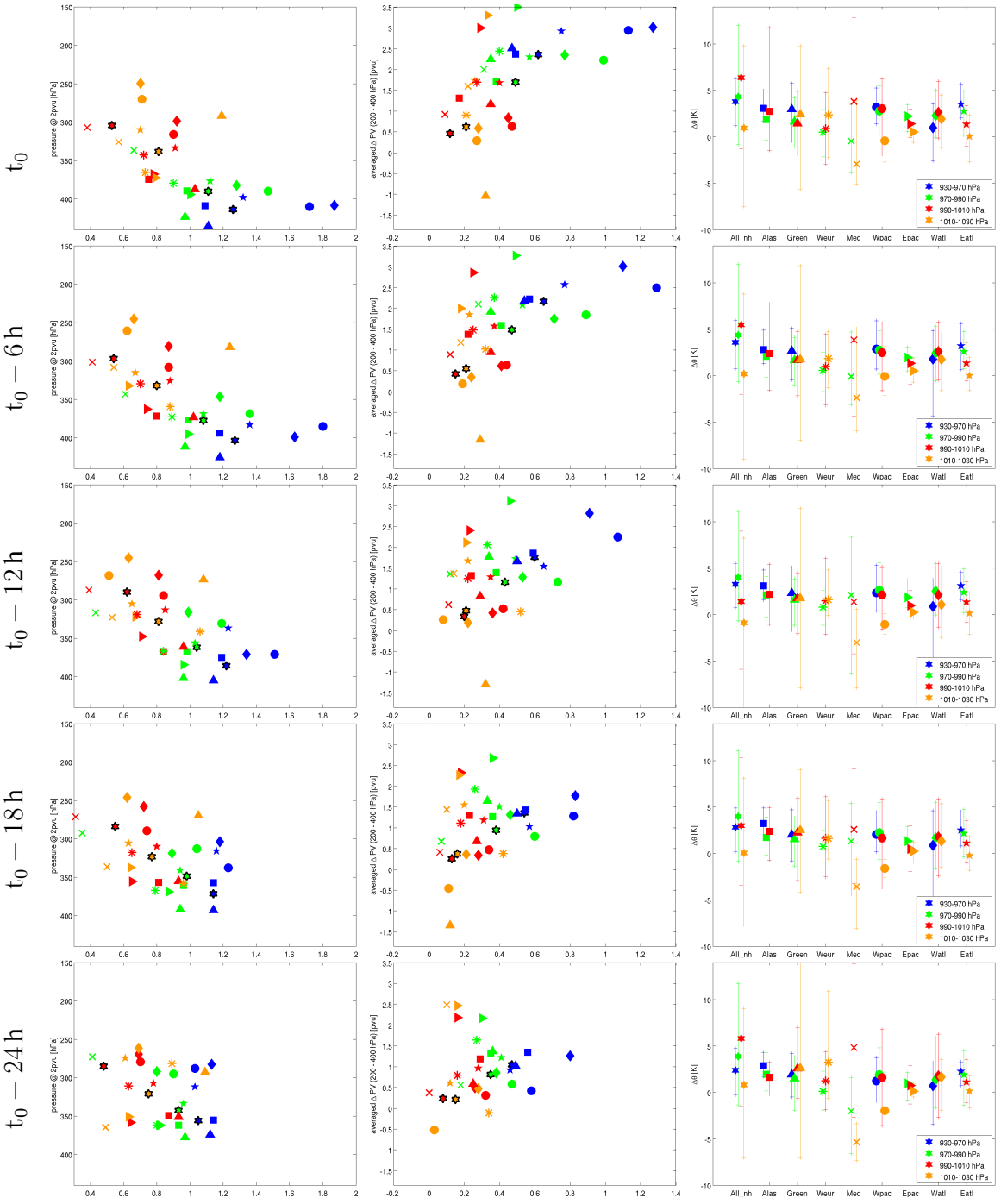

Figure 3.13: As Fig. 3.12, but for the spring season (MAM).

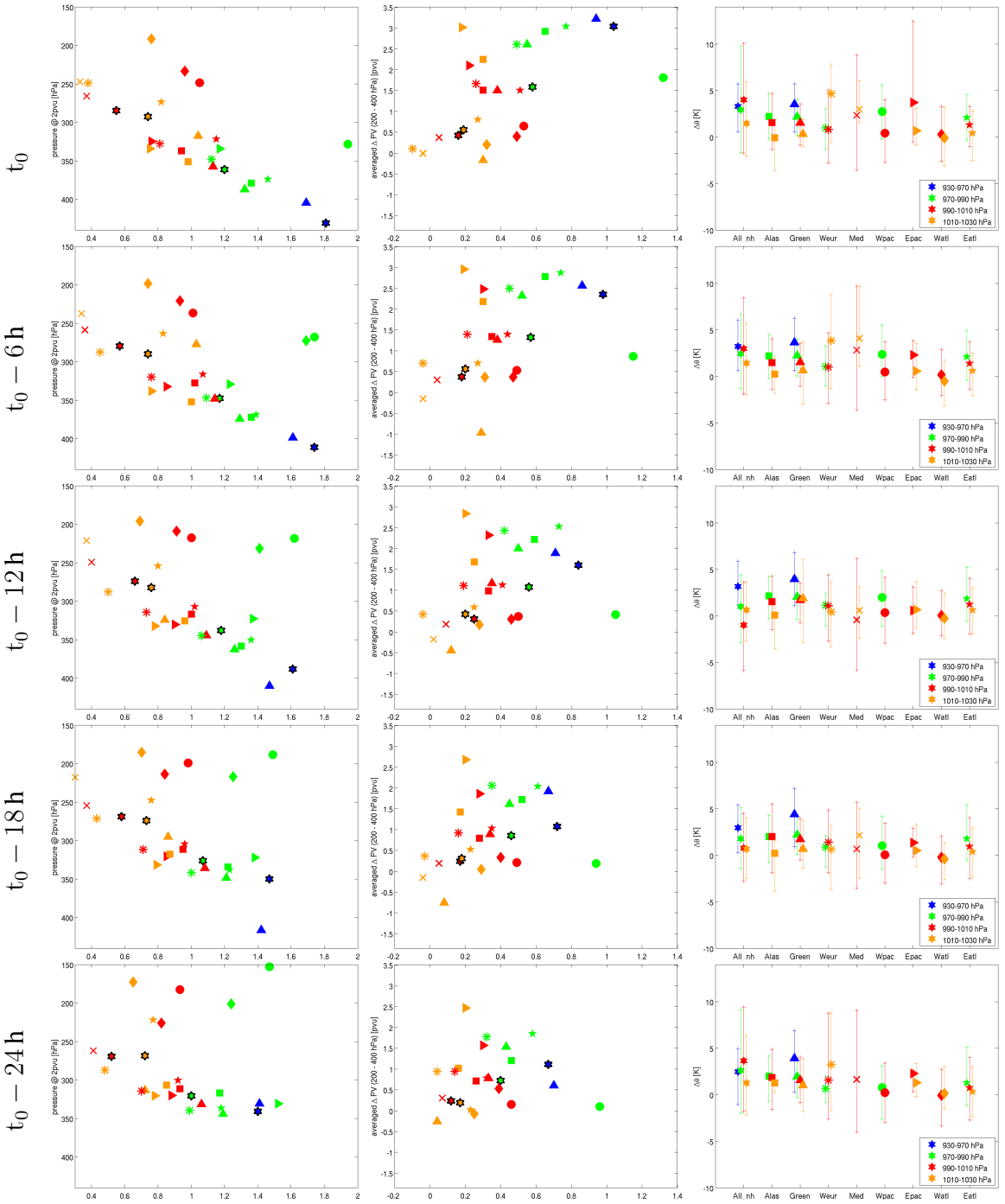

Figure 3.14: As Fig. 3.12, but for the summer season (JJA).

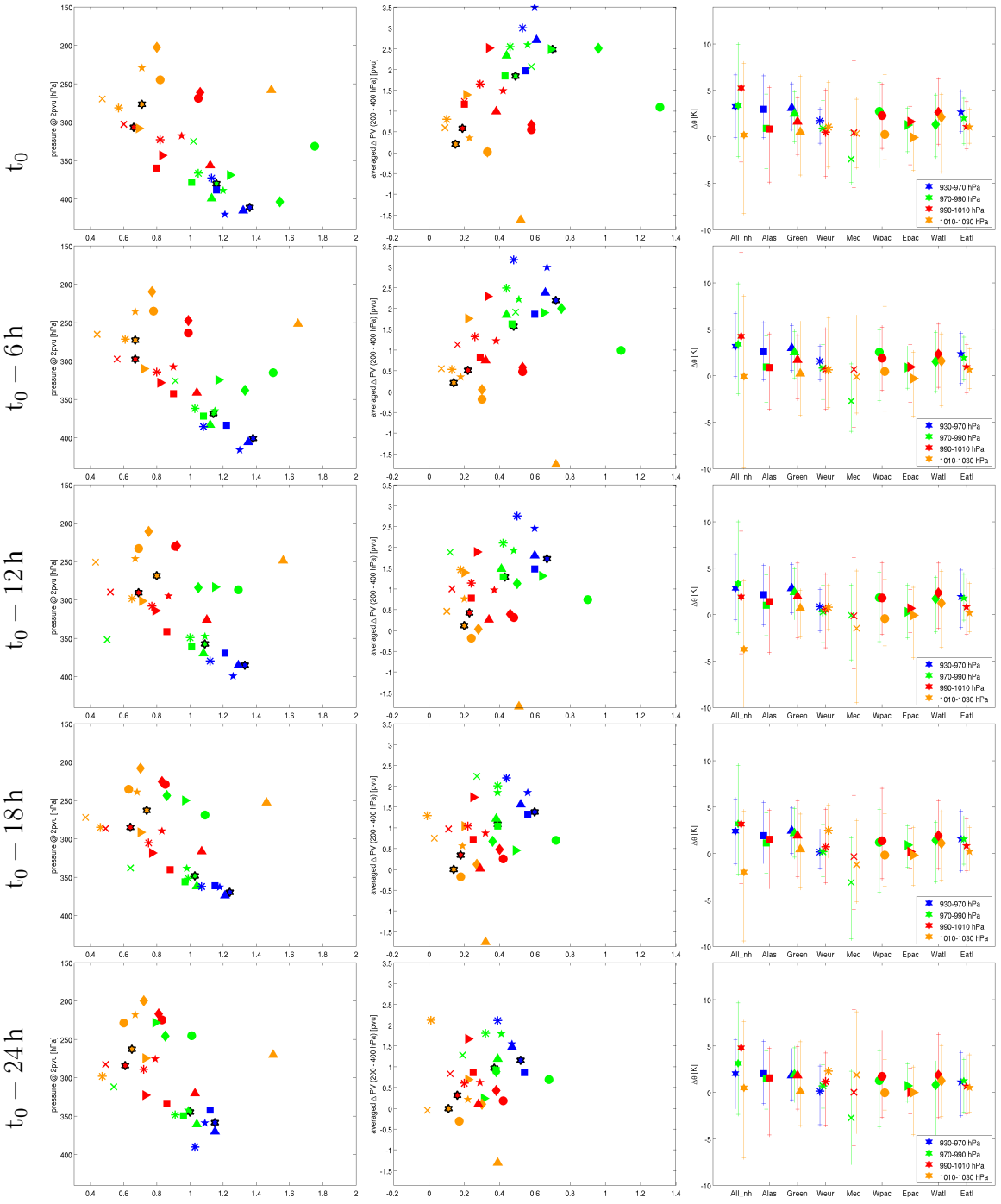

Figure 3.15: As Fig. 3.12, but for the autumn season (SON).

tropopause is slightly lower on average. Surface potential temperature is not as variable as in winter but the weaker cyclones are warmer. In JJA (Fig. 3.14), cyclones of one intensity class tend to have higher $\Delta\mathrm{PV}$ values at both levels compared to winter cyclones. The low-level PV values of the cyclones with the central SLP in the range of $970 - 990$ hPa are $0.1 - 0.7$ PVU higher than in winter. This tendency towards more pronounced values of diabatically produced PV might be explained by a larger supply of moisture evaporating from the warmer ocean surface (compared to winter). Cyclones of this intensity class (green symbols) in the eastern North Atlantic and western North Pacific show the largest increase in low-level PV anomaly compared to winter, while the differences are not so obvious for cyclones in western Europe and around Greenland. On the contrary, the cyclones in western Europe show much more variability in terms of upper-level PV anomaly compared to winter (the difference between the green and the orange symbol is 2.5 PVU in summer compared to 0.2 PVU in winter). Overall, the variability of both PV anomalies as well as tropopause height is the largest for all Northern Hemisphere cyclones (symbols with a black edge) compared to other seasons. In summer all weakest identified Mediterranean cyclones reach their maximum intensity earlier than in 24 hours, therefore this simbol is missing in the bottom panels of Fig. 3.14. The surface potential temperature anomalies are much smaller than in winter, with values between 0 and 4 K (see right panels in Fig. 3.14). They are especially low in the western North Pacific, both North Atlantic regions and around Alaska. They do not always increase monotonically with the cyclone intensity implying that the intensity depends less on the amplitude of the surface θ anomalies for some regions in summer. SON cyclones have less absolute low-level PV compared to other seasons but the variability in tropopause height is very pronounced (left panels in Fig. 3.15). The tropopause is very high especially for weaker cyclones. The differences in $\Delta\mathrm{PV}$ at upper and lower levels between the cyclones in different intensity classes for the selected regions is the smallest in this season (middle panels). Besides western European also the Mediterranean cyclones exhibit large variability in terms of upper-level $\Delta\mathrm{PV}$ (the same also for MAM). $\Delta\theta$ values are similar to those in JJA, but they are much more in agreement with cyclone intensity than in JJA.

3.3.5 Statistical significance

In order to see whether the differences in PV structures between cyclone categories are statistically significant, we performed a T test analysis. We compared profiles of cyclones with different intensities in each region, upper (between 200 and 400 hPa) and lower ($650 - 900$ hPa) part of $\Delta\mathrm{PV}$ and surface $\Delta\theta$ separately. Table 3.3 shows the test results for the DJF cyclones at the time of SLP minimum. A value of 1 means that we can reject the null hypothesis that the two compared profiles are identical at the 5% significance level and 0 that we cannot. For instance, for western North Pacific, comparing cyclones with SLP of $930 - 970$ hPa to those with SLP of $990 - 1010$ hPa (the profiles shown in Figs. 3.9a,b) and $1010 - 1030$ hPa, we can reject the null hypothesis for all parts of the profile (cf. third and fourth column in Table 3.3 for Wpac). Comparing the strongest cyclones

Table 3.3: Significance tables for all regions for DJF for upper-level ΔPV/ low-level ΔPV/surf. $\Delta\theta$. Each triplet of numbers is for a combination of profiles from two categories indicated on the top and on the left side of the Table. Value of 1:the two compared anomalies are significantly different; 0: the null hypothesis - that the profiles are identical - cannot be rejected.

Alas	$970-990$ hPa	$990-1010$ hPa	$1010-1030$ hPa
$930-970$ hPa	0/1/1	0/0/1	1/0/1
$970-990$ hPa		0/0/1	1/0/1
$990-1010$ hPa			1/0/0
Green	$970-990$ hPa	$990-1010$ hPa	$1010-1030$ hPa
$930-970$ hPa	1/0/1	1/0/1	1/1/1
$970-990$ hPa		1/1/1	1/1/1
$990-1010$ hPa			1/0/0
Weur	$970-990$ hPa	$990-1010$ hPa	$1010-1030$ hPa
$930-970$ hPa	0/0/1	1/1/1	0/0/1
$970-990$ hPa		1/0/1	0/0/1
$990-1010$ hPa			0/0/0
Med	$970-990$ hPa	$990-1010$ hPa	$1010-1030$ hPa
$930-970$ hPa	0/0/0	0/1/1	0/1/1
$970-990$ hPa		0/1/1	0/1/1
$990-1010$ hPa			0/1/1
Wpac	$970-990$ hPa	$990-1010$ hPa	$1010-1030$ hPa
$930-970$ hPa	0/1/0	1/1/1	1/1/1
$970-990$ hPa		1/0/1	1/0/1
$990-1010$ hPa			1/0/0
Epac	$970-990$ hPa	$990-1010$ hPa	$1010-1030$ hPa
$930-970$ hPa	0/1/0	1/1/1	0/1/1
$970-990$ hPa		1/1/1	0/0/1
$990-1010$ hPa			0/0/0
Watl	$970-990$ hPa	$990-1010$ hPa	$1010-1030$ hPa
$930-970$ hPa	1/0/0	1/0/1	1/0/0
$970-990$ hPa		0/1/1	0/0/0
$990-1010$ hPa			0/0/0
Eatl	$970-990$ hPa	$990-1010$ hPa	$1010-1030$ hPa
$930-970$ hPa	1/0/1	1/1/1	1/0/1
$970-990$ hPa		1/0/1	0/0/1
$990-1010$ hPa			0/0/1

tho those with SLP of $970 - 990$ hPa, we can reject it only for the low-level PV anomaly (second column in Table 3.3). In eastern North Atlantic, for the profiles of the highest two intensities, we can reject it for the upper-level and surface anomaly. For the second combination of profiles in Fig. 3.9, the most intense eastern North Atlantic cyclones and those with minimum SLP between $990 - 1010$ hPa, we can reject the null hypothesis for all three parts of the profiles (third column in Table 3.3 for Eatl). The test shows that both parts of the two profile combinations in Fig. 3.9 are significantly different. In several other profile combinations we can reject the null hypothesis only either for the lower part or for the upper part of the profiles. For weaker cyclones and for regions with very few cyclones the differences are not statistically significant at the 5% level both at upper and lower levels. Nevertheless, statistical significance itself does not necessarily also imply a physical relationship and vice versa. Therefore, we believe that we can obtain important information also from the parts that are not significantly different.

3.4 Summary and discussion

The vertical structure of extratropical cyclones has been analyzed using composite PV and $\Delta\mathrm{PV}$ profiles and $\Delta\theta$ at the surface in the surface cyclones' centre. Until now, this aspect of the vertical structure of cyclones has been investigated mainly in case studies. The statistical analysis performed in this study, based upon the climatology of cyclone tracks in the ERA-Interim dataset, provides new insight into the structure of extratropical cyclones in different geographical regions and for different intensity categories. Recalling the questions posed in the introduction, we have found out:

1. On average, more intense cyclones (in terms of central SLP) are associated with higher low-tropospheric $\Delta\mathrm{PV}$ values in their centre and a more prominent upper-level positive PV anomaly, which mostly goes along with an increased pressure at the dynamical tropopause. The stronger cyclones also have a more intense positive surface potential temperature anomaly in the centre. In winter, the averaged low-level $\Delta\mathrm{PV}$ values in the most intense cyclones (with central SLP between 930 and 970 hPa) in all regions are higer than 0.5 PVU, with the highest values of more than 1 PVU in the western and eastern North Pacific and western North Atlantic. In contrast, the low-level PV values in weaker cyclones (where central SLP ranges between 990 and 1010 hPa) reach up to only about 0.4 PVU. The surface θ anomaly of the intense cyclones is above 4 K in all regions, while for the weaker cyclones it ranges from 0 K around Greenland to 4 K in the western parts of the oceans. $\Delta\mathrm{PV}$ at upper levels is higher than 0.5 PVU for all most intense cyclones with the highest value of around 3 PVU in the western North Atlantic and eastern North Pacific. The upper-level $\Delta\mathrm{PV}$ in the weaker cyclones with central SLP between 990 and 1010 hPa varies between 0 and 2.5 PVU.

2. We have found large variability between the cyclones in different regions. West-

ern North Pacific and western North Atlantic cyclones exhibit large differences in low-level PV anomalies between strong and weak cyclones. This is an indication that condensational processes that produce the low-level PV may be especially important for their intensification. Cyclones from eastern North Atlantic, region east of Greenland and also western North Pacific are very variable in terms of upper-level $\Delta\mathrm{PV}$. This anomaly is the largest in eastern North Pacific cyclones. Low-level $\Delta\mathrm{PV}$ values are generally higher over the oceans. Also surface θ anomalies are the highest in the western parts of oceans.

3. The time evolution of PV profiles showed that the strongest ocean cyclones experience a marked intensification in terms of upper-level and diabatically produced low-level PV anomaly during the 24 hours prior to minimum SLP. Their surface θ anomalies are relatively high. The concomitant growth of the PV anomalies points to the positive mutual interaction of the anomalies for explosively intensifying cyclones. For weaker cyclones, the upper level anomaly develops while the low-level anomaly remains very weak in these 24 hours. The behaviour of the profiles and surface anomalies differs strongly between the regions.

4. We also found a significant seasonal dependency. Although summer cyclones are typically weaker than winter cyclones, both PV anomalies have larger amplitudes on average. The variability between cyclones of different intensities in the whole Northern Hemisphere is much larger in summer than in other seasons. However, surface $\Delta\theta$ values are lower, which might be related to smaller differences between temperatures of water and air. The spring cyclones have larger upper-level PV anomalies. The SON cyclones have less absolute low-level PV and a very pronounced variability in tropopause height.

Our method also has some caveats that we would shortly like to comment on. The method is slightly sensitive to the choice of the radius within which we calculate the horizontally averaged values. If the radius is too small, it can happen that we do not consider all the important parts of the PV structure. But if the radius is too large, the differences between the cyclones become very weak because of averaging over a (too) large area. The choice of a radius of 200 km appeared as a reasonable compromise between the two options. Another issue is related to the vertical tilt of most cyclones. Cyclones are never completely vertical, especially not during their intensification phase. We have tried to account for the cyclones' tilt by calculating tilted profiles using the method by Deveson et al. (2002). The drawback of this approach was that we lost a large amount of information from the PV in the lower troposphere, because the low-level PV anomaly (up to about 600 hPa) is often quasi-vertical. Also due to the fact that mature cyclones become more and more vertical when the upper-level anomaly approaches the position of the cyclone centre, we then decided to calculate only vertical profiles. The use of central SLP as an intensity measure can also be slightly problematic. We have chosen minimum SLP as a simple and widely used metric for cyclone intensity, but we recognize that it is not

an optimal choice when comparing cyclones in different regions of the world. Therefore we grouped cyclones in different regions and focus mainly on intensity differences for cyclones in the same region.

All in all, our investigation points to the importance of all three tropospheric PV anomalies (including warm air at the surface) for the development of extratropical cyclones. We have shown that on a climatological basis, in addition to a pronounced upper-level positive PV anomaly, the diabatically produced low-tropospheric PV anomaly, and a high surface θ anomaly are essential for the development of intense cyclones. This confirms results from earlier modelling studies (e.g., Uccellini et al. 1987; Kuo et al. 1991, 1995; Wernli et al. 2002) and studies that used piecewise PV inversion (Davis 1992; Huo et al. 1999).

A rather new finding from this study is the large regional variability of the vertical structure of extratropical cyclones. This topic was addressed previously by Wang and Rogers (2001) and Dacre and Gray (2009), but only for cyclones in the North Atlantic. Wang and Rogers (2001) found a lower tropopause and higher (absolute) PV values in explosive eastern Atlantic cyclones compared to those in the western North Atlantic, which is only partially in agreement with our results. For our most intense cyclones the tropopause was indeed slightly lower in the eastern North Atlantic but $\Delta\mathrm{PV}$ is not larger than in the west. For moderately intense cyclones the upper-level PV anomaly in the east ist stronger but it lies higher than the anomaly for the western North Atlantic cyclones. But Wang and Rogers (2001) use somewhat different regions, seasons and analysis method and it can influence our comparison. They further found that the low-level PV is stronger in the cyclones in the eastern part of the ocean at the beginning of the development, which then weakens rapidly. In their study the low-level PV anomaly in western North Atlantic cyclones develops more slowly but reaches a higher value and remains present for a longer time period. Our study also identified cyclones with higher low-level PV values 24 hours before t_0 in the eastern part of North Atlantic which only slightly increase in the next hours. On the contrary, the low-level PV values in the intense western North Atlantic cyclones increase strongly in this period and are much stronger at t_0.

Our study included several other regions in the Northern Hemisphere and extended previous results to identify more important characteristics of cyclone variability between different regions.

Chapter 4

Evaporative moisture sources of the diabatically produced parts of cyclones' PV towers

4.1 Introduction

In extratropical cyclones, PV at low levels is produced diabatically during condensation processes below the maximum of latent heat release (e.g., Wernli and Davies 1997). Therefore moisture is needed for its production. However, sources of moisture involved in the PV production close to the center of extratropical cyclones have not been identified yet. In this study, we are interested in the source of PV that can be found in the cyclone centre at the time of its maximum intensity and the moisture involved in its production. A Lagrangian analysis will allow us to consider material changes of air parcels' PV and humidity along their pathway and to identify the evaporative moisture sources of the water vapor that later contributed to the formation of the bottom part of the mature extratropical cyclone's PV tower. Such an investigation is possible with a recently developed Lagrangian moisture source diagnostic (Sodemann et al. 2008; see below) and it is motivated by the following questions:

- Where are the evaporative moisture sources of extratropical cyclones relative to their track? For instance, do cyclones tap into a "moisture reservoir" on the warm side of their track, or is the cyclone-induced evaporation in the close vicinity of the track an important moisture contribution?

- What is the typical timescale between evaporation and condensation (i.e., PV production) in the cyclone?

- Do evaporative moisture sources differ for weak and intense cyclones developing in the same region?

- Do the answers to the first two questions differ for cyclones in different geographical areas (e.g., at the beginning and end of a storm-track)?

A particular setup of trajectory calculations will be used to address these questions, as explained in detail in the next subsection. In the next paragraphs, the history of Lagrangian studies of extratropical cyclones will be briefly summarized, including an overview on methods developed to identify evaporative moisture sources.

The Lagrangian view of synoptic systems goes back more than 100 years. Very early studies using a Lagrangian approach include Shaw (1903) who computed surface air trajectories for the first time and Bjerknes (1910) who stressed the importance of a continuous representation of the air motion.

The idea of the Lagrangian view of weather systems enabled the identification of distinct coherent features of the flow related to extratropical cyclones, such as warm and cold conveyor belts and the dry intrusion (Harrold 1973, Carlson 1980, Browning 1986). Later Wernli and Davies (1997) and Wernli (1997) introduced objective criteria to define these airstreams. Airstreams that experience strong latent heat release (e.g., warm conveyor belt) are characterized by a maximum decrease of specific humidity of at least 12 g/kg or maximum ascent of at least 620 hPa (now usually 600 hPa is used). The trajectories forming a dry intrusion are supposed to descend at least 350 hPa. To distinguish between stratospheric and tropospheric air (and transport across the tropopause), an additional criterion of PV values along trajectories is implemented (PV value larger than 2 PVU in the stratosphere and smaller than 2 PVU in the troposphere). Use of trajectories offers a complementary insight into the development of synoptic systems. Whitaker et al. (1988) investigated the Presidents' Day cyclone. They calculated backward trajectories to identify the regions where the air constituting the centre of the cyclone originated from. With forward trajectories they also identified the air streams around the cylone. With a combination of trajectories and charts of relative humidity, Reed et al. (1992) distinguished between diabatically produced PV in the cyclone centre and PV advected adiabatically from the upper troposphere. Both these studies used model data. The advent of global analysis and reanalysis datasets enabled extensive use of trajectory calculations. Also Rossa et al. (2000) and Wernli et al. (2002) used backward trajectories to identify the origin of high PV air in the centre of the investigated cyclone.

These Lagrangian studies indicated the importance of cloud diabatic processes and therefore also the relationship between ocean (and land) evaporation, atmospheric moisture transport and cloud formation. Specific techniques have been developed to objectively identify evaporative moisture uptakes along trajectories and within Eulerian weather prediction and climate models.

The first comprehensive Lagrangian moisture source analysis method was introduced by Dirmeyer and Brubaker (1999). It uses quasi-isentropic backward trajectories combined with model surface fluxes (evapotranspiration) to identify source regions. Their approach has advantages compared to the Eulerian methods, because this way it is possible to follow a parcel from the evapotranspiration area to the precipitation region. However, the method is only able to find the nearest source region and cannot distinguish between

the parcels in the vertical column of air that actually contribute to the precipitation. Stohl and James (2004) presented a completely Lagrangian approach. They calculate backward trajectories with an atmospheric dispersion model, interpolate specific humidity, q, to parcel positions and then diagnose material changes in q between two output times. The method is advantageous compared to the one by Dirmeyer and Brubaker (1999) in being able to locate q changes directly and also including all uptakes along the trajectory. However its drawback is that it does not account for the moisture lost by previous precipitation events along the trajectory, which leads to an overestimation of remote moisture uptakes. Also it does not distinguish between moisture changes in and above the boundary layer, respectively. The method by Sodemann et al. (2008) addresses these issues. It only accounts for moisture uptakes in the boundary layer and it allows for a quantitative demarcation of moisture sources by considering moisture loss along trajectories due to precipitation.

Several studies used one of these Lagrangian approaches (or simpler variants) to investigate evaporative moisture sources of precipitation in certain regions. Massacand et al. (1998) looked for sources of heavy precipitation on the Alpine south side by examining specific humidity along backward trajectories. Dirmeyer and Brubaker (1999) investigated sources of moisture during one drought and one flood year over the USA. They found that different sources contribute during drought and flood years. A large percent of moisture was found to be recycled during the drought season and there was a larger contribution from remote sources during the flood season. Reale et al. (2001) and Turato et al. (2004) applied the method introduced by Dirmeyer and Brubaker (1999) to several cases of severe floods in the Mediterranean region. Stohl and James (2004) and James et al. (2004) deployed their method to investigate moisture sources of the extreme rainfall in the first half of August 2002 leading to a severe Elbe flooding event. They found that most moisture originated in the western Mediterranean with additional sources over the Black Sea and eastern Europe.

Other studies considered longer periods and investigated climatological sources of moisture for different regions: Brubaker et al. (2001) focused on the Mississippi river basin, Stohl and James (2005) addressed transport between oceans and river catchments, Nieto et al. (2006, 2007) looked into moisture sources of precipitation in the Sahel and over Iceland, respectively, using the method by Stohl and James (2004). The same method was used, e.g., by Stohl et al. (2008) for the Norwegian west coast and Drummond et al. (2010) for northeastern Brazil. Sodemann et al. (2008) applied their method to Greenland precipitation, Sodemann and Stohl (2009) to precipitation above Antarctica, and Sodemann and Zubler (2010) to precipitation in Central Europe. Pfahl and Wernli (2008) used a similar method to identify sources of moisture at a measuring site of stable water isotopes in Israel and were able to quantitatively link isotopic values to the atmospheric conditions at the moisture uptake locations.

In parallel to Lagrangian methods novel Eulerian tracer methods have been developed for getting detailed insight into the atmospheric water cycle in general circulation models (Numaguti 1999, Bosilovich and Schubert 2002, Bosilovich et al. 2003) and numerical

weather prediction models (Sodemann et al. 2009, Winschall et al. 2011). These methods are applied to study moisture sources in predefined areas (e.g., Eurasia, North America, India, Central Europe).

Here the moisture source identification method by Sodemann et al. (2008) will be applied to learn more about the relationship between ocean evaporation and diabatic PV production in extratropical cyclones (see open research questions above). For this novel application (compared to the more standard application devoted to the origin of atmospheric moisture or precipitation), a slightly refined, three-step Lagrangian setup will be required (see next subsection).

4.2 Method

In order to identify evaporative moisture sources of air parcels that contribute to the diabatic formation of the low-tropospheric part of the PV tower associated with mature extratropical cyclones, the following three-step approach is applied:

1. Two-day backward trajectories are calculated from the low-level part of cyclones' PV towers (black trajectory in Fig. 4.1). Trajectory starting points are characterized by PV values larger than 1 PVU within a cylinder around the cyclone center. The dimensions of the cylinder are a radius of 200 km and a vertical extension from 900 to 600 hPa. Potential trajectory starting points are considered every 0.5° in the horizontal and every 50 hPa in the vertical. Along these trajectories the locations where diabatic PV production occurs are identified. A six-hourly trajectory segment is regarded as a PV production region if the six-hourly change of PV along the trajectory exceeds a certain threshold value: $\Delta PV = PV(t) - PV(t - 6\,\mathrm{h}) > 0.2\,\mathrm{PVU}$. The threshold was used to eliminate small and insignificant PV changes from the analysis. Additional criteria for PV production at time t are that (i) $PV(t) > 0.5\,\mathrm{PVU}$ and (ii) that no 6-hourly PV loss larger than 0.4 PVU occurs between time t and the start time of the trajectory. With the first criterion we focus on diabatic PV production that leads to PV values exceeding the climatological low-tropospheric PV value of about 0.5 PVU. With the second criterion we avoid considering PV production that is not relevant for the formation of the PV tower at the start time of the trajectories. Typically, for one starting point within the PV tower, several PV production regions are identified at different times.

2. The identified PV production locations are used to prepare the starting points for the second trajectory calculation. Since for diabatic PV modification the vertical gradient of the latent heating is important (see Section 1.4), we are interested in the moisture origin of both the air parcels just above and below of the PV production location. Therefore at each PV production location (lat, lon, p), seven starting points for a second set of backward trajectories are specified at (lat, lon, $p + n \cdot 50\,\mathrm{hPa}$), where $n = -2, -1, 0, 1, 2, 3, 4$. If at one of these points relative humidity is below

80% (i.e., the point is outside the cloud), then the point is excluded from the list of starting points.

3. A second set of trajectories is calculated from these new starting points, 10 days backward (blue trajectories in Fig. 4.1). The Lagrangian moisture source diagnostic by Sodemann et al. (2008) is then applied along these trajectories.

All trajectories are calculated with the Lagrangian analysis tool LAGRANTO introduced by Wernli and Davies (1997) and by using 6-hourly three-dimensional wind fields from the ERA-Interim reanalyses. Further variables calculated along the trajectories are specific and relative humidity, potential temperature and PV, and the height of the trajectory relative to the diagnosed ERA-Interim boundary layer height.

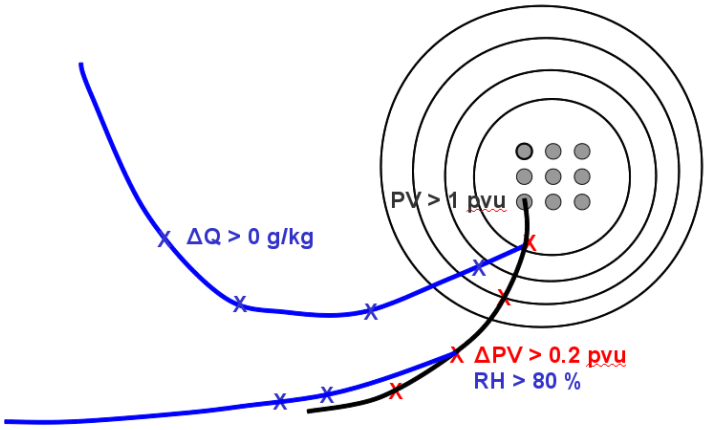

Figure 4.1: Schematic of the Lagrangian approach to identify moisture sources for the lower part of extratropical cyclones' PV towers. Black line: 48-h trajectory from the cyclone centre to identify PV production regions; blue lines: 10-day backward trajectories to identify evaporative moisture sources. Red crosses: PV production regions; blue crosses: moisture uptake regions.

The moisture source identification method (described in more detail in Chapter 2.2.3) is then applied to the second set of 10-day backward trajectories. It first identifies all locations with $\Delta q = q(t) - q(t-6h) > 0.2\,\mathrm{g\,kg^{-1}}$ in the boundary layer. As for the Lagrangian PV changes discussed above, the finite threshold helps focusing on the essential contributions. If precipitation occurs, it adjusts (reduces) each contribution for the proportional amount of precipitated moisture recursively. Finally, adjusted moisture uptake values (in $\mathrm{g\,kg^{-1}}$) are gridded onto a $1^\circ \times 1^\circ$ grid in order to obtain accumulated moisture uptakes (in $\mathrm{g\,kg^{-1}}$ per $10000\mathrm{km}^2$) for one particular PV tower. From these fields composite moisture uptake regions are calculated for all cyclones in a certain region.

Before presenting results of this procedure for two selected case studies, a few issues associated with this approach are highlighted: (i) The approach is more complicated compared to previous applications of the Sodemann et al. (2008) method, because here we are interested in the moisture origin of air parcels, which experience condensational latent heating, which in turn leads to PV production and advection into a cyclone center. Due to the potential time lag between PV production and maximum cyclone intensity (i.e., the time of the PV tower) two sets of trajectories are required. (ii) For every cyclone investigated, the approach provides a map of surface evaporation of water vapor, which is later involved in the diabatic PV production of the lower part of the cyclone's PV tower. Clearly, if this PV tower is of weak intensity (i.e., if only a few grid points within the cylinder around the cyclone center have $PV > 1$ PVU) then only few backward trajectories will be calculated in step (1), which also likely leads to reduced moisture uptake values. (iii) Intense cyclones are typically associated with pronounced diabatic PV production, often strongly exceeding the threshold of 0.2 PVU within 6 hours, which is used to start trajectories for the moisture uptake diagnostic (see above). This indicates that the moisture source diagnostic does not consider the magnitude of the diabatic PV production (as long as it exceeds the threshold) and therefore, very similar moisture source fields might result for a weaker cyclone (where PV increases are typically just slightly above 0.2 PVU in 6 hours) and intense cyclones (where rapid lifting of the similarly humid air parcels can lead to much more pronounced diabatic PV production). These characteristics of the approach must be kept in mind when now looking at results.

4.3 Case studies

In the following subsections two case studies are presented to illustrate the method. The two cases of a North Atlantic and a North Pacific cyclone, respectively, have been selected to demonstrate the variability of moisture uptakes associated with the diabatic PV production contributing to the lower part of the cyclones' PV tower.

4.3.1 North Atlantic cyclone

A cyclone developed on 8-9 February 2007 in the western North Atlantic. Figure 4.2 shows the development of the cyclone with charts of SLP, potential temperature on 850 hPa, and PV on the same level. The cyclone first appeared at 00 UTC 8 February 2007 at $57°$W and $39°$N in a very strong baroclinic zone (Fig. 4.2a). The central SLP is 996 hPa and only a weak low-level PV anomaly is present in the cyclone centre at this time. However, the air at that location is very moist and latent heat is already being released at the time of cyclone formation (not shown here). The cyclone moves in the north-eastward direction along the baroclinic zone. Twelve hours later we find the cyclone at $44°$W and $43°$N (Fig. 4.2b). A stronger PV anomaly has formed in its centre where the SLP has decreased to 974 hPa. Directly downstream of the cyclone, a ridge starts to form

at the tropopause, which is represented by a green line in Fig. 4.2b. In the next 18 hours the cyclone continues its rapid deepening. Figure 4.2c shows the cyclone located at 30°W and 50°N at the time of its maximum intensity (06 UTC 9 February). It has deepened 35 hPa in 30 hours.

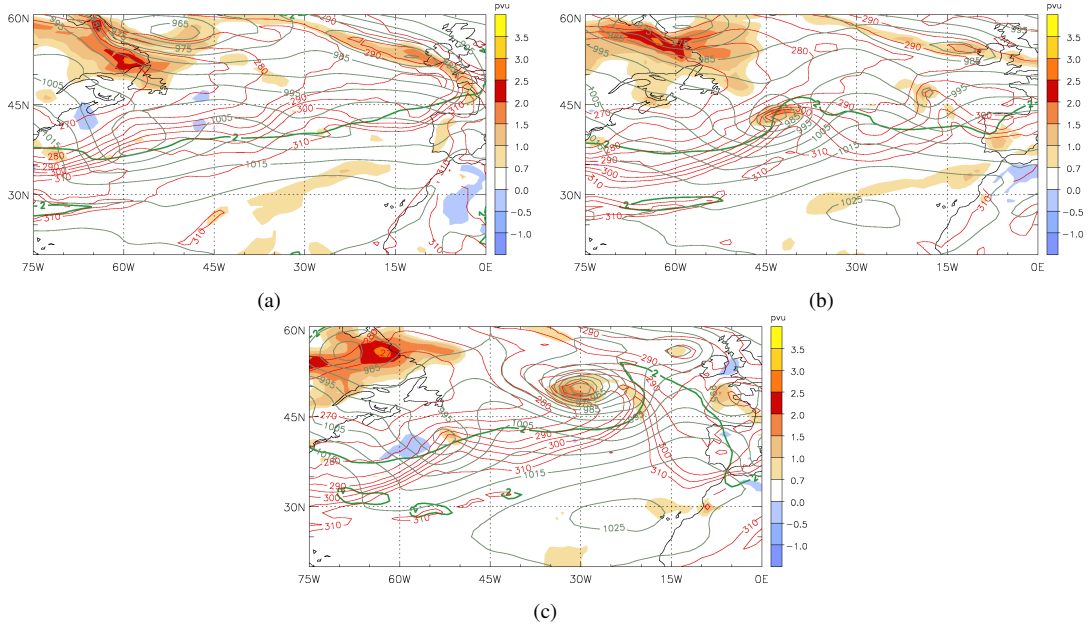

Figure 4.2: Development of the North Atlantic cyclone at (a) 00 UTC 8 February 2007, (b) 12 UTC 8 February 2007, and (c) 06 UTC 9 February 2007. Shown are PV at 850 hPa (colours, in PVU), SLP (grey lines, every 5 hPa), pot. temperature at 850 hPa (red lines, every 5 K), and the 2 PVU contour at 250 hPa (green bold line).

Our focus here is on the production of low-level PV, i.e., PV that can be found in the cyclone centre between 600 and 900 hPa. The evolution of the vertical PV profile during the last 24 hours of the intensification phase is presented in Fig. 4.3a (see chapter 3 for the explanation of the method) and the evolution of the SLP and the surface potential tempearture anomaly are shown in Fig. 4.3b. The time of maximum cyclone intensity, 06 UTC 9 February, is referred to as t_0. Already 24 hours before the cyclone was at its maximum intensity average low-level PV values were higher than 1 PVU, about 0.5 PVU higher than the climatological background. 6 hours before t_0, averaged PV at 800 hPa reached 1.9 PVU. In the last time step the low-level PV decreased although the cyclone slowly deepened further. However, upper-level PV anomaly and the anomaly of surface potential temperature are higher than one timestep earlier.

At 06 UTC 9 February we calculated 48 hour backward trajectories from the grid points in a column around the cyclone centre where PV values were larger than 1 PVU. We then identified points along these trajectories where diabatic PV production was above the threshold (see section above). From these points (and those above and below, see again the explanation in the previous section), we calculated 10-day backward trajectories and

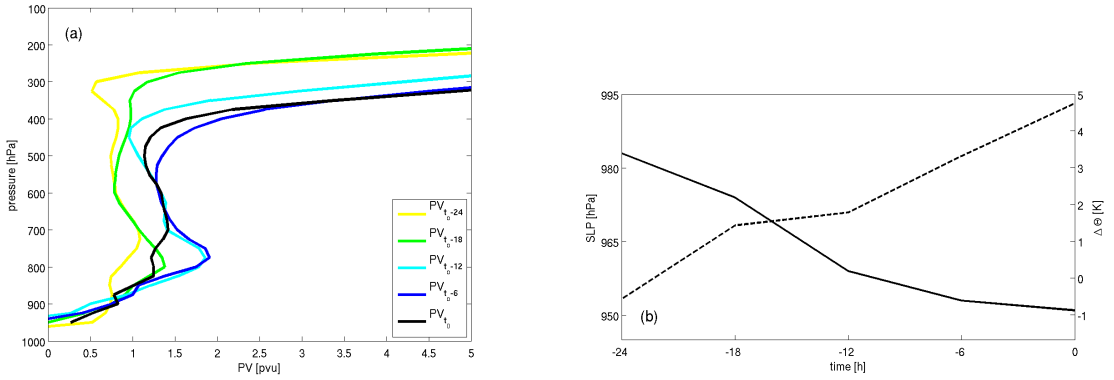

Figure 4.3: Evolution of the vertical PV profile (a), surface Θ anomaly (dashed line) and central SLP (solid line) (b) in the centre of the Atlantic cyclone. Colours indicate different times of the cyclone evolution: time of minimum SLP t_0 (black), $t_0 - 6$ h (blue), $t_0 - 12$ h (cyan), $t_0 - 18$ h (green) and $t_0 - 24$ h (yellow).

looked for evaporative moisture sources along them. Each panel of Fig. 4.4 shows two sets of trajectories, one coming from the PV tower of the cyclone at t_0, and the other one from the PV production regions along the first set of trajectories at different times $t \leq t_0$. The first trajectory set is coloured according to PV and the second set is coloured with specific humidity, q. This shows where the PV that can later be found in the centre of the cyclone is produced and where the longer trajectories, which lead to the PV production, pick up their moisture. Black dots denote the starting point of the long backward trajectories, i.e., the place of PV production. Most of the PV production takes place $6 - 12$ h prior to t_0, and therefore most of the long trajectories start at these times. The PV production takes place in the vicinity of the cyclone centre; hence the trajectories that are involved in the production at earlier times are located more to the south than the others, because the cyclone came from the southwest.

In Fig. 4.4a 10-day backward trajectories started at 12 UTC 8 February are shown besides those coming from the cyclone centre at 06 UTC 9 February. As shown in fig. 4.2b, a positive PV anomaly is already present in the cyclone centre at that time, however, not much of this PV remains in the centre until it reaches the maximum intensity. Therefore, not many backward trajectories were started at this early time. They started to collect moisture 72-48 hours before the time of PV production (see Fig. 4.6b), which took place when the cyclone reached the position of moist air parcels. PV production in these air parcels is not limited only to this time step, it can be produced also earlier or later and also reach the cyclone centre at different times. But only the PV produced at this time ends in the cyclone centre at the time of its maximum intensity, which we were interested in. The highest PV values in the centre (seen as red parts of the first set of trajectories in Fig. 4.4a) were produced in the next 12 hours. Most of the moist trajectories meet the

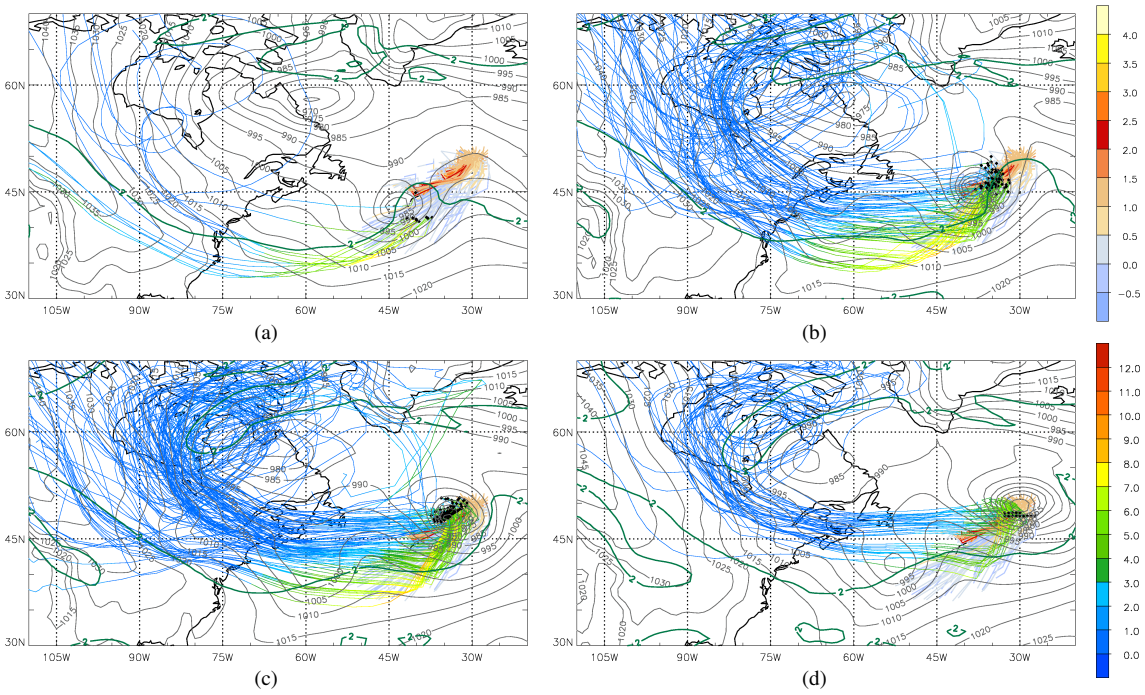

Figure 4.4: First set of backward trajectories started from the cyclone centre (coloured with PV in PVU; upper colorbar), and second set of trajectories started at the PV production locations of the first set (coloured with specific humidity in g/kg; lower colorbar). For the first set of trajectories only the first 24 hours are shown. Black dots mark the positions of the second set of trajectories at their starting point. Panels are for PV production at (a) 12 UTC 8 February 2007, (b) 18 UTC 8 February, (c) 00 UTC 9 February 2007, and (d) 06 UTC 9 February. Also shown is SLP (grey contours) and 2 PVU contour at 250 hPa (bold green line) at these times. Every 4th trajectory is shown.

cyclone in this time interval (Figs. 4.4b,c). We can see that the northernmost trajectories remain dry much longer than the southern parcels (compare blueish colours along northern trajetories compared to yellow and orange colours of the southern trajectories). In the last time step, again less trajectories meet the cyclone and less PV is produced (Fig. 4.4d). Although the air was moist for a longer period of time the PV that we find in the cyclone centre was produced in the direct vicinity of the cyclone and was not advected from far away, as we can see from the position of the black dots relative to the cyclone centre in Fig. 4.4.

Figure 4.5 shows all trajectories from the four panels in Fig. 4.4 in order to illustrate the pathway of the air parcels relative to the evolving synoptic-scale situation. The positions of air parcels at different times are highlighted by black dots and the trajectories are colored by their pressure value. The trajectories originate to the northwest of the cyclone. Many air parcels arriving from the region of the Hudson Bay and Labrador Sea are involved in the PV production at the latest stage (compare with Fig. 4.4d). The most distant

origin of air parcels that reach the cyclone is in the Arctic Ocean. The air parcels cross the whole North American continent, arrive as south as 35°N and then move eastward till they become involved in the cyclone.

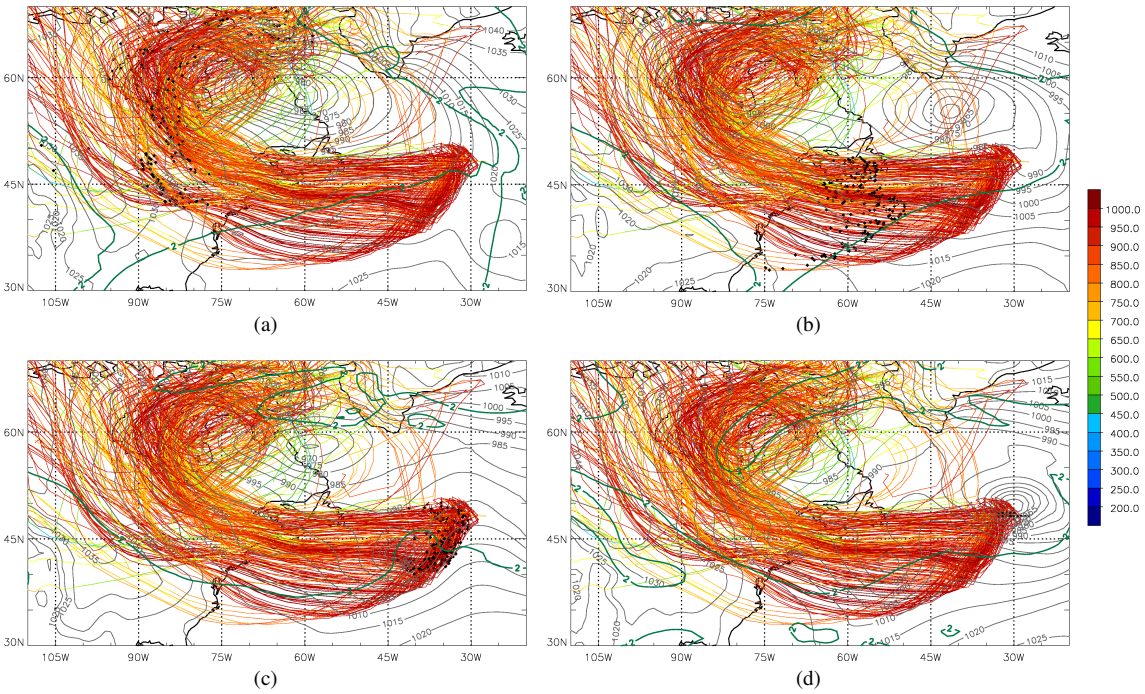

Figure 4.5: All backward trajectories from the second set coloured with pressure (in hPa). Air parcel positions (black dots), SLP (grey contours, interval 5 hPa) and 2 PVU contour at 250 hPa (bold green line) are shown at (a) 00 UTC 5 February 2007, (b) 00 UTC 7 February 2007, (c) 12 UTC 8 February, and (d) 06 UTC 9 February 2007. Every 4th trajectory is shown.

From 3 February onward an intense cyclone is situated over Newfoundland and Labrador. It strongly steers the low-level flow. The air parcels travel south and later east along its western flank (black dots in Fig. 4.5a). On 6 February the first trajectories reach the Atlantic coast and continue moving eastward across the North Atlantic. On 7 February all trajectories reach the North Atlantic (Fig.4.5b). Along the way they gain moisture from the ocean (see colour change from blue to yellow along trajectories in Fig. 4.4). At that time the investigated cyclone does not exist yet. The cyclone develops in a very moist environment, which is favourable for diabatic PV production. Figures 4.5c, d show parcel positions at the first and the last time of PV production, respectively. Before the production sets in the moist air parcels are located east of the cylcone. The cyclone moves faster than the air parcels and catches in with them.

Figure 4.5 shows that at least after 00 UTC 7 February there is not very much variability of the height of the trajectories. But still, their moisture content is quite different (Fig. 4.4). This difference is strongest in the meridional direction - the air parcels with the southernmost path contain more moisture than those further north. To investigate these

differences we divide air parcels into three groups according to their position at 00 UTC 7 February. The first group includes air parcels with latitude lower than $40°$N, the second those situated between 40 and $45°$N, and the rest of the parcels builds the third group. Figure 4.6 shows the height and moisture content of the trajectories in the three groups during the 10 days before they reach the PV production region. Here, the colours correspond to the three groups: the southernmost trajectories are couloured in red, the trajectories in the middle in green, and the northernmost in blue. The time runs from the start of trajectories, therefore time along trajectories is not the same in the absolute sense, i.e. -24 hours means 06 UTC 8 February for the trajectories involved in PV production at 06 UTC 9 February, and 12 UTC 7 February for those starting at 12 UTC 8 February.

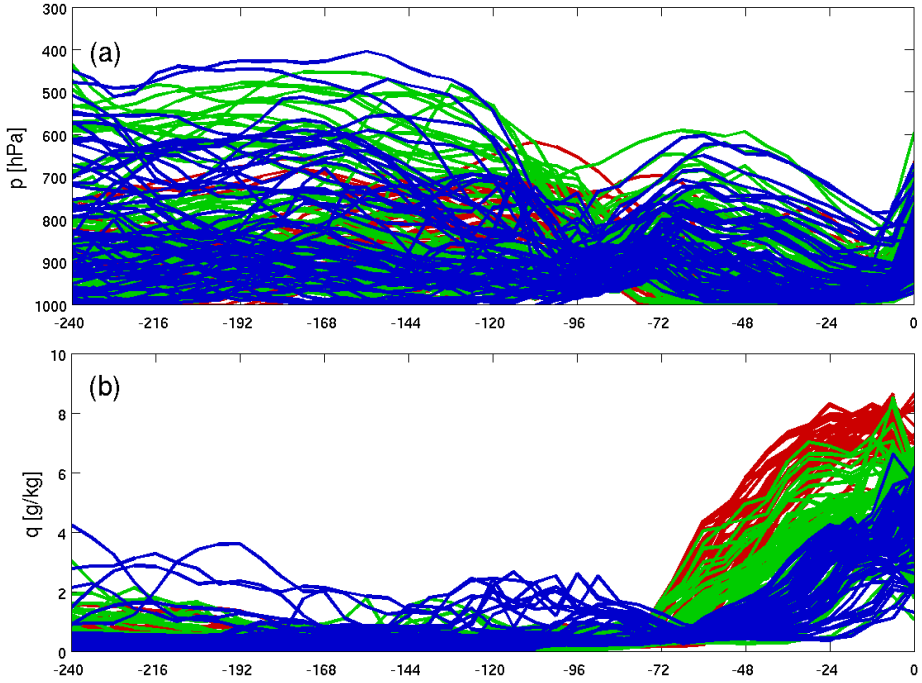

Figure 4.6: Evolution of pressure and specific humidity along trajectories ending in the PV production region in the vicinity of the Atlantic cyclone. Colours corespond to the three clusters (see text for explanation). Every third trajectory is shown.

In Fig. 4.6a we see that the southernmost trajectories are also the lowest. They spend almost all the time below 700 hPa. The trajectories from the other two groups show more variability in the first 6 days. However, in the last 4 days most of the trajectories are below 700 hPa. The earliest moisture uptakes start 3 days before the end of trajectories (Fig. 4.6b). The onset is the earliest for the red trajectories and the latest for the blue trajectories. The time span between the uptakes is more than 48 hours and even larger in absolute sense, if we consider that red trajectories mostly start earlier than the blue trajectories.

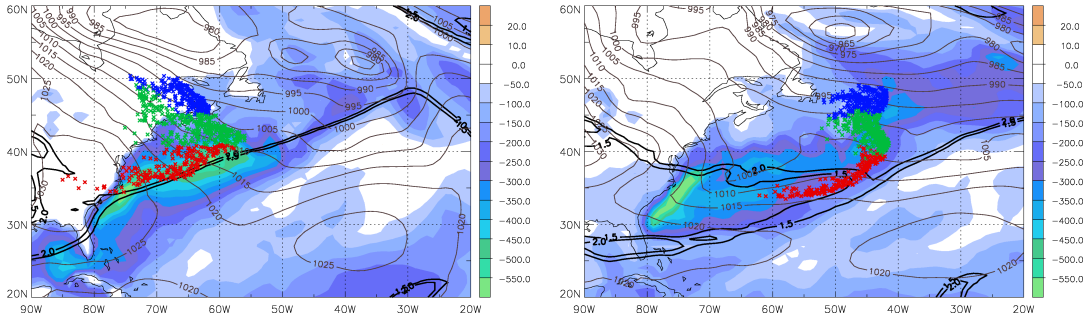

(a) (b)

Figure 4.7: Surface latent heat flux (in colours; $\mathrm{W/m^2}$) and trajectory positions at (a) 12 UTC 6 February 2007, (b) 18 UTC 7 February 2007. Trajectories are coloured according to their positions at 00 UTC 7 February; red: south of $40°$, green: between $40°$ and $45°$, blue: north of $45°$. Also shown are SLP (grey contours, interval 5 hPa) and 2 PVU contour at 250 hPa (bold black line).

To address these differences, we looked at the distribution of the surface latent heat flux. Evaporation from the surface is supposed to be the major source of moisture for our air parcels (remember that only moisture uptakes within the boundary layer are considered in this study). Therefore we expect to see differences in the latent heat flux at the positions of air parcels. Figure 4.7 shows the surface latent heat flux and air parcel positions at two times before the cyclone formation. Parcel positions are depicted in the same colours as in Fig. 4.6. The earliest air parcels reach the ocean at about 00 UTC 6 February. A region of enhanced upward flux extends along the coast and further into the Atlantic ocean. Figure 4.7a shows the situation at 12 UTC 6 February. Almost all red air parcels are located above the region of strong latent heat flux and can therefore receive large amounts of water vapour. Also some of the green parcels reach this region at its northern flank. These parcels exhibit similar characteristics as the red ones in Fig. 4.6b. However they reach slightly lower values of specific humidity, because they are further away from the maximum of the latent heat flux and they also move away from it earlier. Later a new region of enhanced latent heat flux develops between 45-$35°$W and 40-$50°$N connected to another cyclone to the north. The blue parcels gain their moisture from this region. The moment when the first blue parcels reach the second region of enhanced surface latent heat flux is shown in Fig. 4.7b (at 18 UTC 7 February).

Figure 4.8 presents the evaporative moisture uptakes integrated over all considered air parcels along their way before they contribute to the diabatic PV formation in the cyclone center. The uptake region extends over the whole western part of the North Atlantic, from 75 to 30°W and 35 to 50°N. Note that for this case the moisture uptakes are located along the track of the cyclone (solid black line) and extend about 1000 km to the west of the location of cyclogenesis. A small part of its moisture originates also from the Labrador sea and the Great Lakes region.

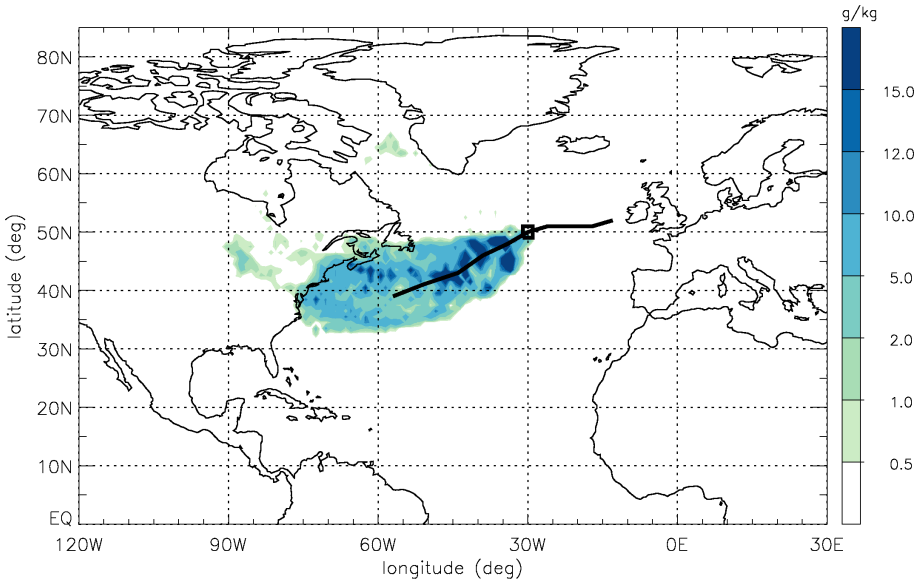

Figure 4.8: Integrated moisture uptakes for the North Atlantic cyclone. Units are g/kg per $10000\,\mathrm{m}^2$. The black line shows the cyclone track, and the black square the location of the cyclone at its time of maximum intensity.

4.3.2 North Pacific cyclone

In contrast to the North Atlantic case study, a second example is shown here, where moisture uptakes cover a smaller area only. This cyclone developed south of Japan on 31 December 2000 and moved towards the northeast.

Before the cyclogenesis a tropical cyclone *Soulik* was situated at 130°E and 14°N to the east of the Philippines. The northward flow steered by the tropical cyclone impinges upon a southward flow caused by a weak cyclone to the north in a region of enhanced baroclinicity (not shown here). This results in a strong convergence zone located at 25°N between 125 and 140°E. Lifting of air and strong latent heat release occur in this region which produce a positive low-level PV anomaly. From this PV anomaly a low pressure system emerges. The cyclone was first identified at 00 UTC 31 December 2000 at 135°E and 26°N. Figure 4.9a shows the cyclone at 12 UTC 31 December. It is located at 144°E and 31°N and has a central SLP of 985 hPa. Low-level PV values in its centre are already higher than 3 PVU. In this stage it has all characteristics of a diabatic Rossby wave (more about it in Chapter 5). There is an anticyclone downstream at 163°E and 37°N, which will play a very important role in recurving trajectories. Twenty-four hours later the cyclone reaches its maximum intensity. Located at 153°E and 42°N it has a central SLP of 948 hPa and extremely high PV values in the centre (Fig. 4.9b). It has deepend 37 hPa in the last 24 hours.

Also a look at the evolution of the vertical profile of PV in the cyclone centre reveals extremely high values in the lower troposphere (Fig. 4.10a). At $t_0 - 24\,\mathrm{h}$, averaged PV

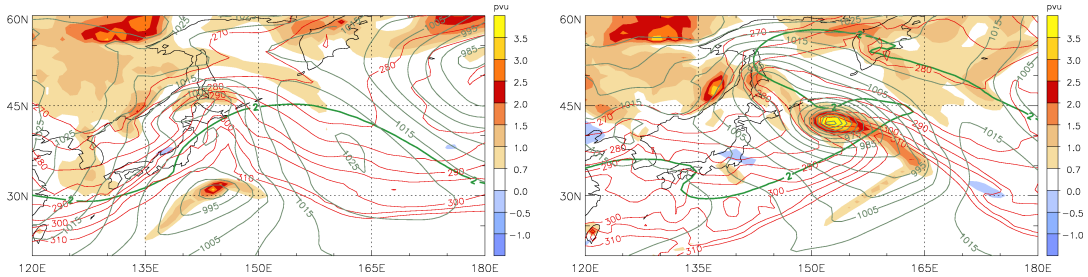

Figure 4.9: Development of the North Pacific cyclone at (a) 12 UTC 31 December 2000 and (b) 12 UTC 1 January 2001. Shown are PV at 850 hPa (colours, in PVU), SLP (grey contours, every 5 hPa), pot. temperature at 850 hPa (red contours, every 5 K), and the 2 PVU contour at 250 hPa (green bold line).

values at low levels exceed 1.7 PVU, which is 1.4 PVU higher than the climatology. 24 hours later, average central PV values are 3 PVU higher than the background value. Also surface potential temperature anomalies are very high (Fig. 4.10b). On the other hand, the upper-level PV anomaly is rather weak. Compared to the Atlantic cyclone, which experienced comparatively similar rapid deepening, this cyclone has more low-level PV and a stronger surface potential temperature anomaly, but the Atlantic cyclone has a much more intense upper-level PV anomaly.

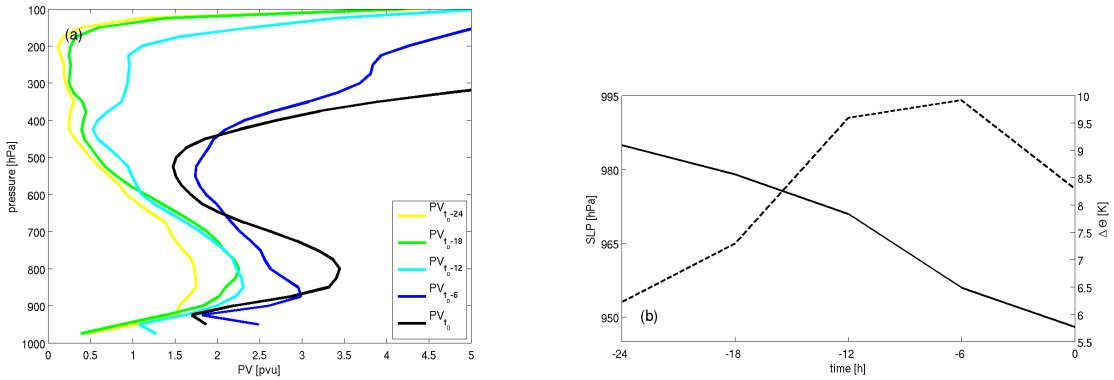

Figure 4.10: Evolution of the vertical PV profile (a), surface Θ anomaly (dashed line) and central SLP (solid line) (b) in the centre of the Pacific cyclone. Colours indicate different times of the cyclone evolution: time of minimum SLP t_0 (black), $t_0 - 6$ h (blue), $t_0 - 12$ h (cyan), $t_0 - 18$ h (green) and $t_0 - 24$ h (yellow).

The same procedure of calculating backward trajectories and identifying moisture sources was applied to this cyclone. The 10-day backward trajectories started at locations of PV production are displayed in Fig. 4.11. As in the Atlantic case, PV that was

found in the cyclone centre at the time of its maximum intensity t_0 (i.e., 12 UTC 1 January 2000) was produced in the last twenty-four hours of the cyclone life time. The strongest PV production takes place $6 - 12$ h before t_0.

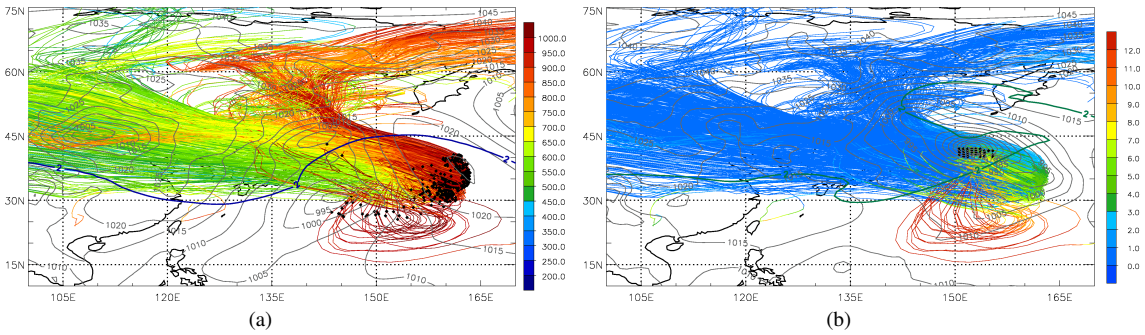

(a) (b)

Figure 4.11: Backward trajectories started at all PV production locations. Marks of air parcel positions (black dots), SLP (grey contours, every 5 hPa) and 2 PVU contour at 250 hPa are shown at (a) 12 UTC 31 December 2000 (in colours pressure along trajectories (hPa)) and (b) 12 UTC 01 January 2001 (in colours specific humidity (g/kg)).

We can distinguish three bundles of trajectories connected with this cyclone (see Fig. 4.11). Trajectories originating in the Arctic Ocean traveled at an altitude of approximately $900 - 800$ hPa (redish colours in Fig. 4.11a). They are dry (blueish colours in Fig. 4.11b) and don't collect moisture until they arrive close to the cyclone. The second bundle also starts at low levels, in the northeastern part of Russia. These trajectories first travel south, collect moisture as they reach the ocean east of Japan and then make a loop before entering the cyclone. Trajectories arriving from the west from heights between 550 and 250 hPa are very dry at the beginning. They travel past the location of the cyclone and when they arrive into the center of an anticyclone downstream they descend rapidly, turn their direction and arrive at the cyclone center after collecting a significant amount of moisture east of the cyclone. We investigate the evolution of the air parcel characteristics along trajectories in the three clusters. In Fig. 4.12, the western trajectories are colured in red, those coming from the north in green, and the lowest trajectories looping south of the cyclone in blue. The green group includes air parcels originating from the region to the east of $130°$E and north of $60°$N. Most of these parcels travel directly towards the cyclone, but some of them join the parcels in the loop in the south. We will treat them here as a part of the blue cluster.

The three clusters exhibit much larger variability than the trajectories in the Atlantic case. In Fig. 4.12 changes of height and moisture along trajectories are shown. The air parcels in the red cluster originate from all tropospheric levels over the Atlantic, Europe and North Africa. When travelling over Asia they all rise to altitudes higher than 700 hPa and only start to return to lower levels when they get involved in an anticyclone over Japan and move with it to the east. The green parcels remain below 700 hPa almost all the time. Shortly before they arrive in the cyclone they enter the anticyclone and descend further

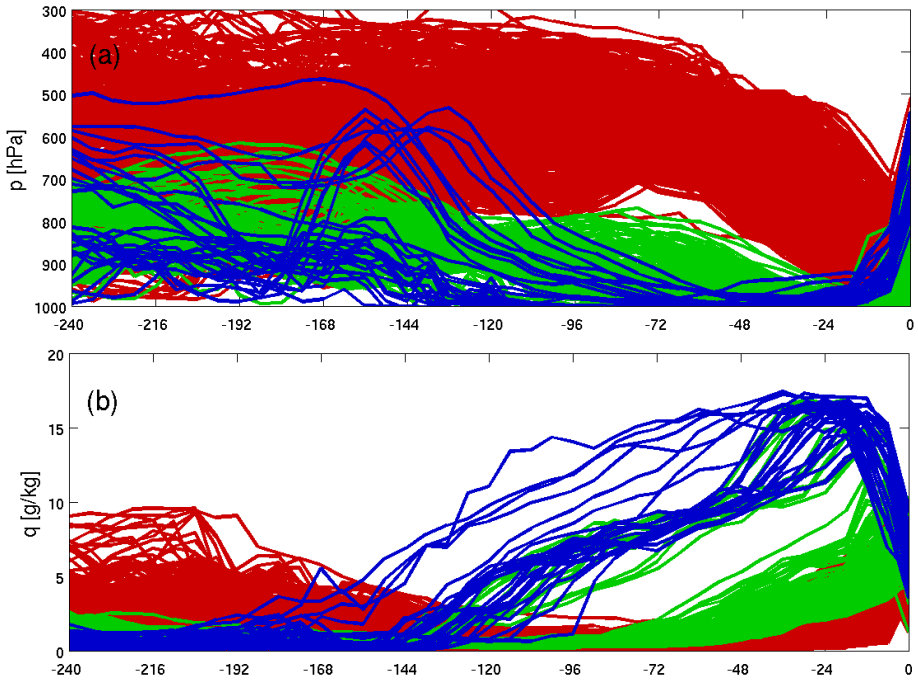

Figure 4.12: Evolution of pressure and specific humidity along trajectories ending in the PV production region in the vicinity of the Pacific cyclone. Colours corespond to the three clusters (see text for explanation). Every fifth trajectory is shown.

almost to the surface. The third, blue cluster, contains air parcels that originate from very different regions, to the west, north and east of the cyclogenesis region. The blue parcels coming from the north travel at low levels all the time, others descend to the surface at the latest after 5 days. They have in common that they reach the ocean much earlier than the other air parcels and they gain high amounts of moisture very early (Fig. 4.12b). The parcels from the green and red cluster collect their moisture in the last three or two days, respectively.

A comparison of parcel positions and the distribution of the surface latent heat flux in Fig. 4.13 shows where air parcels collected their moisture. At 00 UTC 27 December (Fig. 4.13a) there is a large region of enhanced upward latent heat flux extending to the south and east of Japan. Most of the blue air parcels are located above or near the region of the strongest flux where they gain most of their moisture. 36 hours later, at 12 UTC 29 December, we can see also the red and the green cluster arriving over the ocean in Fig. 4.13b. At this time, the green parcels are on average approximately 300 hPa lower than the red ones. The corresponding time in Fig. 4.12 is approximately -72 hours. The green parcels slowly start collecting moisture, however slower than the parcels in the blue cluster did 72 hours earlier (compare Fig. 4.12b). The evaporation from the sea surface is much weaker at this time, therefore the moisture content of all particles, including the

blue ones, rises slower. In Fig. 4.12c we can see red and green parcels at 00 UTC 31 December in the centre of an anticyclone that forces them to descend and change their direction. Shortly before they get involved into the cyclone, at 18 UTC 31 December, also red and green parcels impinge on a region of strong surface latent heat flux close to the cyclone (Fig. 4.12d). However, they never reach the amount of moisture that the blue parcels contain.

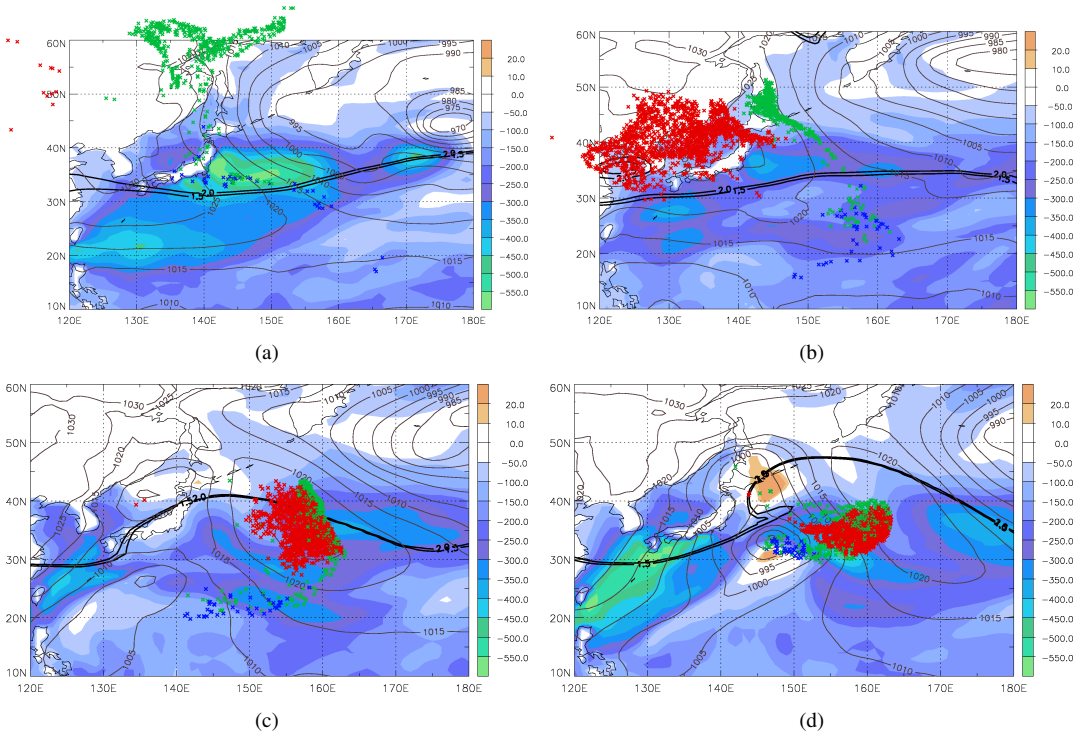

Figure 4.13: Surface latent heat flux (in colours) and trajectory positions at (a) 00 UTC 27 December, (b) 12 UTC 29 November, (c) 00 UTC 31 December, and (d) 18 UTC 31 December 2000. Trajectories are coloured according to the three clusters (see text for explanation); red: parcels from the west, green: parcels from the north, blue: parcels from the moist loop; Also shown are SLP (grey contours, interval 5 hPa) and 2 PVU contour at 250 hPa (bold black line).

The integrated moisture uptake region for this cyclone is shown in Fig. 4.14. The region is much smaller and more focused than in the case of the Atlantic cyclone. The southern and weaker part of the uptake region belongs to blue trajectories and the northern and stronger part to green and red trajectories. The blue parcels clearly contained more moisture than the other parcels, but there were 20 times more red than blue parcels and 4 times more green than blue parcels. This adds up to the strong uptake that we can see in Fig. 4.14.

High values of integrated moisture uptake in the Pacific case compared to the Atlantic case correspond to differences in low-level PV in the two cases. However we have to keep in mind that the uptake region is smaller in the Pacific case.

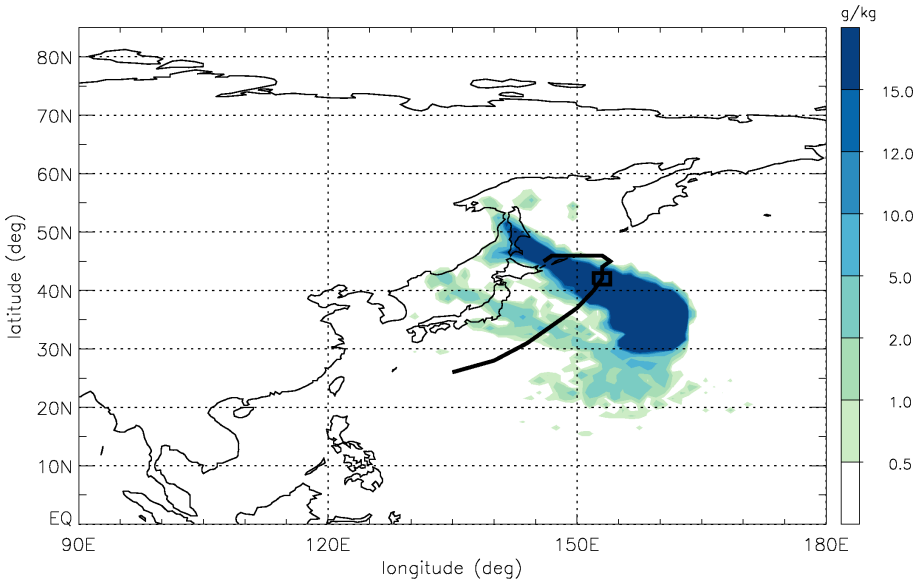

Figure 4.14: Same as Fig. 4.8, but for the North Pacific cyclone.

4.4 Climatological evaporative moisture source regions

We conducted the Lagrangian analysis of evaporative moisture sources involved in the diabatic PV production for all DJF cyclones in the regions defined in the previous chapter. Composite fields of evaporative moisture uptake regions are presented in Figs. 4.15 - 4.18. The boxes where the cyclones reached their minimum SLP are outlined in each figure. No results are shown if the number of cyclones in a category, for which we were able to identify moisture sources, is less than 10 to ensure reliability. Also the cyclones in which no moisture uptakes were recorded (mostly the weakest cyclones) are included in this composite analysis.

Composite moisture source regions for the cyclones with the minimum SLP near Alaska and Greenland are displayed in Fig. 4.15. The uppermost panels include very intense cyclones with minimum SLP between 930 and 970 hPa, the second upper panels those with minimum SLP between 970 and 990 hPa. The composites for weaker cyclones are shown in the lower panels, for cyclones with minimum SLP between 990 and 1010 hPa in the second lowest panels and for the weakest cyclones (SLP between 1010 and 1030 hPa) in the lowermost panels. This arrangement is the same also for Figs. 4.16, 4.17 and 4.18. The white region along the dateline is an artefact of the data format and does not appear in reality.

Clearly, the composites cannot show the full variability of the single cyclone's moisture uptake fields. Moisture source regions for individual cases can vary strongly from the mean field, as presented in the two case studies above. Alaskan cyclones from the strongest two classes (Figs. 4.15 a,b) collect their moisture in large areas over the North

Pacific and the uptakes are well spread over the whole region. However the values are not very high. Moisture sources of weaker cyclones (Figs. 4.15 c) are more limited to the eastern part of the North Pacific. The amplitude of moisture uptakes is more variable for the cyclones in the vicinity of Greenland. The uptake region extends from the coast of the Carolinas in the south-west to Spitsbergen in the north-east. There is a maximum south of Greenland with values higher than 2 g/kg per 10000 m^2 in the two strongest cyclone classes (Figs. 4.15 e,f). Weaker cyclones in this region are not associated with intense moisture uptakes and diabatic PV production (Figs. 4.15 g,h). These two cyclone classes have the smallest uptake regions with the lowest integrated values of specific humidity compared to cyclones in other regions.

For western European cyclones (Figs. 4.16 left), we notice a steady decrease of amplitude and spatial extent of the moisture uptake region with cyclone intensity. The strongest cyclones receive their moisture only from the Atlantic, with contributions from the Great Lakes region and the Labrador Sea. For cyclones in other three classes, the Mediterranean also plays a role as an uptake region. The most intense cyclones typically cross this box in the upper left corner and the weakest in the lower right corner as shown in Fig. 3.8 in Chapter 3. The uptake field for the weakest western European cyclones is very localised in the vicinity of the cyclones. Also in the Mediterranean (Figs. 4.16 right) we see contributions from both basins, the Atlantic and the Mediterranean. However, the contribution from the Atlantic is large only for the strongest cyclones (remember that no cyclones with the minimum SLP lower than 970 hPa were found in the Mediterranean). The cyclones in the first two intensity classes receive some moisture also from the Black Sea. The distribution of moisture sources within the Mediterranean Sea is very similar in Figs. 4.16f and h, only the intensity is different. The maxima in moisture uptake correspond well to maxima in cyclone frequency in the region (Campins et al. 2011).

In Figs. 4.17 and 4.18 we again see the differences that we have already seen in the case studies above. The uptake regions are remarkably larger for cyclones intensifying in the eastern parts of the oceans. For the cylones in the eastern Atlantic, the uptakes extend over 60° longitude, whereas the western Atlantic cyclones only collect water along about 30°. Obviously, the trajectories that end in the PV production region mostly come from the west, therefore they have more time to collect moisture. This is confirmed by the investigation of moisture uptakes along the trajectories (last column in Fig. 4.19). In the western North Pacific, the earliest uptakes on average take place 4 days before PV production, while in the eastern North Pacific it happens already 3-4 days earlier. The differences are less obvious in the North Atlantic, however the comparison is exacerbated due to unsufficient data from the strongest and the weakest cyclones. Although the western uptake regions are smaller, the uptake values are much higher. The most likely reason for it is that the trajectories collect moisture in a small region in the vicinity of a cyclone. Gridded data therefore exhibits higher values.

Almost all moisture was collected over the oceans. Evapotranspiration from land does not seem to play an important role. The inspection of single trajectories reveals that some moisture also originates from terrestrial sources, but they are much smaller than the up-

takes from the oceans. Only western North Atlantic cyclones have a considerable contribution from the continent (Fig. 4.18 left).

Surprisingly, most trajectories typically do not originate from low-levels in the cyclone's warm sector but rather come from further away and mostly from high levels. On average, the trajectories descend strongly in the last days before the PV production, collect moisture and then quickly rise in the last $12 - 24$ hours, producing latent heating and therefore a good environment for PV production. Figure 4.19 shows average values of pressure, PV, relative humidity, specific humidity and moisture uptakes along the trajectories in each region and intensity class.

The average values along trajectories are rather unexpected. Only in Alaskan cyclones max. values of specific humidity increase with intensity. Almost everywhere else trajectories from more intense cyclones are drier. However, it is possible that water rains out more often in these cyclones but we can only detect net changes of humidity. Average specific humidity along trajectories often increases earlier than the identified uptakes begin. These air parcels gain moisture outside of the boundary layer from sources, which we cannot identify. Very special examples are cyclones from the third intensity class in Greenland and western Europe that have higher values of specific humidity than other cyclones in these regions but lower identified evaporative moisture uptakes. Here an even larger amount of moisture comes from unidentified sources.

Although the trajectories in intense cyclones seem to be drier, the overall uptakes are still larger than in weaker cyclones as presented in Figs. 4.15 - 4.18. Usually stronger cyclones have appreciably more trajectories from diabatic PV production regions than weaker cyclones, which results in higher integrated moisture uptake values. In intense cyclones there are more points with $\mathrm{PV} > 1\,\mathrm{PVU}$ in the centre, from which backward trajectories were calculated. However, the results from Fig. 4.19 show us that essential processes leading to PV production are similar in both weak and strong cyclones. For PV production in weak cyclones also enough moisture must be present in order to reach saturation and latent heating.

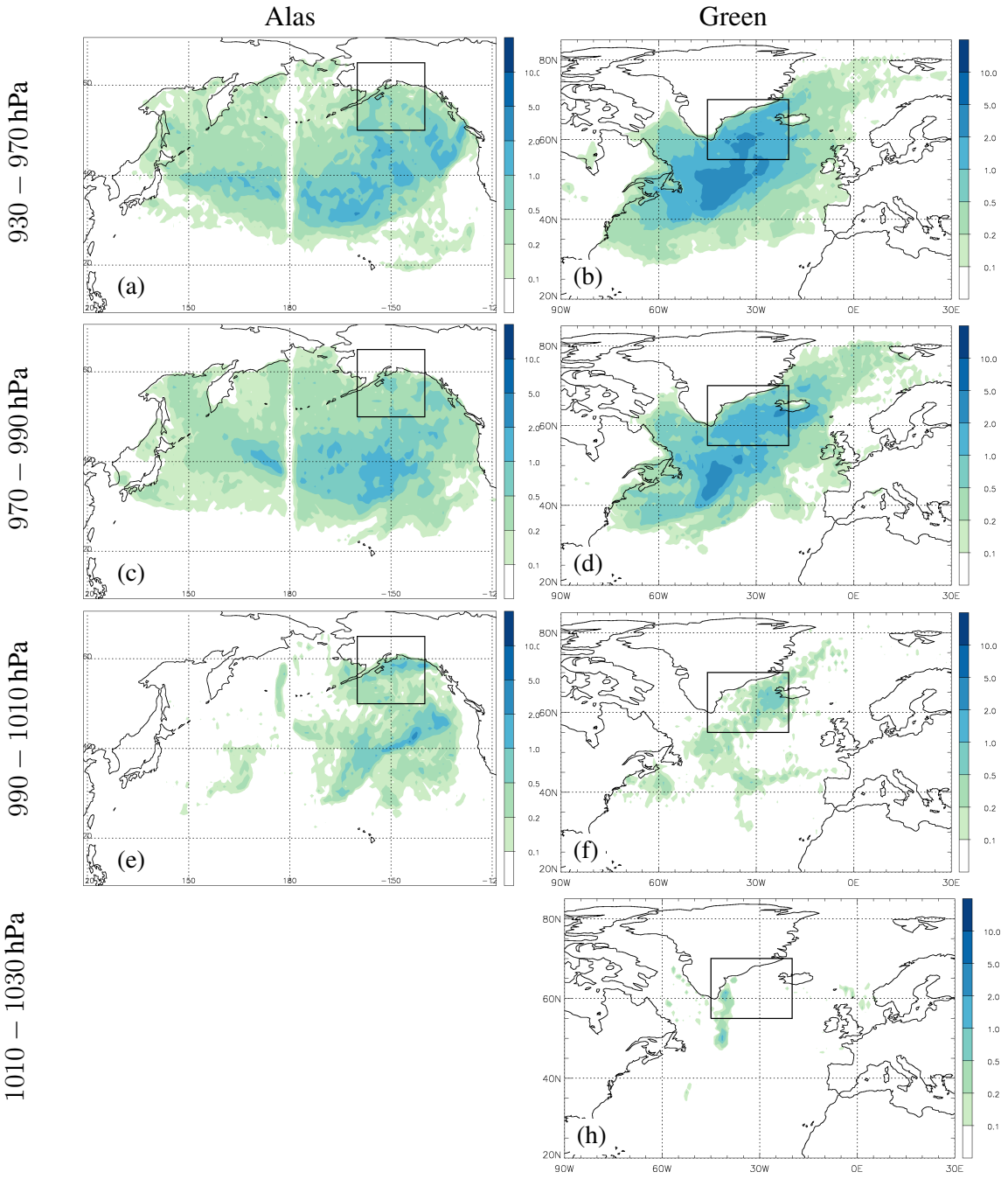

Figure 4.15: A composite moisture uptake field. Units are g/kg per 10000 m^2. Left: Alaskan cyclones, right: Greenland cyclones. The intensity of cyclones is labeled on the left side.

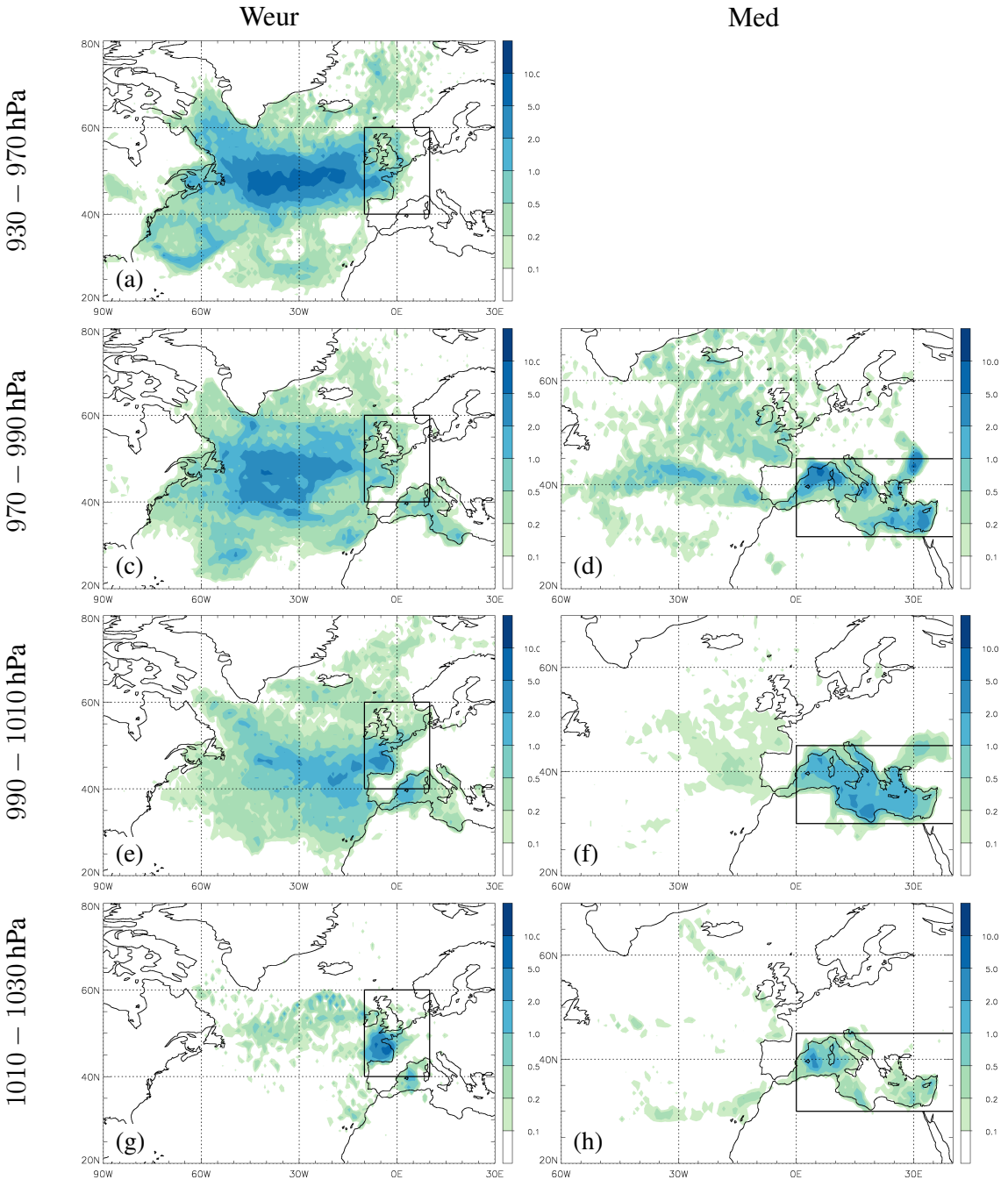

Figure 4.16: Same as fig. 4.15, but for western European cyclones (left) and Mediterranean cyclones (right).

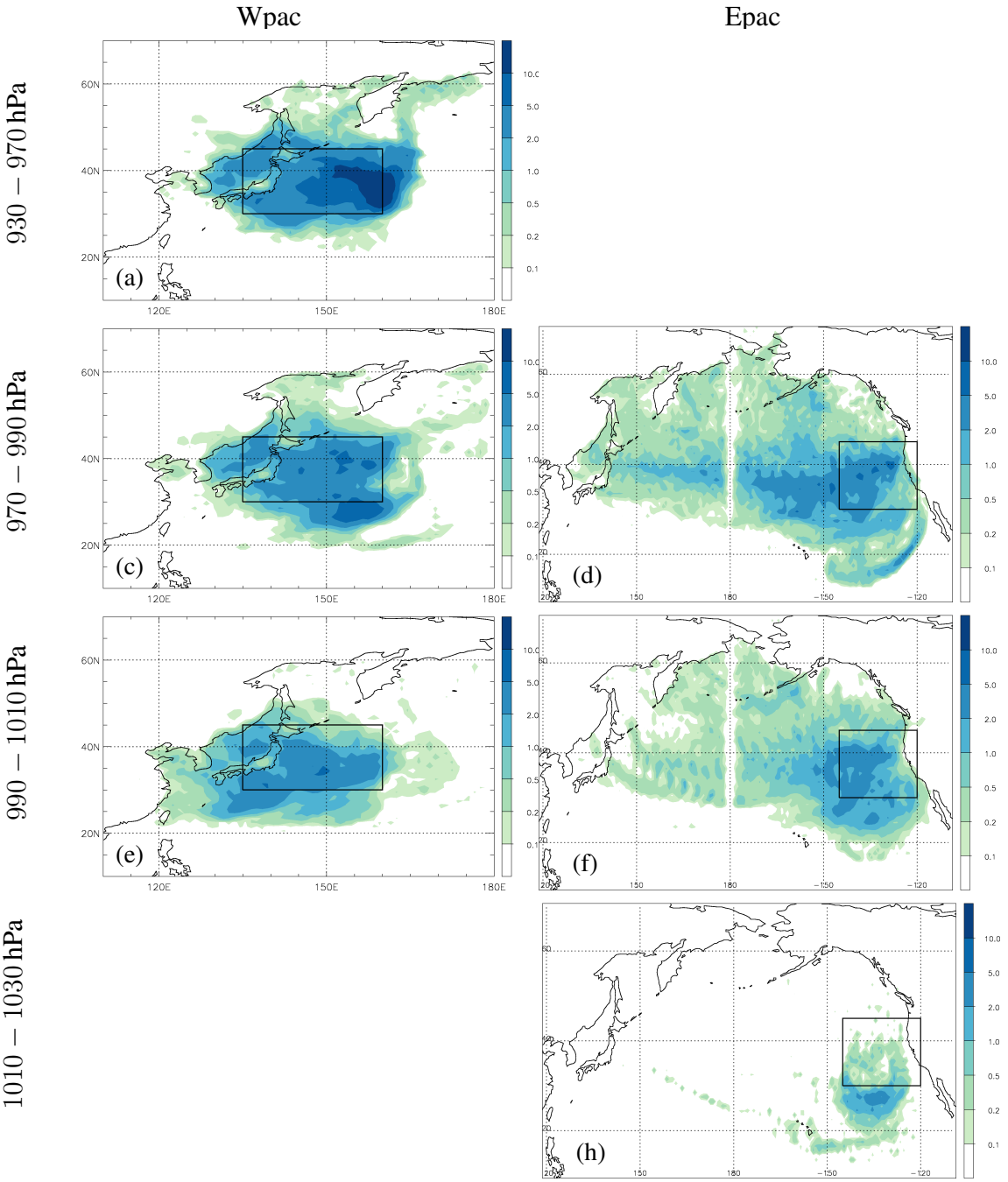

Figure 4.17: Same as fig. 4.15, but for western (left) and eastern (right) North Pacific cyclones.

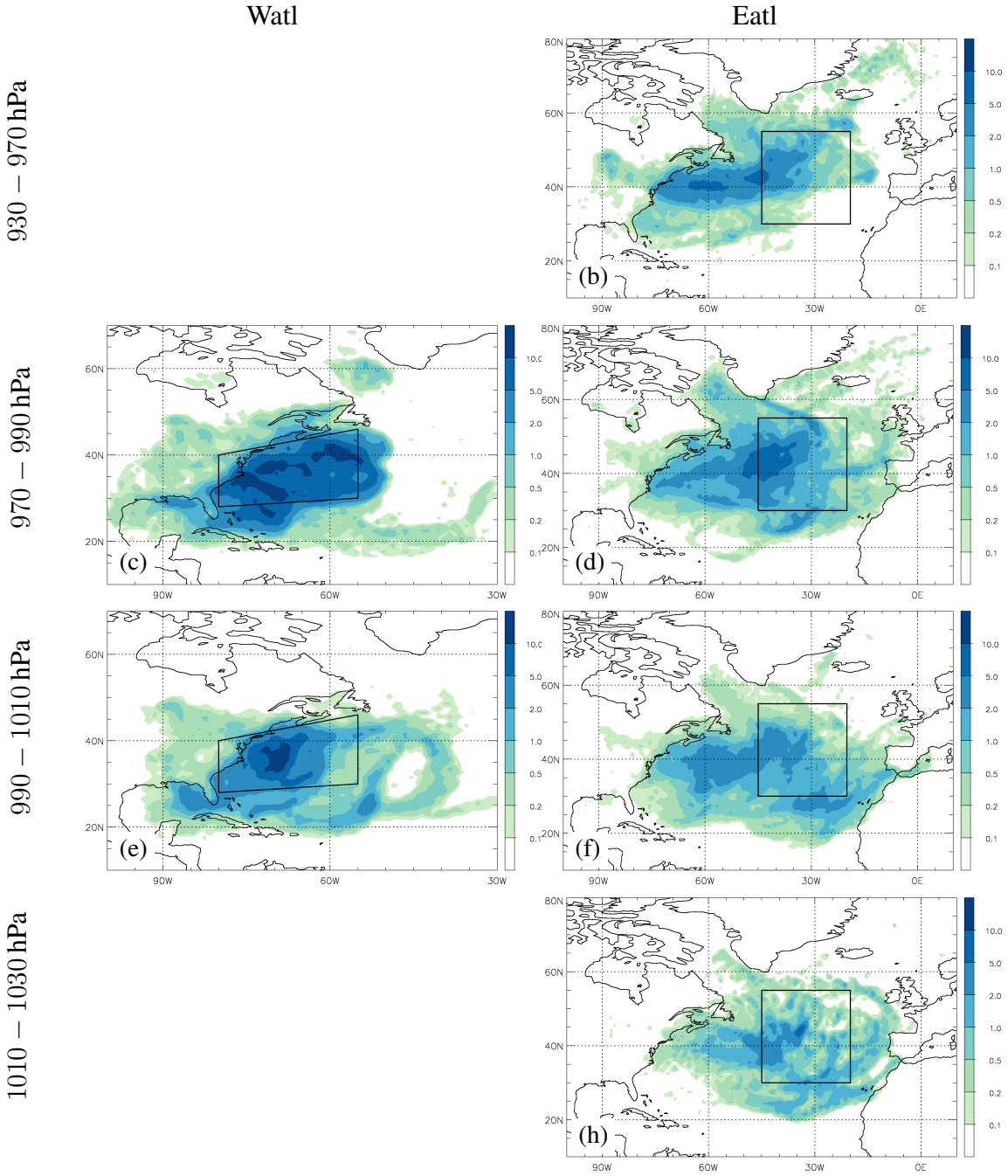

Figure 4.18: Same as fig. 4.15, but for western (left) and eastern (right) North Atlantic cyclones.

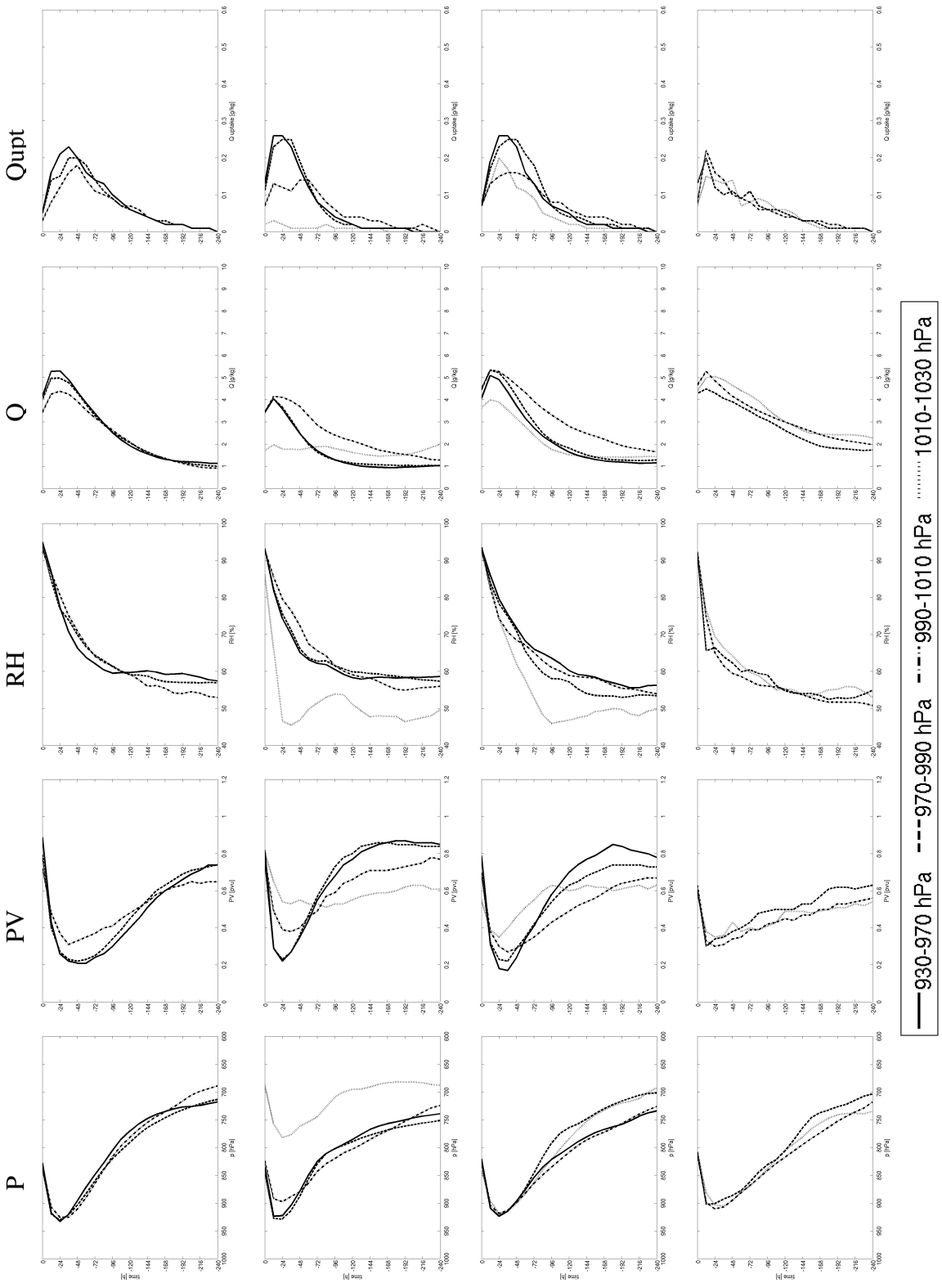
P
PV
RH
Q
Qupt
Alas
Green
Weur
Med
930-970 hPa
970-990 hPa
990-1010 hPa
1010-1030 hPa

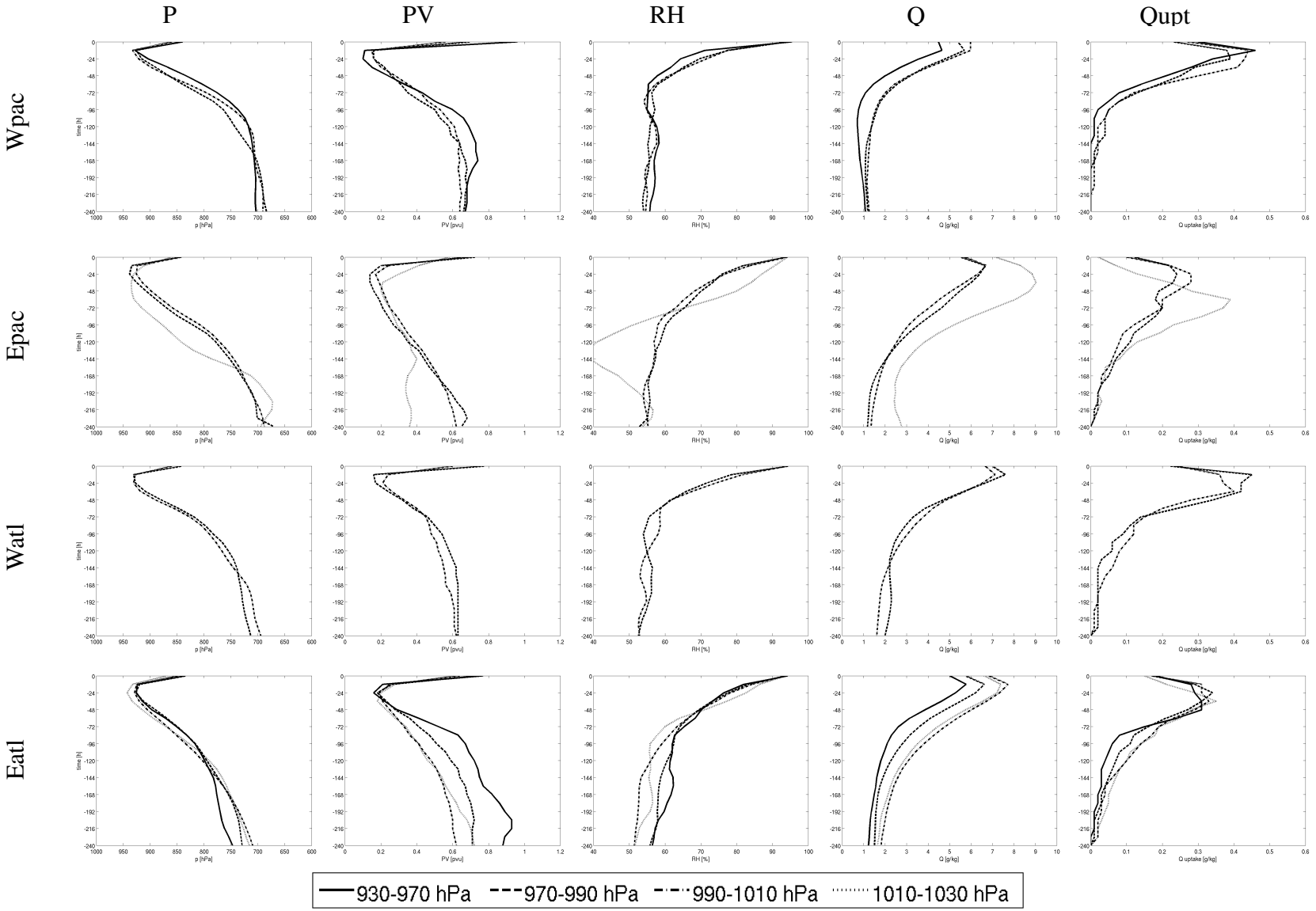

Figure 4.19: Time evolution of averaged values of variables along the second set of trajectories for different categories of cyclones.

4.5 Summary and discussion

The Lagrangian approach allows to identify the sources of water vapour that play an important role in low-level PV production. We have investigated the evaporative moisture sources of extratropical cyclones in several regions. We have found large variability between the cyclones in different regions but also between cyclones of different intensity within one region. Case to case variability is larger than the variability between the averages for different cyclone intensities.

Most of the PV in the cyclone centre is produced in the last 18 hours of the intensification phase. The average values along backward trajectories reveal that most trajectories come from higher levels and descend strongly before the time of PV production. Mainly, water uptakes take place from 0 up to 6 days prior to PV production with maxima between -12 and -48 hours. In the last 12-24 hours, the air parcels strongly rise, precipitate and gain PV.

The water uptake regions are on average larger for the cyclones in the eastern parts of the oceans. Here the air parcels travelled a longer way over the ocean where they could take up more moisture. In the western oceans, evaporation occurs in more confined regions, leading to higher gridded values of moisture uptakes.

Stohl et al. (2008) found sources of moisture precipitating over Norway spread all over the North Atlantic and reaching all the way to the subtropics. This is somewhat in contrast to our findings. The source regions for the cyclones in the eastern North Atlantic and over western Europe do not extend that far to the south (especially for the strongest cyclones). One possible reason may be that many trajectories leading to intense precipitation might come from regions further south than the trajectories involved in PV production in the centre of the cyclones. It is also likely that the uptakes further back in time are assumed to contribute much less to the final moisture amount with our approach. The method used by Stohl et al. (2008), however, does not account for moisture losses due to precipitation along the trajectories.

Only a very small portion of moisture in our study originates from the continents, which seems to be reasonable, since most of the investigated cyclones develop over oceans. However, many trajectories travelled a long way over the continents. We did not distinguish between the two options, but likely the uptakes above oceans were much larger compared to those above continents. From this point of view the results of Brubaker et al. (2001) and Stohl and James (2005) are surprising. According to the first study, a very large amount of moisture that brings precipitation to the Mississippi basin originates from recycling over the basin itself and over the continent. Stohl and James (2005) confirmed this and additionally found out that in more than half of the investigated river catchments more than 50 % of the precipitation originated over land surfaces. However, this source is most important for rivers that are remote from oceans. The same is the case for the study by Reale et al. (2001). Their flood events in the Mediterranean gained a lot of moisture from terrestrial sources, even though the authors claim that a substantial amount of moisture was advected from the Atlantic ocean with three (ex-)tropical cyclones. As opposed

to that, we do not find any important terrestrial moisture sources for our cyclones. However, the above studies include other seasons than our (warm-season in Brubaker et al. 2001, whole year in Stohl and James 2005 and September-October in Reale et al. 2001). Therefore extending of our investigation to other seasons might be rewarding for better understanding of moisture transport and easier comparison of the results.

Chapter 5

A case study on the effects of low-tropospheric moisture on cyclone intensification with the COSMO model

5.1 Introduction

This case study is motivated by the results of the investigation of oceanic moisture sources for the diabatic production of PV in extratropical cyclones. The objective of this chapter is to investigate the impact of low-tropospheric moisture on the cyclone development at different stages of the cyclone's life-cycle. The COSMO model will be used to simulate the cyclone (reference simulations), and sensitivity experiments will be performed with artificially modified low-tropospheric moisture fields in moisture uptake regions previously identified by the method used in Chapter 4.

Condensation is responsible for PV production in a cyclone at low tropospheric levels. We expect that reduced moisture in the region of the cyclone's low-level inflow will in the first place reduce low-level PV and thereby weaken the cyclone. In the worst case, moisture reduction can even "kill" a cyclone, i.e., inhibit the intensification and further development of a cyclone. Diabatic PV production in front of the cyclone is a mechanism that enhances its propagation velocity. Therefore another consequence of reduced low-tropospheric PV production could be a slower propagation speed. The weakening and the slower propagation can also result in a (strongly) differing cyclone track. A secondary effect of reduced low-tropospheric moisture in potentially ascending air masses are differences at the level of the tropopause. A coherent stream of rising air is associated with most intense cyclones. When lifted, air experiences large changes in PV (e.g., Wernli and Davies 1997). Below the maximum of latent heating the air gains PV. This PV is destructed when the air rises further into the region of a negative vertical gradient of latent heating. Through this mechanism low PV air is transported to the tropopause region where it modifies the Rossby wave pattern (e.g., Grams et al. 2011). Low PV air enhances the ridge in front of the cyclone, typically leading to a shortening of the wavelength of the

upper-level trough and therefore stronger curvature of trajectories of air flowing around it (increase in relative vorticity). From the PV point of view, a stronger ridge makes a positive PV anomaly associated with the trough even more anomalous. The differences in stratification below the anomalies additionally enhance vertical movement. The isentropes are typically lowered below a negative PV anomaly (a ridge) whereas they are lifted below a positive anomaly (trough). When a trough moves towards east, a so called "vacuum cleaner effect" leads to strong vertical movement. The stronger the ridge, the lower the isentropes below it and stronger the effect of lifting when the trough arrives. Furthermore, a ridge slows down the propagation of an upstream trough allowing for easier coupling of the upper-level anomaly with a surface cyclone. Reduced moisture allows less latent heating, less lifting, and therefore leads to a reduced cross-isentropic transport of low-PV air into the upper-level ridge. As a consequence, the upper-level anomalies might be weaker and the interaction with the (weaker) surface cyclone less intense.

We expect these effects to show up in our experiments. Probably, the intensity of each effect will differ depending on the phase of the cyclone evolution. We will look at the evolution of the PV profile in the cyclone, its position and intensity (measured in central SLP). Additionally, the position relative to the jet and upper-level trough and the intensity of the trough will be examined.

The selected case will first be presented by means of ERA-Interim data, followed by a careful inspection of the cyclone development in different sensitivity experiments with the COSMO model.

5.2 Case overview

In this subsection ERA-Interim data are used to provide an overview on the evolution of the considered North Pacific cyclone.

5.2.1 The SLP evolution

The cyclone first appears at 00 UTC 11 November 2005 southwest of Japan, at 128°E, 30°N. Its track and the evolution of its minimum SLP value are presented in Fig. 5.1. The cyclone reaches its maximum intensity after 42 hours at 154°E, 39°N. Afterwards it weakens, but still exists for five more days. The first two days of this cyclone's life cycle are our main interest since the intensification happens then. For this reason and to save computing time we will focus on the first 66 hours of the cyclone's life time, i.e., on the time period from 00 UTC 11 November to 18 UTC 13 November. Therefore we also present only this part of the cyclone evolution with ERA-Interim data.

The life cycle of the cyclone can be divided into two phases. In the first 24 hours the cyclone is confined to the low levels. The cyclone moves fast towards the east, there is no upper-level forcing present, and the low-level PV in the cyclone centre is continuously reproduced by condensational heating. This development corresponds to type A of the

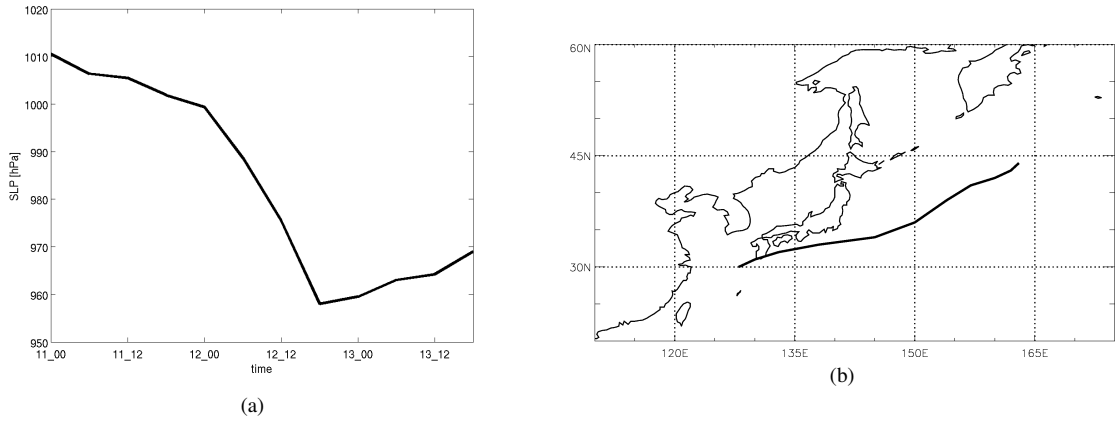

Figure 5.1: a) Time evolution of central SLP [hPa] from 00 UTC 11 November to 18 UTC 13 November 2005 and b) cyclone track in ERA-Interim data.

cyclogenesis classification of Petterssen and Smebye (1971) or to the concept of a diabatic Rossby wave (DRW). The mechanism of a DRW was first thoroughly described in Parker and Thorpe (1995) and later investigated in case studies (Wernli et al. 2002, Moore et al. 2008, Riviere 2010, Böttcher 2010, Böttcher and Wernli 2011) and theoretical studies (Moore and Montgomery 2004, 2005). The theoretical studies found out that the DRW is a robust phenomenon of a moist baroclinic atmosphere, which can exist without an upper-level forcing. The case studies confirmed the importance of moisture, baroclinicity, latent heating and surface fluxes for the existence of a diabatic Rossby wave.

Böttcher and Wernli (2012) compiled a climatology of DRWs and investigated the large-scale flow patterns favourable for the formation of a DRW. They found five situations typical for DRW genesis, which correspond to meridional flows against the mid-latitude baroclinic zone (associated with surface anticyclones, (tropical) cyclones, or upper-level cutoffs), ascent at the baroclinic zone induced by upstream upper-level troughs, and PV remnants, e.g., of a tropical cyclone, advected into the baroclinic zone. The DRW investigated here is a hybrid case, which formed to the west of an anticyclone and to the north of tropical storm *Tembin* that assisted in steering moist air towards the north.

Later, on 12 November, the surface cyclone starts interacting with an upper-level trough and crosses the axis of the upper-level jet. In this period it experiences an extremely strong intensification of more than 40 hPa in 24 hours. The left exit and the right entrance region of a jet are known to be especially prone to cyclogenesis. Riviere and Joly (2006) and Riviere et al. (2010) investigated the role of the low-frequency jet-like flow for the explosive growth of three very intense European winterstorms, especially “Lothar” in December 1999. They introduced the concept of a baroclinic critical region at the end of a jet as the region where explosive growth preferentially takes place. They claimed that the jet determines the location of the growth but its intensity depends on the properties of

a surface cyclone. In our case the jet split when the cyclone approached and the cyclone arrived between the two jets, hence in a region where it was influenced by both jets. This favored the extremely rapid intensification.

5.2.2 The cyclone's PV evolution

Hours before cyclone formation there was precipitation in the genesis region (with a similar pattern as in Fig. 5.3a). According to the reanalysis data only a small part of the precipitation was of convective nature, the rest came from large-scale ascent. A strong baroclinic zone (Fig. 5.2a) extended from the continent far into the Pacific ocean. Between the east coast of China and Japan, northerly flow driven by an anticyclone to the east and a tropical storm to the south brought moist air from the south towards the baroclinic zone where it rose and formed precipitation. An elongated cloud can be seen in the satellite image (Fig. 5.2b) along the baroclinic zone, which confirms the rising motion. In the upper levels a straight jet is aligned with the baroclinic zone.

At 00 UTC 11 November the cyclone (in the form of a DRW) with a central SLP value of 1010.5 hPa is first identified by the cyclone tracking algorithm. Figure 5.2a shows the cyclone 6 hours later, together with a positive low-level PV anomaly in its centre. The maximum of precipitation at the same place amounts to approximately 20 mm/6 h. There was a weak ridge at upper levels to the north of the genesis point, but no trough (i.e., no prominent upper-level forcing for ascent) was present in the vicinity of the evolving DRW.

The cyclone moved eastwards relatively fast and passed to the south of Japan. The amount of precipitation remains relatively unchanged for about 18 hours and is located mainly to the rear but also in front of the surface cyclone (Fig. 5.3c). At upper levels the ridge in front of the cyclone slowly strengthens (see the evolution of the 2-pvu isoline in the figures). After approximately 24 hours, a small positive PV anomaly (connected to intense precipitation) approached the cyclone from the south and merged with it. At 00 UTC 12 November the precipitation associated with the cyclone strongly increases in amplitude, which also induces the first increase in the amplitude of the low-level PV. At the same time the surface cyclone moves closer to the jet and the interaction between the lower and the upper levels begins. The upper-level jet already shows a significant wave shape and starts to split (not shown). The precipitation becomes much stronger and affects a continuously growing region. Between 06 and 18 UTC on 12 November the cyclone undergoes an extremly rapid intensification phase. It crosses the axis of the upper-level jet and finds itself at 154°E, 39°N in an optimal position between the two parts of a split jet. The central SLP decreases from about 990 to 960 hPa in only 12 hours. Subsequently the cyclone starts its slow decaying phase. It moves very slowly towards the north and remains connected to the upper level PV anomaly.

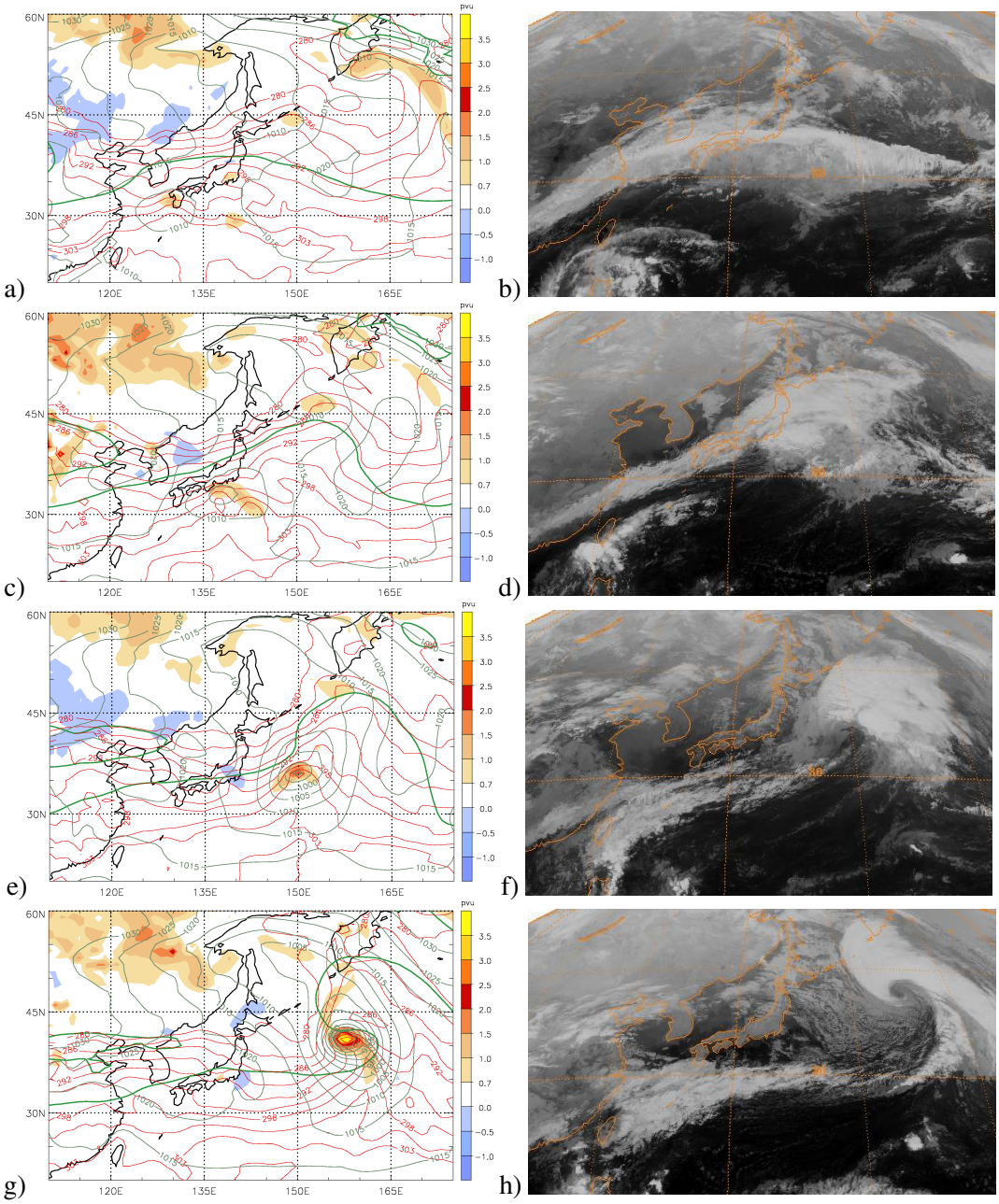

Figure 5.2: Development of the North Pacific cyclone at (a) 06 UTC 11 November, (b) 03 UTC 11 November (the satellite picture at 06 UTC 11 November was not available), (c,d) 18 UTC 11 November, (e,f) 06 UTC 12 November, and (g,h) 18 UTC 12 November 2005. Left: PV, vertically averaged between 975 and 800 hPa (in pvu, colours), SLP (grey lines, contour interval 5 hPa), 2-pvu isoline at 250 hPa (green bold line), and potential temperature at 900 hPa (thin red lines, contour interval 3 K). Right: IR satellite pictures from GOES west.

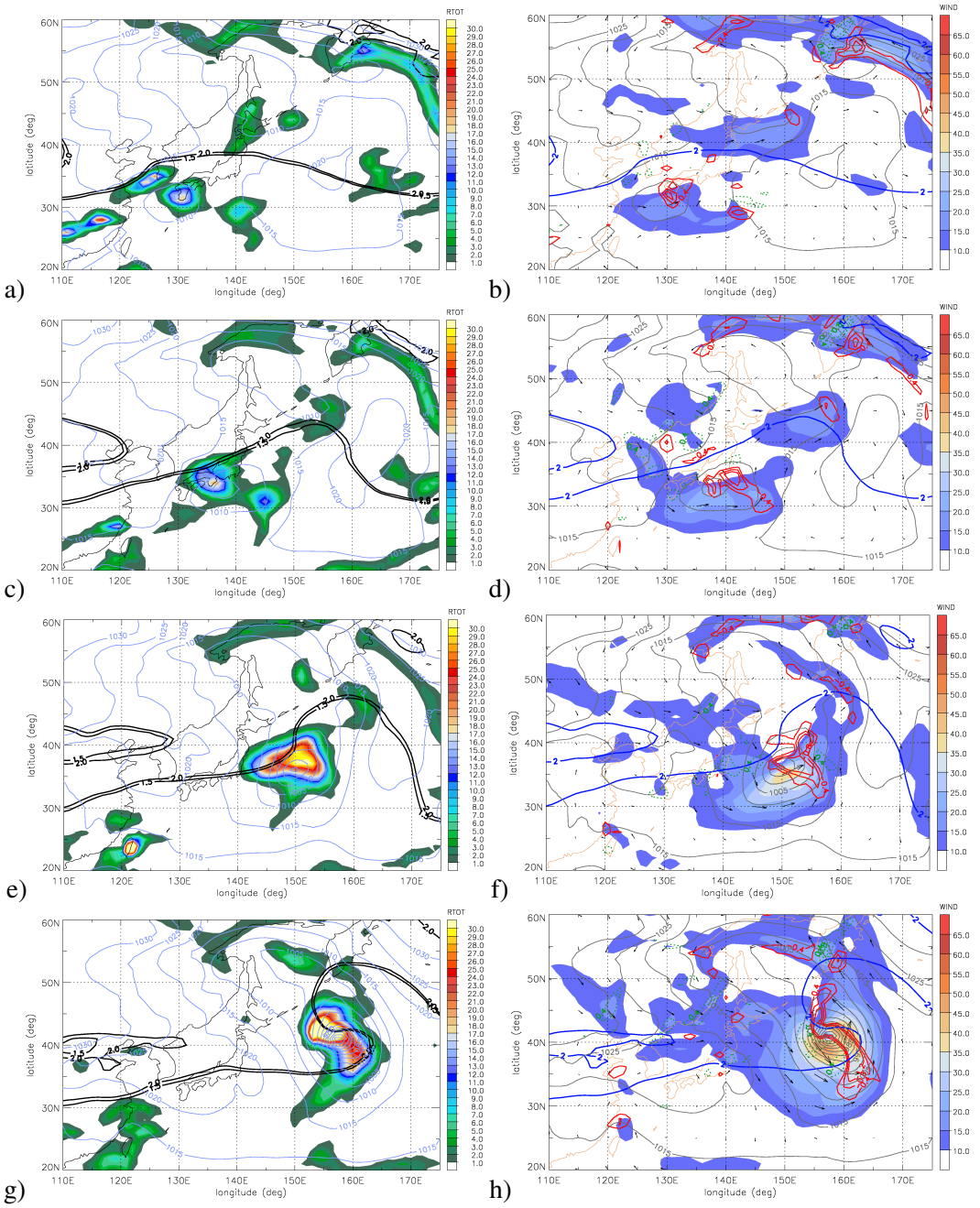

Figure 5.3: Development of the North Pacific cyclone at (a,b) 06 UTC 11 November, (c,d) 18 UTC 11 November, (e,f) 06 UTC 12 November, and (g,h) 18 UTC 12 November 2005. Left: Total precipitation (colours, in mm/6 h), SLP (light blue lines, contour interval 5 hPa), 1.5 and 2 pvu isolines at 250 hPa (black bold line). Right: Horizontal wind speed (colors, in $\mathrm{m\,s^{-1}}$) and vectors at 850 hPa, SLP (grey lines, contour interval 5 hPa), 2-pvu isoline at 250 hPa (blue bold line), and vertical velocity (contour interval $0.4\,\mathrm{Pa\,s^{-1}}$, red solid line negative values, green dotted line positive values.

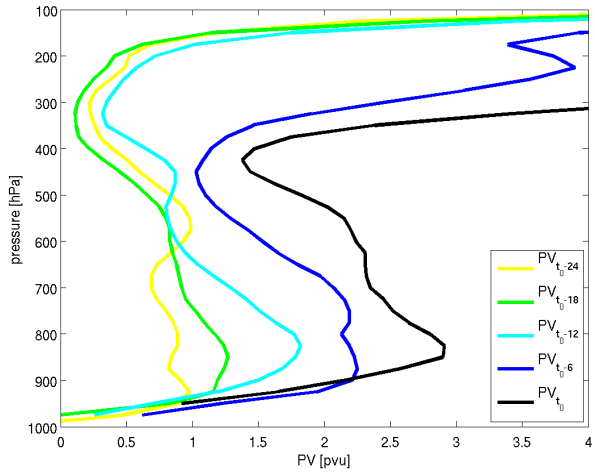

Figure 5.4: Temporal evolution of the vertical PV profile in the centre of the cyclone from 18 UTC 11 November and 18 UTC 12 November. Colours represent the time at which the profile was calculated (t_0 refers to 18 UTC 12 November, i.e., the time of minimum SLP).

5.2.3 Vertical PV profile

Next we consider the temporal evolution of the vertical PV profile in the centre of the cyclone (calculated with the same procedure as in Chapter 3). Figure 5.4 shows the profile evolution during the 24 hours of the strongest intensification, between 18 UTC 11 November and 18 UTC 12 November and reveals dramatic structural changes associated with the explosive intensification. One day before the cyclone's maximum intensity averaged PV values in a circle around the cyclone centre were between 0.7 and 1 pvu. During the next 12 hours especially low-level PV values intensified strongly. After the onset of the interaction with the upper levels we can also see the rapid lowering of the tropopause and further strong increase of the low-level PV.

5.2.4 The role of the WCB

The development of the cyclone was accompanied by strongly rising moist air masses. This cross-isentropically ascending air was responsible for building a pronounced upper-level ridge to the north of the cyclone and therefore enabled the interaction of the surface cyclone with the upper-level PV trough. Using LAGRANTO, we were able to identify coherent air streams in the vicinity of the cyclone that started at low levels and ascended to the upper troposphere where they significantly influenced the upper-level flow. We started 2-day forward trajectories in a box between 120-170°E, 15-40°N and 1000 and 800 hPa and selected those which rose more than 600 hPa. Trajectory ensembles with such a strong ascent can be referred to as warm conveyor belts (Wernli and Davies 1997). In Fig. 5.5

one of these air streams are presented, which was launched at 18 UTC 10 November.

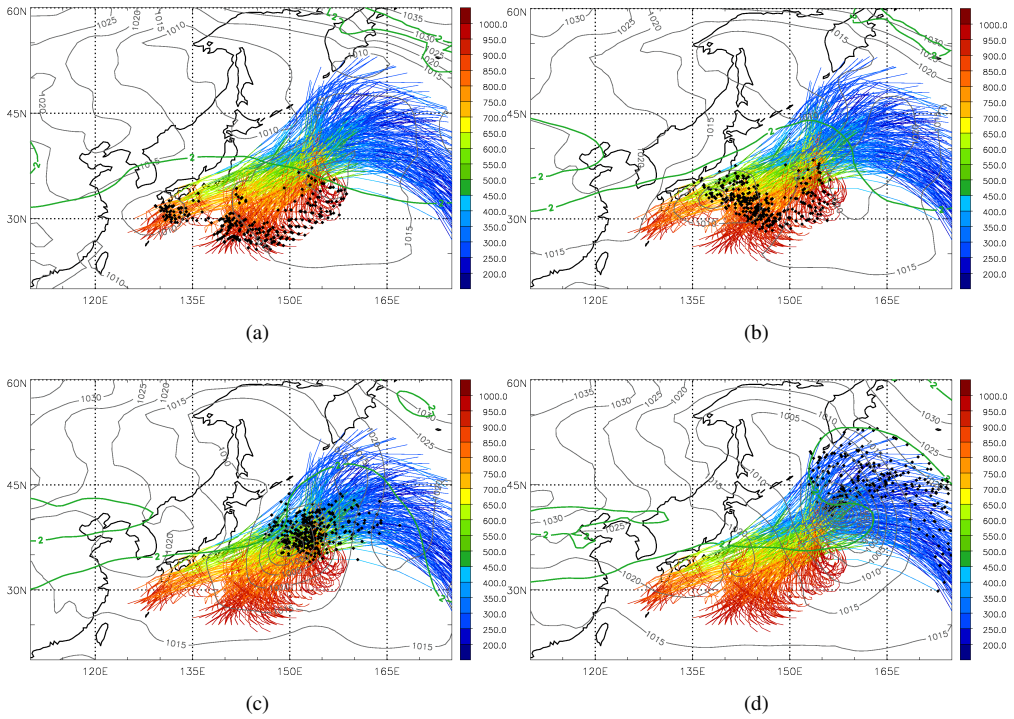

Figure 5.5: Warm conveyor belt trajectories in the vicinity of the cyclone started at 18 UTC 10 November. Black dots denote the trajectory positions at (a) 06 UTC 11 November, (b) 18 UTC 11 November, (c) 06 UTC 12 November, and (d) 18 UTC 12 November. SLP contours (grey lines) and the 2-pvu isoline on 250 hPa (green line) are shown at the same times. The trajectories are colored with pressure (in hPa).

All the identified WCB trajectories started their course under the influence of an anticyclone to the east of the cyclogenesis region (Fig. 5.5a,b). As the cyclone appears, its low level circulation advects the air towards the baroclinic zone where it is lifted (Fig. 5.5c,d) and where new PV needed for the propagation of the DRW is diabatically produced. This air is then further lifted to the upper troposphere. During its ascent it loses its high PV values and arrives near the jet with low PV values. Some of the trajectories ascend into the growing upper-level ridge, providing evidence for the diabatic influence on the upper-level ridge amplification (e.g., Grams et al. 2011). On average, the trajectories rose from approximately 950 hPa to 270 hPa and thereby overcame a height difference of 670 hPa. All trajectories started in the boundary layer with very low PV values (lower than 0.3 pvu). During the strongest lifting they underwent large variations of PV, reaching up to 2 pvu, until they finally arrived at the tropopause levels with average values of about 0.5 pvu.

5.2.5 Moisture source regions

Using the same technique as in Chapter 4 we calculated the moisture uptake regions that are important for the diabatic low-level PV production in this cyclone. We looked at PV in the cyclone centre at 18 UTC 11 November, and 06 and 18 UTC 12 November and diagnosed the associated moisture sources (see Fig. 5.6). 18 hours after genesis, the cyclone is still weak and relatively small. Moisture sources for PV in the cyclone centre at this time (Fig. 5.6a) are confined more or less to the direct vicinity of the cyclone. As the cyclone becomes stronger, the low-level PV anomaly intensifies (cf. Fig. 5.4), the cyclone can collect more moist air, and vertical motions leading to diabatic PV production are stronger. Therefore moisture uptake regions are larger in the later stages of the development (Figs. 5.6b,c). For this case, moisture sources are located on both sides of the cyclone track.

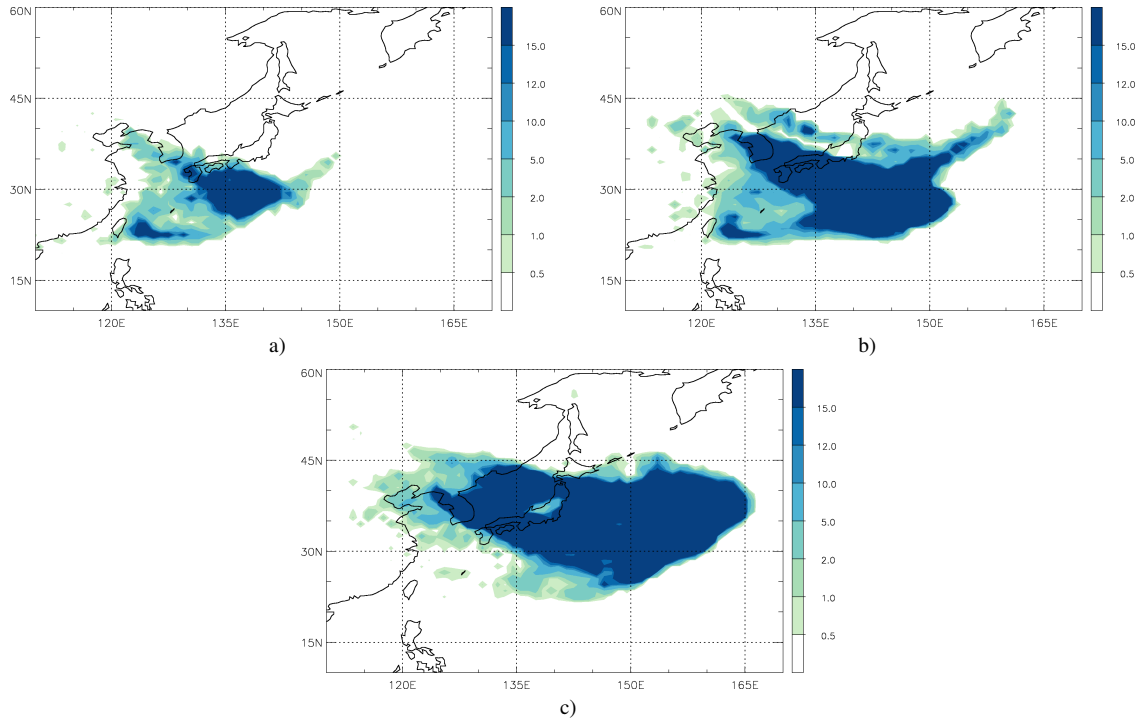

Figure 5.6: Moisture uptake regions that contributed to the production of PV in the cyclone centre at (a) 18 UTC 11 November, (b) 06 UTC 12 November, and (c) 18 UTC 12 November. The unit is g/kg per 10000 m^2.

5.3 COSMO model setup and control simulation

5.3.1 Model setup

The cyclone started its life cycle to the west of Japan and decayed south of Kamchatka. Therefore, the simulation area has been chosen over the western North Pacific as seen in Fig. 5.7. It contains 440×270 horizontal grid points with a horizontal spacing of 28 km, and 40 vertical levels. As the initial and boundary data 6-hourly ECMWF reanalyses were used. The cyclone was not yet present in the initial data. It developed approximately 6 hours after the start of the simulation at 00 UTC 11 November.

On the basis of the moisture source diagnostics three regions for moisture depletion sensitivity experiments were selected (see section 5.4). Modifications in the red box (Fig. 5.7) should influence the cyclone in its early stage (cf. Fig. 5.6a), those in the green box during the propagation (cf. Fig. 5.6b) and those in the blue box during the interaction with the upper-level trough (cf. Fig. 5.6c). The dry layer in the boxes extends from the surface to 700 hPa.

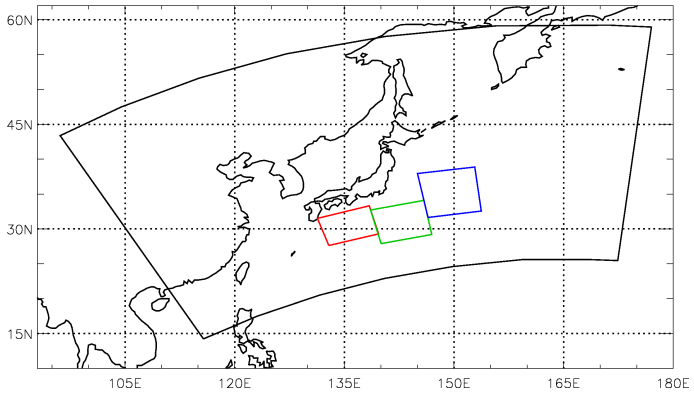

Figure 5.7: Model area (black) and boxes in which specific humidity was modified in the sensitivity experiments (see text for details). The experiments will be referred to as the red, green, and blue experiment, respectively.

5.3.2 The COSMO control run

In this subsection we compare the control run of the COSMO model to the reanalyses. Several runs with different starting times were performed. The simulations started up to 6 hours prior to cyclogenesis (i.e., started at 18 UTC 10 November, 00 and 06 UTC 11 November) represented the cyclone very well. Simulations with a longer lead time did not capture the cyclone evolution accurately enough. In the end, the run started at 18 UTC 10 November was chosen as the control simulation in order to ensure that the model produces the cyclone itself instead of getting it via the initial conditions.

The cyclone in the control run appears at 01 UTC 11 November at 127.5°E, 31°N. As in the reanalyses it is created at the western flank of an anticyclone, which drives air at low levels towards the baroclinic zone. The tropical cyclone to the south is not included in the simulation area but its flow field is captured via the boundary conditions. As for the reanalyses there is a strong jet at upper levels, which is perfectly aligned with the 2-pvu contour at 250 hPa. In the early phase, PV values in the lower troposphere are weaker than in ERA-Interim. Small-scale structures are typically much finer in COSMO output than in the reanalysis, due to the higher resolution, and PV anomalies are more concentrated.

At 06 UTC 11 November the cyclone reaches the southernmost Japanese island Kyushu (Fig. 5.8a) and moves eastward over it. On the east side of the island a small but strong PV anomaly is formed in the cyclone centre which is well seen in Fig. 5.8b. Vertically averaged low-level values are higher than 3.5 pvu. The whole low-level PV anomaly is much smaller than the one seen in the reanalysis but the values are much more pronounced. It's shape is more elongated compared to the almost circular structure in the reanalysis data at the same time. Air is lifted at the front side of the cyclone in front of the PV maximum. As the cyclone's development proceeds, its low-level PV structure is getting more and more elongated.

At 18 UTC 11 November another low-level positive PV anomaly can be seen approaching the cyclone from the southeast (Fig. 5.8b). In the reanalysis, this anomaly merges 6 hours later with the cyclone's PV anomaly and the cyclone moves rapidly in this time period. In contrast, the two PV anomalies in the control run do not merge until the cyclone is fully developed and the southern anomaly gets incorporated into the warm front. Therefore the cyclone track in the control run is slightly further north and it therefore can start interacting with the upper-level jet earlier.

The structure of the upper-level PV field is not as smooth as in the reanalysis data (see the 2 pvu lines at different levels in Fig. 5.8). Due to the higher resolution of the COSMO simulation we can see many small-scale features, especially in the region of the upper-level ridge. These PV blobs along the 2-pvu tropopause might be a consequence of air rising in the WCB to the tropopause level and interacting with the PV structure there.

The interaction of the cyclone with the jet starts early on 12 November. The jet splits completely at 06 UTC 12 November and at that time the cyclone is already crossing the jet axis (Fig. 5.8g). Six hours later the cyclone is located between the two jets. In the COSMO simulation the cyclone experiences the strongest deepening at the same time as the cyclone in the reanalyses, but its deepening phase lasts longer. After the cyclone becomes fully aligned with the upper-level high PV body (Figs. 5.8d,h) it slowly deepens further until it reaches the minimum SLP at 09 UTC 13 November. However, the rapid intensification phase before 18 UTC 12 November at the attained central SLP value of 961 hPa at this time corresponds very well to the intensification of the cyclone in the reanalysis (958 hPa).

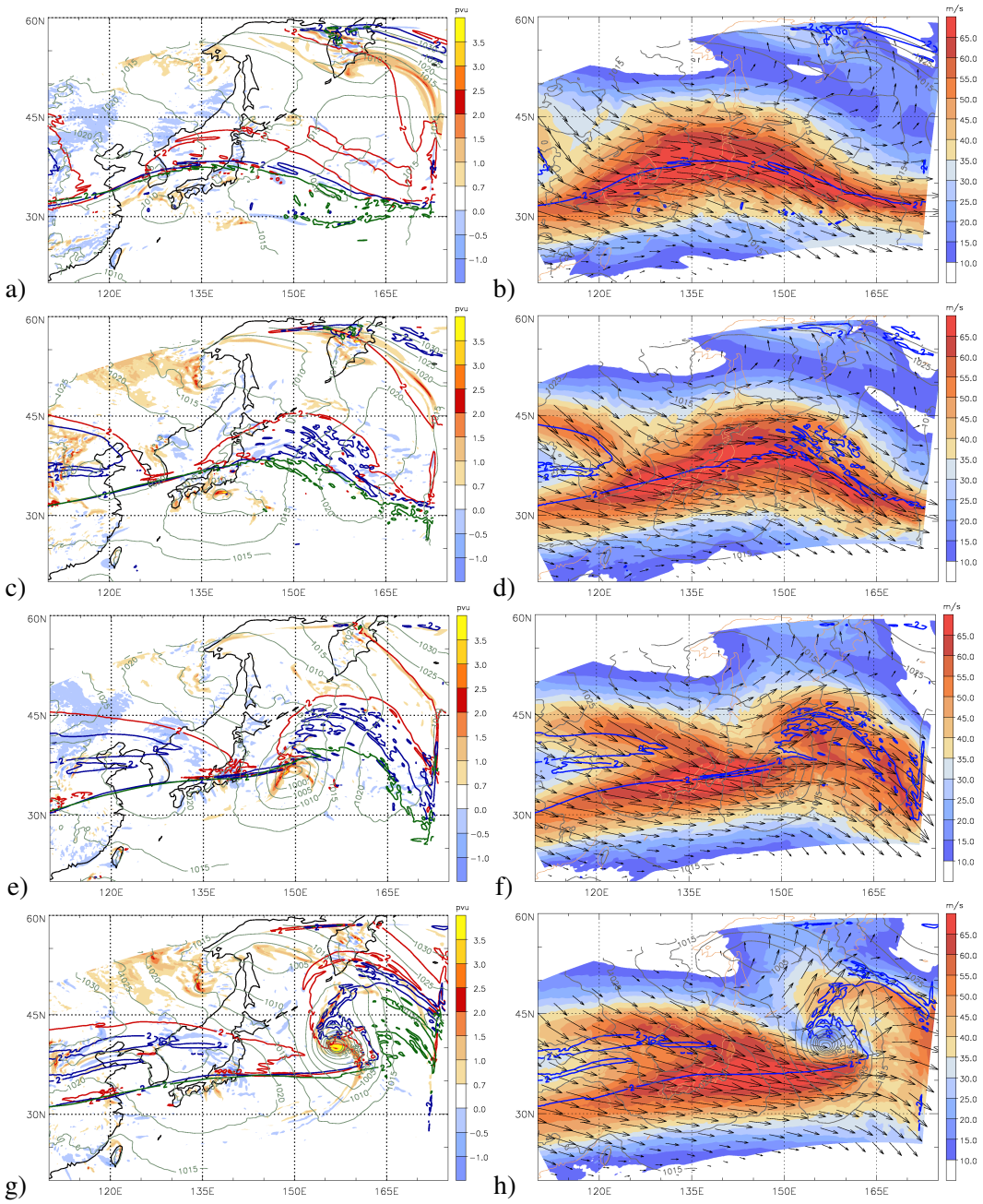

Figure 5.8: Development of the cyclone in the control simulation at (a,b) 06 UTC 11 November, (c,d) 18 UTC 11 November, (e,f) 06 UTC 12 November, and (g,h) 18 UTC 12 November. Left: PV averaged between 975 and 800 hPa (colours, in pvu), SLP (grey lines, contour interval 5 hPa), 2-pvu isoline at 300, 250 and 200 hPa (red, blue and green bold line, respectively). Right: Horizontal wind speed (colors) and vectors at 250 hPa, SLP (grey lines, contour interval 5 hPa), and 2-pvu contour on 250 hPa (blue line).

5.4 Cyclone development in experiments with the COSMO model

In this section, the COSMO sensitivity experiments will be presented. These experiments have been set up in order to investigate the influence of low-tropospheric moisture from different regions on the cyclone development. Previous case studies of DRWs and rapidly deepening cyclones emphasized the crucial role of moisture in the development of these features. The special aspects of this work are (i) to test the sensitivity of a rapidly deepening cyclone to moisture modifications at different stages of its development, and (ii) to determine the moisture modification regions with a moisture uptake diagnostic (see section 5.2.5).

First, as a reference, a completely dry simulation will be presented followed by the experiments with dry boxes as shown previously in Fig. 5.7.

5.4.1 Dry simulation

For the dry simulation moisture was completely eliminated in the entire atmosphere in the initial and boundary data. Furthermore, evaporation from the surface was turned off during the model integration in order to keep the atmosphere dry.

Without moisture, PV in the lower troposphere cannot be produced by moist diabatic processes, therefore one of most important mechanisms to sustain a DRW and rapidly intensify a cyclone is missing in this simulation. We therefore expect the development of a much weaker cyclone. The simulation will show to what extent "dry dynamics" alone would be able to produce this cyclone and thereby quantify the overall role of moist processes for this special case.

Figure 5.9 shows the evolution of the dry experiment. As expected, no condensational PV production takes place at low levels (Fig. 5.9a,b,c). The low-level PV that we see in the figures is mostly confined to continents and most likely produced by frictional processes. In the first hours of the simulation the initially present, diabatically produced low-level PV over the ocean decays relatively fast due to boundary layer turbulence and in the absence of a diabatic PV source. A very weak signal in SLP appears at 10 UTC 11 November, moves to the east and merges with the SLP minimum associated with the PV anomaly that approaches the cyclone from the south (cf. Fig. 5.9b and discussion of the control experiment). The cyclone's minimum SLP values remain higher than 1010 hPa at all times. The cyclone never reaches the jet nor does it intensify. It decays at 06 UTC 12 November (Fig. 5.9c), i.e., at the time when the cyclone in the control run starts to intensify.

The development at the tropopause is much weaker than in the control run. The 2-pvu isolines at different levels are fairly straight compared to the control run, which clearly emphasizes the importance of diabatic processes for the formation of the upper-level ridge downstream of the evolving cyclone in the control simulation. Also, in the dry experiment the upper-level jet did not split. In the first hours of the simulation its structure was very

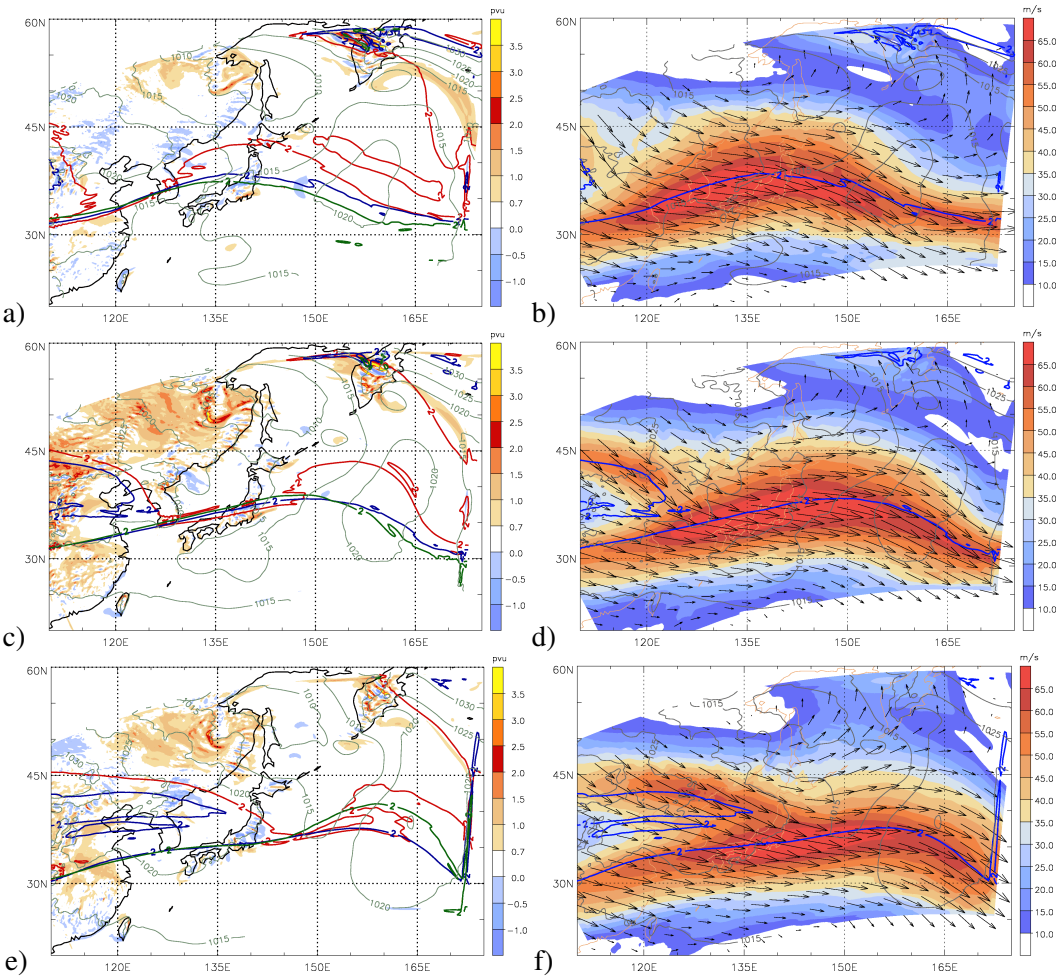

Figure 5.9: Development of the cyclone in the dry simulation at (a,b) 06 UTC 11 November, (c,d) 18 UTC 11 November and (e,f) 06 UTC 12 November. Left: PV averaged between 975 and 800 hPa (in pvu, colours), SLP (grey lines, contour interval 5 hPa), and the 2-pvu isoline at 200, 250, and 300 hPa (green, blue and red lines, respectively). Right: Horizontal wind speed (colors) and vectors at 250 hPa, SLP contours (grey, every 5 hPa), and 2-pvu contour on 250 hPa (blue line).

similar to the control run (cf. Figs. 5.9d and 5.8e). At the time when the jet splits in the control run, i.e. at 06 UTC 12 November, it is about 10° longer in the zonal direction in the dry run (Fig. 5.9e). The jet in the control simulation does not reach that far to the east due to the effects of the rotation around the cyclone located at around 150°E (Fig. 5.8g).

This simulation definitely confirms the high importance of moisture and latent heating for the development of this particular cyclone. However, this type of completely dry simulations is rather "rude" and modifies the atmospheric flow not only in the vicinity of the system of interest. Therefore a more specific technique is to eliminate moisture (and the associated latent heating) only in confined, pre-specified boxes. The results from a series

of such experiments are described in the following.

5.4.2 Red box experiment

In this experiment the dry box was placed directly south of Japan, approximately 7 degrees east of the cyclone's genesis region (see Fig. 5.10a). According to the moisture source diagnostic (Fig. 5.6a), low-level moisture in this region is essential for the diabatically produced PV in the cyclone centre at 18 UTC 11 November which was produced during the 24 hours prior to this time.

In this red box experiment, cyclogenesis occurs at 01 UTC 11 November at 126°E, 30°N. In the first 6 hours the cyclone remains situated almost at the same position and deepens by 2 hPa, similar to the control run. Then, after crossing the southern Japanese island Kyushu, the low-level PV anomaly intensifies in the control experiment. In contrast, this PV anomaly is missing in the red box experiment due to suppressed moisture and latent heating in the box (Fig. 5.10a). As a consequence, the cyclone dies 14 hours after its genesis at the western boundary of the box.

The second PV anomaly near 145°E at 18 UTC 11 November, which in the control run approaches our main cyclone of interest from the south, is also present in the red box experiment (Fig. 5.10a). It forms just south-east of the box at 00 UTC 11 November (not shown here) and appears to be stronger than in the control run. It moves undisturbed towards the northeast. Since the cyclone that it should merge with is missing, this approaching PV anomaly acts as the precursor for a new cyclone genesis at 13 UTC 11 November. At 18 UTC 11 November it is located 5 degrees to the east of the original cyclone (cf. Figs. 5.8b and 5.10a) and has a central SLP of 1009 hPa (compared to 1002 hPa in the control run).

During the next 6 hours the cyclone moves eastward and intensifies. At 06 UTC 12 November it is located to the southeast of the trough and starts crossing the jet (Figs. 5.10b,e). The ridge downstream of the cyclone is weaker than in the control run (compare Figs. 5.8c and 5.10b; note in particular the differences on 250 hPa) and the jet does not split yet. The cyclone has crossed the jet axis at 18 UTC 12 November and is located between the two upper-level jets. Its central SLP has decreased to 981 hPa. In the control experiment the jet crossing occurs 6 hours earlier and 5 degrees further west. Until the jet crossing, the upper-level ridge in the red box experiment can be seen only at 300 hPa. Thereafter, the ridge extends vertically and appears also at 250 hPa (Fig. 5.10c).

At the same time a weak secondary SLP minimum can be seen north of the main cyclone. This cyclone is a result of earlier interaction of lifting air with the approaching trough. The beginning of its development can be seen in Fig. 5.10b where the 1010 hPa contour is elongated towards the north containing a very weak second SLP minimum. Moist air is advected by the primary cyclone towards a baroclinic zone extending from the Korean Peninsula over Japan towards the Kamchatka Peninsula (not shown here). The arriving trough impinges on this lifting air before the interaction with the primary cyclone starts. It gives the secondary cyclone the opportunity to develop independently. This

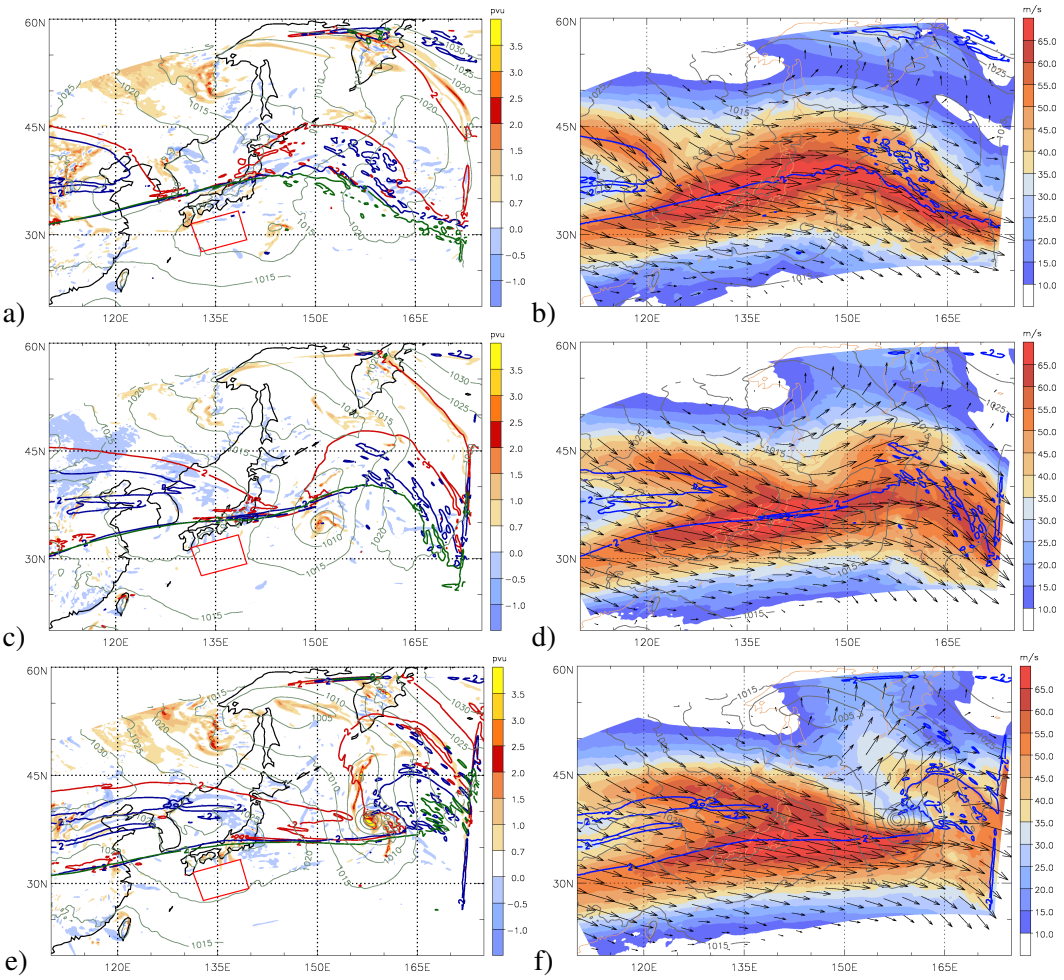

Figure 5.10: Development of the cyclone in the simulation with the red dry box at (a,b) 18 UTC 11 November, (c,d) 06 UTC 12 November, and (e,f) 18 UTC 12 November. Left: PV averaged between 975 and 800 hPa (in pvu, colours), SLP (grey lines, contour interval 5 hPa), and the 2-pvu isoline at 200, 250, and 300 hPa (green, blue and red lines, respectively). Right: Horizontal wind speed (colors) and vectors at 250 hPa, SLP contours (grey, every 5 hPa), and 2-pvu contour on 250 hPa (blue line).

feature was not seen in the reanalyses nor in the control simulation. There, the primary cyclone and the trough were in an optimal position so the interaction could start earlier. The lifting air at the baroclinic zone contributed to the rapid intensification. Due to lacking or postponed interaction between the surface cyclone and the trough this secondary cyclone develops in all experiments with a dry box.

To shortly summarize, the original cyclone dies in this experiment due to lack of moisture in the red box. The PV anomaly approaching from the south still produces a cyclone, which crosses the jet axis slightly weaker, intensifies less and produces weaker

downstream ridge. Additionally, a secondary cyclone to the north of the primary cyclone develops.

5.4.3 Green box experiment

Compared to the red box experiment, the box is now located further downstream at a position reached by the cyclone at approximately 16 UTC 11 November. Until this time the development of the cyclone and the upper-level ridge are very similar to the control run (with a minor difference of its central SLP by 2 hPa). In this experiment the dry box stops the propagation of the PV anomaly coming from the south, which therefore never reaches the cyclone (Fig. 5.11a).

During the passage of the dry box the low-level PV almost completely disappears but weak signals in the SLP field and low-level circulation remain, which are associated with a surface warm anomaly. Shortly before the interaction with the upper-level PV anomaly the cyclone is very weak (1005 hPa at 06 UTC 12 November, see Fig. 5.11b). Compared to the control experiment, the trough is located a few degrees further east such that the cyclone is not in an optimal position to favorably interact with the upper-level anomaly. The main reason for the too rapid propagation of the upper-level trough in this experiment is the strongly reduced PV destruction associated with the outflow of the approaching cyclone.

The cyclone crosses the jet axis without strongly intensifying and much later and further downstream (cf. cyclone location at 158°E, 37°N in Fig. 5.11f) than in previous experiments. The crossing does not occur in the jet exit region since the jet extends further to the east compared to the control run. This can be seen in Figs. 5.11c,f, note in particular the green and the blue contours that are very close and rather straight. After the jet crossing the cyclone intensifies slightly and reaches its minimum SLP of 992 hPa. The downstream ridge is even a bit weaker than in the red box experiment.

However, the secondary cyclone (at 156°E, 44°N in Figs. 5.11c,f) undergoes the strongest intensification in this experiment. At 18 UTC 12 November it is 8 hPa deeper than the primary cyclone and later reaches its minimum SLP of 986 hPa.

In summary, locating the dry box further downstream kills the PV anomaly approaching from the south and the DRW. Only a very weak cyclonic remnant crosses the upper-level jet axis in a position that is not most favorable for a strong vertical coupling. Consequently the primary cyclone remains weak and so does the upper-level downstream ridge. It also remains quite far south and a new cyclone forms beneath the trough to the north of the jet axis, which is the strongest in this experiment.

5.4.4 Blue box experiment

In the blue experiment the dry box is located even further downstream. The moisture from this box should primarily influence the cyclone during its intensification stage.

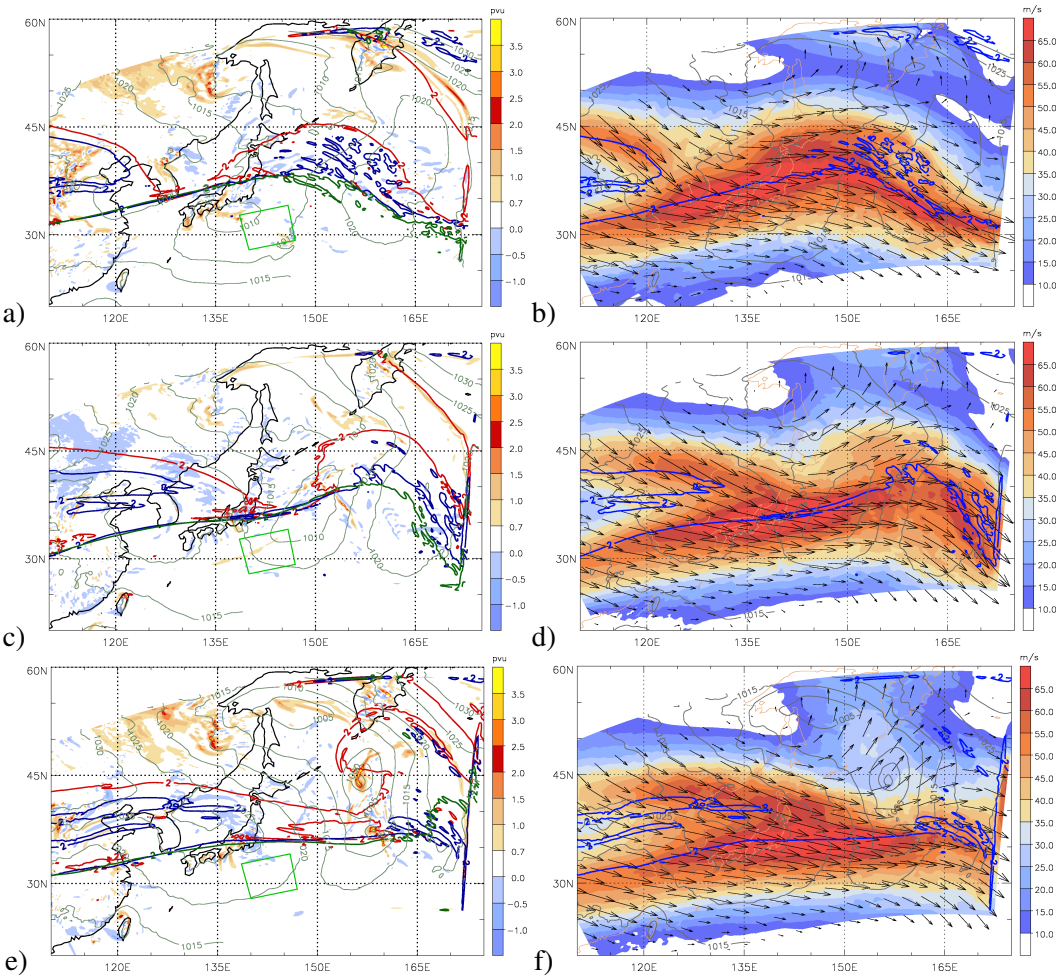

Figure 5.11: Development of the cyclone in the simulation with the green dry box at (a,b) 18 UTC 11 November, (c,d) 06 UTC 12 November, and (e,f) 18 UTC 12 November. Left: PV averaged between 975 and 800 hPa (in pvu, colours), SLP (grey lines, contour interval 5 hPa), and the 2-pvu isoline at 200, 250, and 300 hPa (green, blue and red lines, respectively). Right: Horizontal wind speed (colors) and vectors at 250 hPa, SLP contours (grey, every 5 hPa), and 2-pvu contour on 250 hPa (blue line).

The cyclone reaches the box at 06 UTC 12 November, i.e., at the time when the strongest intensification starts in the control experiment (Fig. 5.12b). Until this time the evolution is very similar to the control experiment. In the blue box experiment, the PV anomaly associated with the approaching cyclone does not decay completely as it enters the box but it drifts from the centre of the box to its southern boundary. At that time, the cyclone's minimum SLP is approximately 5 hPa higher than in the control experiment.

In this experiment a rather strong upper-level ridge forms, in agreement with the undisturbed diabatic activity of the cyclone in its first phase. However, due to distortion by the

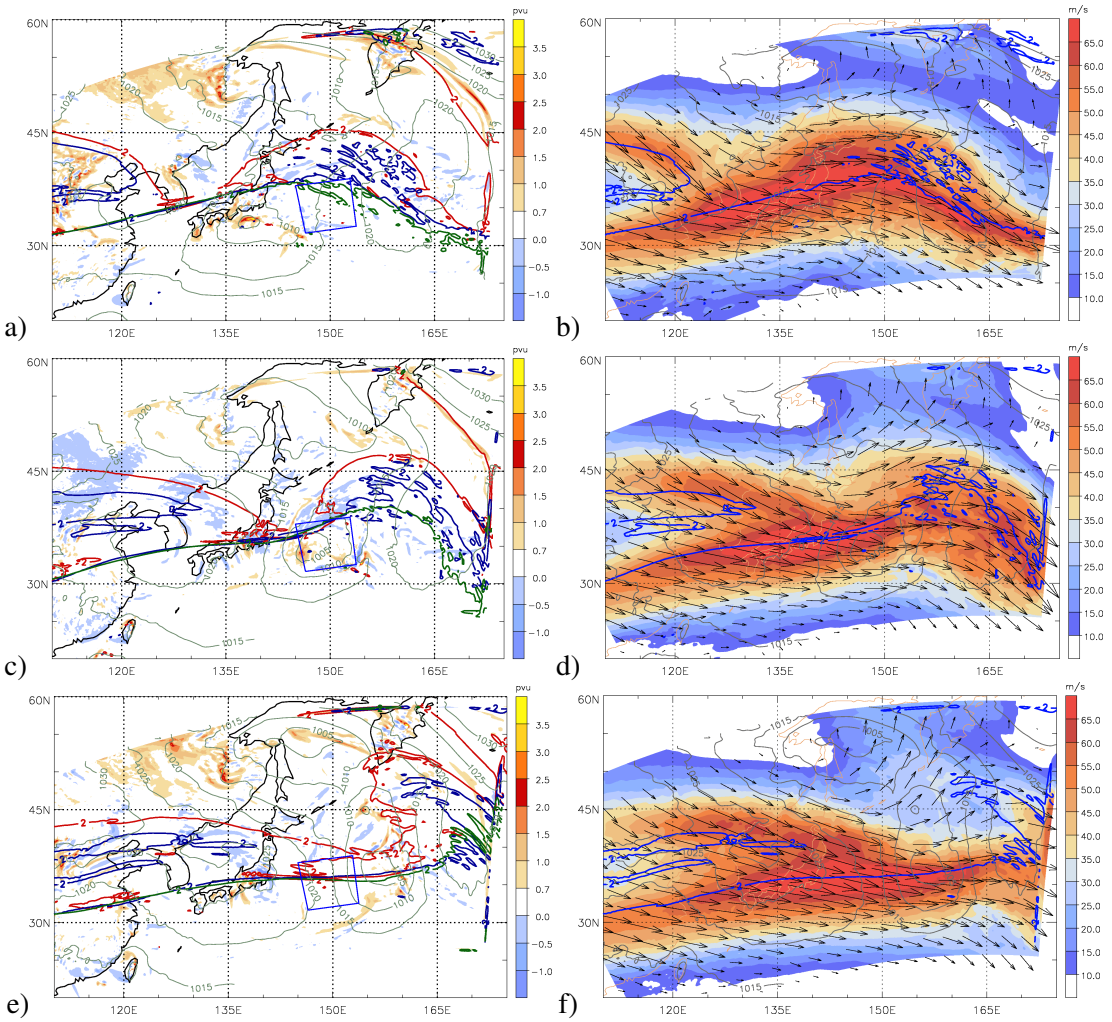

Figure 5.12: Development of the cyclone in the simulation with the blue dry box at (a,b) 18 UTC 11 November, (c,d) 06 UTC 12 November, and (e,f) 18 UTC 12 November. Left: PV averaged between 975 and 800 hPa (in pvu, colours), SLP (grey lines, contour interval 5 hPa), and the 2-pvu isoline at 200, 250, and 300 hPa (green, blue and red lines, respectively). Right: Horizontal wind speed (colors) and vectors at 250 hPa and SLP contours (grey, every 5 hPa), and 2-pvu contour on 250 hPa (blue line).

blue box, the cyclone is too slow and too far south in the crucial phase prior to intensification. The approaching upper-level trough is a bit further downstream than in the control run, but still approximately 5 degrees further west than in the green box experiment. The jet splitting starts at 08 UTC 12 November in the green box run, but the retarded cyclone does not allow for a most favorable interaction with upper levels. In this experiment, the originally fully developed cyclone has contributed to the formation of the pronounced upper-level ridge (and trough), but was then slowed down and missed the optimal location

for the crossing the jet axis. As a consequence, the cyclone only deepened to 1000 hPa at 18 UTC 12 November (Fig. 5.12c). However, it passed the dry box with a weak but a clear signal in SLP. 6 hours later it crossed the jet and low-level circulation strenghtened. By the end of the simulation the cylone deepened to 978 hPa. The secondary cyclone develops also in this simulation. It remains very weak as the low level circulation advecting air towards the baroclinic zone was inhibited in the blue box.

The cyclone in this experiment affected the PV distribution at the tropopause in the early stage of its development contributing to the ridge formation. It was strongly weakened in the dry box, however it maintained the circulation at low levels. The deepening phase was delayed, but the cyclone reintensified after passing the box.

5.5 Comparison of cyclone tracks, SLP evolution, vertical PV profiles, and upper-level wave pattern

In order to synthesize the evolution of the cyclone in the various experiments (control, dry, and red, green and blue box experiments), we compare the identified cyclone tracks and the evolution of the cyclones central SLP and vertical PV profiles, respectively. In experiments with discontinuous tracks (e.g., in the red box experiment where the DRW decays in the box and a new cyclone forms downstream), both track segments will be considered.

5.5.1 Cyclone track and minimum SLP

Figure 5.13 shows the diagnosed cyclone tracks and the associated time evolution of central SLP. The line colours correspond to the colours of the boxes in the experiments. Primary cyclone segments are plotted with solid lines and secondary segments with dotted lines. The track of the cyclone from the dry experiment is not included here because the cyclone dies a couple of hours after the beginning of the simulation.

The tracks start almost identically and drift apart from the control track once the cyclones impinge on the dry box. The cyclone in the red box experiment first impinges on the dry box and ends there. At the same time a new cyclone is produced downstream of the box. At the beginning its position is 5 degrees south of the primary cyclone segments in the other simulations but it then advances in a more northward direction and eventually is located in almost the same region as the other cyclones (Fig. 5.13b). Approximately at 22 UTC 12 November the secondary cyclone that develops on the northern side of the jet is first identified as an independent cyclone by the tracking algorithm although it can be seen at separate times before.

Although the red box cyclone is the weakest at the beginning it intensifies much earlier than the cyclones in the other box experiments. The strongest intensification phase starts at approximately the same time as in the control experiment and it ends after the cyclone has crossed the jet axis, at 00 UTC 13 November, 6 hours after the cyclone in the control

run. The northern SLP minimum (as defined by the tracking program) appears at 22 UTC 12 November with a central SLP of 998.3 hPa. It forms at the northernmost position of all experiments. It weakens as it moves to the west of Kamchatka.

In the green box experiment, the cyclone follows the track of the control cyclone until 14 UTC 11 November. Four hours later it is located 3 degrees to the west of the control cyclone. It remains very weak as it passes the dry box. The intensification only sets in at 15 UTC 12 November when the cyclone starts crossing the jet axis. Its track is further south than the control cyclone since the simulation is lacking the correct evolution of the upper-level trough, which would advect it further north. The cyclone reaches a minimum SLP value of 992.4 hPa and then decays. This is the only simulation in which the northern cyclone becomes stronger than the main one further south. The northern cyclone forms beneath the eastern flank of the trough and deepens by 20 hPa before it settles.

The cyclone in the blue box experiment follows the control cyclone during the first 24 hours of its lifetime. In the box it is slowed down and weakens. At 06 UTC 12 November, when the control cyclone starts to intensify, the cyclone in the experiment is located approximately 200 km to the southwest of the control cyclone's position. With a central SLP of 1000.8 hPa it is 10 hPa weaker than the control cyclone. It crosses the jet axis only at 00 UTC 13 November, almost 10 degrees further to the east than the control cyclone. It then interacts with the upper-level trough and intensifies to a minimum SLP value of 978 hPa at the end of the simulation. In this experiment also the northern cyclone misses the optimal position for intensification to the east of the trough. It forms when the wave on the jet has already passed and the jet has become straight again.

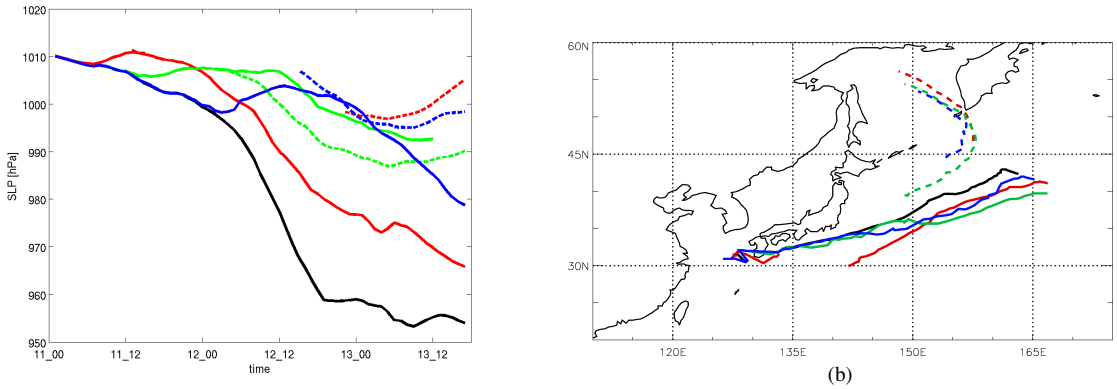

Figure 5.13: Temporal evolution of the cyclones' minimum SLP (a) and tracks (b) in the different COSMO simulations. Colours correspond to those in Fig. 5.7, the results for the control run are shown in black.

5.5.2 PV profile

The strong intensification of the cyclone in the ERA-Interim dataset was also seen in the evolution of the cyclone's vertical PV profile (Fig. 5.4). During the 24 hours of maximum intensification the horizontally averaged low-level PV values rose from 1 to 3 pvu. PV at upper levels started to increase more than 12 hours later. Here we consider the evolution of the vertical PV profiles in the dry box experiments, i.e., under modified moisture conditions. Again, the profile calculation in the dry run is omitted here, since the cyclone was not present.

The cyclones in the experiments intensify and reach their maximum intensity at different times. Therefore the vertical PV profiles were calculated in a time window of 27 hours between 03 UTC 12 November and 06 UTC 13 November. After the splitting of the cyclones we only consider and follow the southern track.

Large differences between the experiments and the control run can be seen in Fig. 5.14. As expected, the highest PV values are found in the centre of the control cyclone. At 09 UTC 12 November (cyan dotted line in Fig. 5.14a) the cyclone had already started to cross the jet axis and to interact with the upper-level trough. The PV values at upper levels (between 300 and 200 hPa) are the highest of all simulations at this time. Also the low-level PV values are already larger than 1 pvu in a deep vertical layer. The strongest intensification phase ended at 19 UTC 12 November when we see PV values larger than 3 pvu between 700 and 800 hPa (yellow and green line in Fig. 5.14a). Afterwards the tropospheric PV values decrease although the cyclone still slowly deepens.

The evolution of the profile in the red experiment lags behind the control run by 3-6 hours. The low-level PV values are similar at the beginning of the intensification. The PV production is less intense and the highest values are 2.2 pvu at 00 UTC 13 November at about 800 hPa (solid cyan line in Fig. 5.14b).

The cyclone in the green experiment has the lowest PV values in the centre at the beginning of the profile calculation (dotted lines in Fig. 5.14c). At that time the cyclone is located in the middle of the dry box. The cyclone leaves the box already at 06 UTC 12 November, but the deepening sets in only 6 hours later. Between 12 and 21 UTC 12 November we can see the lowering of the tropopause as the trough approaches and afterwards tho production od low-level PV follows.

The low-level PV values in the blue experiment (Fig. 5.14d) are larger than 1 pvu in the first three profiles and drop between 9 and 12 UTC 12 November, after the cyclone has entered the dry box. However, the values above 700 hPa (which is the upper boundary of the box) remain as before. This effect can also be seen in the green box experiment. Between 12 and 21 UTC 12 November the cyclone approaches and crosses the jet. We can see this process by the lowering of the tropopause. But the low-level PV only increases after 21 UTC. This cyclone exhibits the lowest overall PV values of all experiments in this time window. During its late intensification phase it again gains some low-level PV.

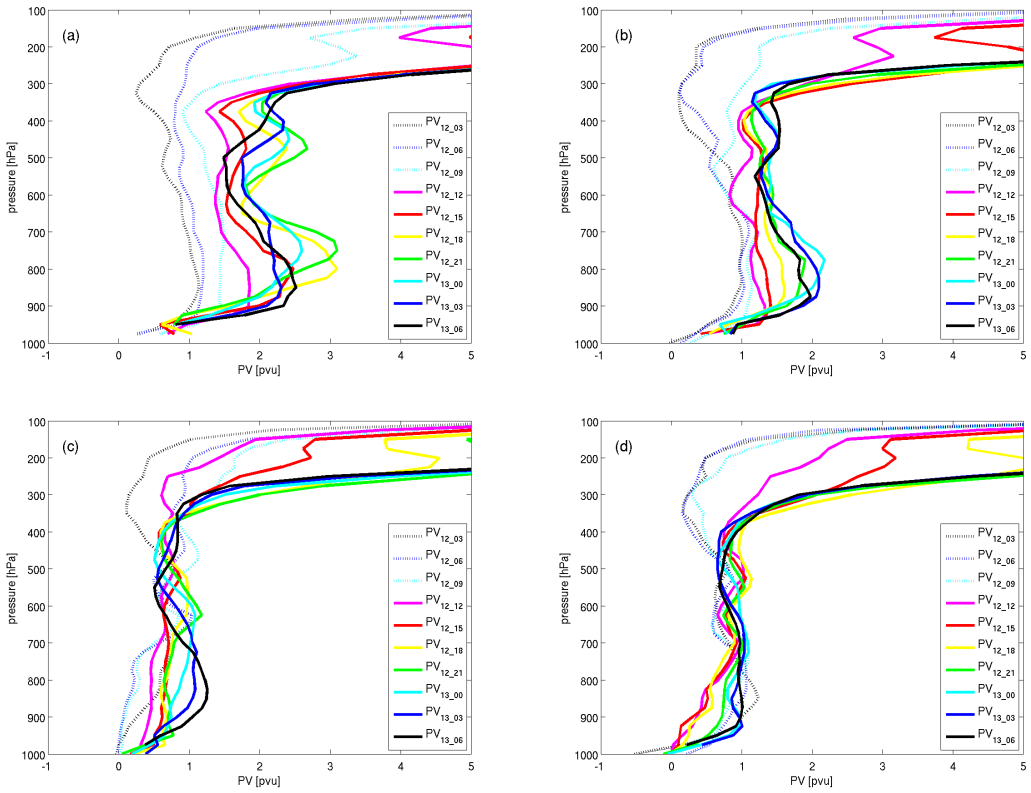

Figure 5.14: Evolution of vertical PV profiles in the centre of the cyclone from 03 UTC 12 November to 06 UTC 13 November. The colours correspond to different times (see legend). Panels are (a) for the control run, (b) the red box experiment, (c) the green box experiment, and (d) the blue box experiment.

5.5.3 Upper-level ridge and jet stream

The interaction of the initially shallow low-level cyclone with the upper-level trough triggered the strong intensification of the cyclone. However, it is important to note that the surface cyclone itself influenced the tropopause-level wave pattern before and during the intensification phase due to the cross-isentropic transport of WCB-like air masses to the upper levels. Here, changes of the upper-level PV distribution and the associated jet will be compared in the different experiments. The dry run is included here because the presence of the surface cyclone is not necessary for the analysis of the development at the upper levels.

In the first 12 hours of the cyclone life cycle, the 2-pvu contours look very similar in most experiments (not shown). Only the ridge in the dry experiment is already more than 5 degrees shorter at the rear side. This indicates that the ridge might be partially a consequence of diabatic processes in ascending air masses at the strong baroclinic zone,

which are not affected by the box experiments. After this time small deviations start to develop in the red experiment. At 18 UTC 11 November the ridge at 300 hPa is also missing the rear part north of the dry box (see Fig. 5.10a). There are less small-scale structures in the PV field at 250 hPa. This points to missing vertical motions in that region, which are probably caused by air lifted within a WCB. This difference is even more pronounced 6 hours later, at 00 UTC 12 November, but the pattern in the green and blue experiments is still almost the same (not shown). At this time the new cyclone in the red experiment has already formed and the cyclone in the green experiment has entered the dry box. Therefore, 6 hours later we see the same effects at the tropopause in the green run as earlier in the red experiment, i.e., the missing rear part of the ridge at 300 hPa and less structure at 250 hPa (Fig. 5.11b). The rear part of the ridge in the red experiment has formed again (Fig. 5.10b). At this time we can see a pronounced ridge also at 250 hPa in the control and blue box simulations (Figs. 5.8c and 5.12b), and less deep one in the red and green runs (Figs. 5.10b and 5.11b). The meridional extension of the ridge at 300 hPa in the dry experiment is approximately 10 degrees smaller at its maximum than in the other experiments (it does not reach as far north as in the other experiments). However, the 2-pvu contour at 200 hPa looks the same in all experiments, also in the dry run. We can therefore attribute the relatively weak wave pattern at 200 hPa to the dynamical processes that are not affected by moisture, and the much more pronounced trough-ridge couplet on 250 and 300 hPa to the influence of moist processes.

In Fig. 5.15 we compare the shape of the 2-pvu tropopause on 200, 250 and 300 hPa at 12 UTC 12 November. The ridge in the control run (Fig. 5.15a) has the largest horizontal and vertical extension. At 300 hPa (red line), the 2-pvu contour reaches farthest to the west compared to the other simulations and we also see significant disturbances at 200 hPa (green line). The amplitude of the ridge at 250 hPa in the red and green experiments is small (Figs. 5.15b,c). The ascent of air from low levels to the tropopause region was interrupted at the time that was important for the intensification of the trough. Actually, a weaker ridge did form in the green experiment, but it propagated downstream too quickly as it was not retarded by interaction with the cyclone. The ridge at 250 hPa in the red experiment forms a couple of hours later in parallel to the cyclone intensification. The ridge does not reach the same extent as in the control run, but it is still larger than in the other experiments. The WCB in the blue experiment (Fig. 5.15d) is fairly strong and produces a relatively high-level ridge. However, at this time it is already 10 degrees downstream of the surface cyclone center and does not start interacting with the weak surface cyclone. Also the ridge in the dry experiment is located further downstream and is the weakest of all (Fig. 5.15d).

Clearly the evolution of the tropopause structure goes along with the development of the upper-level jets. The formation of a strong ridge leads to a splitting of the jet and prepares an optimal environment for cyclone intensification. The jet splitting occurs in the control run, and the red and blue experiments. In the control and red run, we have also seen a strong cyclone deepening. In the blue experiment, however, the jet splitting as well as ridge building happened too early, at a time when the surface cyclone was still

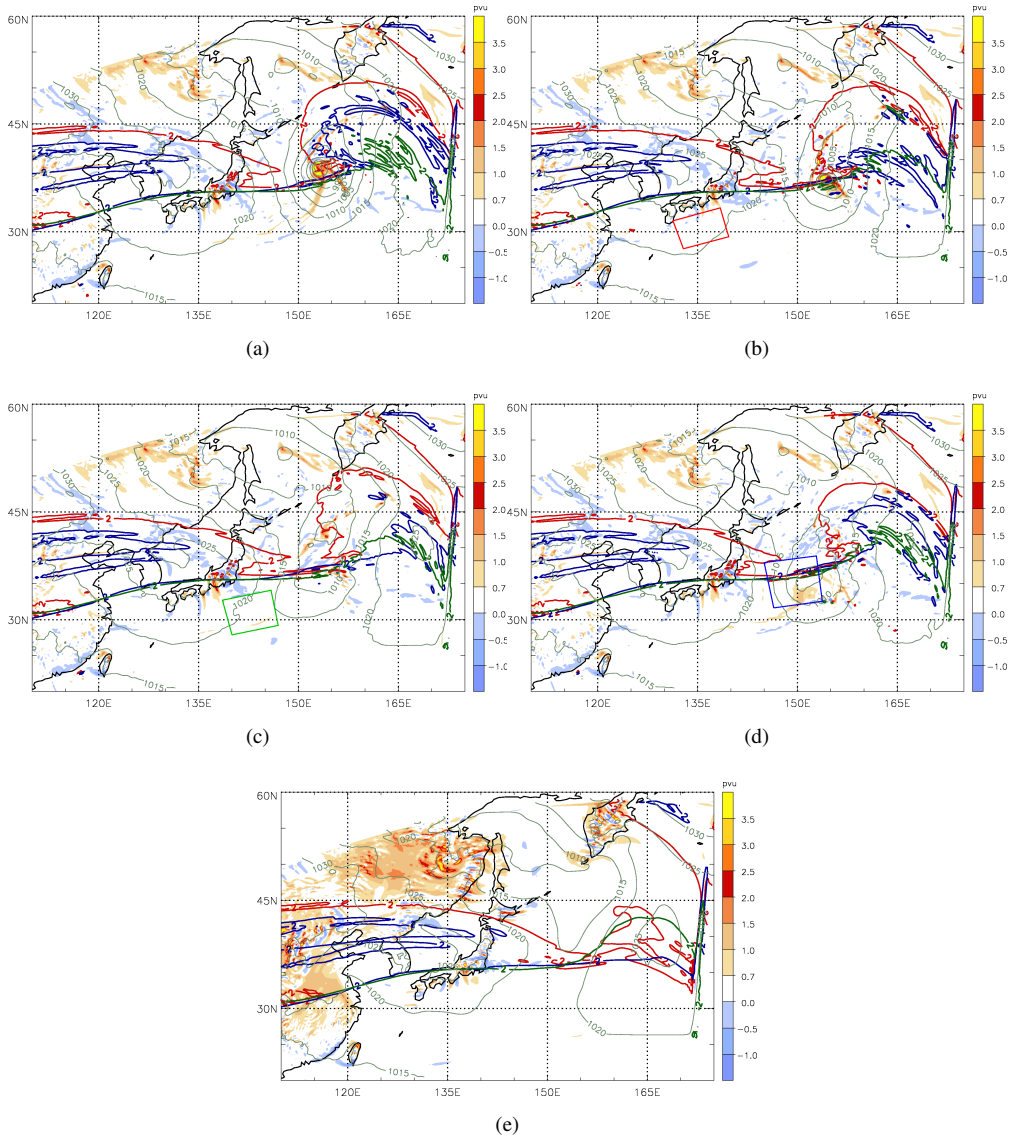

Figure 5.15: Comparison of the tropopause structure at 12 UTC 12 November for (a) the control run, (b) the dry run, and (c,d,e) the red, green, and blue box experiments, respectively. Bold lines show 2-pvu contours at 300 hPa (red), 250 hPa (blue), and 200 hPa (green). Grey contours denote SLP every 5 hPa, and low-level vertically averaged PV is shown in colours.

too weak. Later, when the interaction between the low-level cyclone and the upper-level wave started, the split part of the jet was already far downstream. In the green and dry experiments no jet splitting occurred. The diabatic modification of the upper-level PV structure was not strong enough to distort the jet.

5.6 Summary and discussion

In this Chapter a rapidly intensifying cyclone in the Pacific ocean was simulated. At the beginning of its life cycle it propagated as a DRW with steong low-level PV production and no influence from the upper levels. After approximately 24 hours the surface cyclone merged with another positive low-level PV anomaly approaching from the south and arrived in the vicinity of a tropopause jet. With the crossing of the jet the explosive intensification began and the cyclone deepened about 30 hPa in 12 hours.

Simulations with the COSMO model have been performed to investigate the influence of low-level humidity on the cyclone development in different stages. Moisture was completely eliminated in three different low-level boxes along the cyclone track. In addition, a control run and a traditional "dry run" have been made. In the latter, moisture was eliminated in the entire model domain. We compared the evolution of the cyclone in the different simulations and focused in particular on the track of the cyclone, its intensity, and its vertical PV profile.

The control simulation reproduced the cyclone development and intensification very well. Compared to the reanalysis data, the simulated cyclone had much finer structures and higher values of low-level vorticity.

Moisture elimination in a box passed by the cyclone in its early phase as a DRW leeds to its destruction. A new cyclone occurred downstream of the box due to the advection of a low-level positive PV anomaly from the south. This cyclone took a similar track as the original cyclone and became almost as intense as in the control run. The ridge in front of the cyclone was not very deep at the beginning of the intensification phase, but the phasing was good and the surface cyclone was strong enough for the rapid deepening. During the intensification phase the trough grew further. A weak secondary cyclone appeared in front of the trough before the interaction with the primary surface cyclone.

When moisture was reduced at a later stage, the cyclone did not vanish completely in the box but lost its diabatically produced low-level PV. In this experiment, the cyclone did not produce a strong ridge and also the phasing was not optimal for interacting with the upper-level wave. The secondary northern cyclone came into a good position and intensified moderately, while the southern part had the most southern track, was detached from the stratospheric PV body and did not intensify.

In a third experiment, the cyclone passed the dry box at an even later stage, just before starting its rapid intensification. This cyclone experienced the largest SLP change in the box but still had the lowest pressure after leaving the box (compared to the other box experiments). Low-level PV did not totally disappear but was sustained south from the cyclone centre outside of the small box. The cyclone was slowed down and missed the optimal position relative to the approaching upper-level trough. But it remained strong enough for a delayed and moderate intensification (compared to the control run).

These COSMO model sensitivity experiments reveal that moisture modifications strongly influence the intensity, track and the propagation speed of this cyclone. Furthermore they significantly influence the lifting of moist air to the tropopause level and the

evolution of the upper-level ridge. As in other DRW case studies, the crucial component for the cyclone intensification was (i) the timing and the position of the low-level cyclone relative to the upper-level trough and (ii) the diabatic modification of the trough structure by the cyclone itself.

Chapter 6

Summary and outlook

This work investigated potential vorticity and moisture in extratropical cyclones. We have addressed the vertical PV distribution in extratropical cyclones and its evolution, and the sources of moisture that contribute to the diabatic PV production in the cyclones, both with a climatological and a numerical modeling approach. Detailed conclusions can be found at the end of each chapter. Here, we shortly want to summarize the main findings and recall the specific question posed in each chapter.

In the first part of this thesis, we have focused on the three ingredients that contribute to cyclone development: a stratospheric PV intrusion at the tropopause, which interacts with a warm anomaly at the surface and intensifies the low-level circulation, and a diabatically produced positive PV anomaly in the lower troposphere, which enhances the interactions between the anomalies at the level of the tropopause and at the surface through reduction of static stability and additional circulation. The structure of these three PV anomalies constituting a PV tower in mature cyclones was for the first time investigated climatologicaly for a large number of cyclones in different extratropical regions. We have calculated vertical profiles of PV anomalies and surface potential temperature anomalies in the centre of cyclones and compared the evolution of the anomalies along the cyclone track for cyclones of different intensities in several regions.

We found that winter (DJF) cyclones of different intensities in western Europe, in the Mediterranean and in the eastern North Pacific vary primarily in terms of the amplitude of the low-level PV anomaly, while the upper-level PV anomalies and the tropopause height are very similar. On the contrary, the variability of the upper-level PV anomaly is larger for eastern North Atlantic cyclones. Western North Pacific and western North Atlantic cyclones vary strongly in all three anomalies. We find the largest upper-level PV anomalies in the eastern North Pacific and western North Atlantic. The low-level PV anomalies are the largest in the western parts of both oceans and the eastern North Pacific. The highest values of surface θ anomalies appear in the western parts of the oceans, but the variability of this variable is the highest for cyclones around Greenland and Alaska.

The most intense cyclones in the western North Atlantic and western and eastern North Pacific undergo the strongest development during the 24 hours before the time of

maximum intensity. In western Europe, for instance, the strongest development happens at upper levels while the low-level anomaly only slightly increases. This is also the fact for the weakest cyclones in most regions. The surface θ anomalies do not change much during this 24-hour intensification period.

Mediterranean and western European cyclones show on average the least variability in winter, but there are much larger differences between the cyclones of different intensities in these regions in spring, summer and autumn. The numbers of detected cyclones (in particular the strongest cyclones) are lower in other seasons compared to winter, especially in summer. However, the weaker cyclones in summer have higher values of low-level PV anomalies. Also the variability for all Northern Hemisphere cylones is the largest in summer. It is the lowest in winter and spring. The surface θ anomalies in spring are very similar for cyclones of different intensities in most of the regions. The spread of the cyclone characteristics (both PV anomalies) at the beginning of the intensification phase 24 hours before the SLP minimum is much smaller in winter and autumn than in spring and summer. However, the variability in the tropopause height is the largest in autumn (for all 24 hours).

Subsequently, we focused on the diabatically produced PV at lower tropospheric levels, which was found crucial for the explosive deepening in many case studies of very intense extratropical cyclones. The PV tower climatology served as a basis for the investigation of moisture sources for these cyclones. By the means of Lagrangian trajectories and a previously developed moisture source identification method we have identified source regions of moisture, which is relevant for the diabatic production of low-level PV found in the cyclone centre at the time of its maximum intensity.

Moisture uptake fields can be extremely different for individual cyclones (even for cyclones of one intensity class in one region) and depend also on the large scale situation before and during cyclogenesis. The composites do not show all the variability but still provide important information. Moisture uptakes take place up to 9 days prior to the time of PV production, with maxima between 12 and 48 hours. Trajectories on average come from higher levels, descend into the boundary layer and collect moisture a few days before the PV production. Qualitatively, the evolution of meteorological parameters along the trajectories is similar for all regions and intensity classes, implying that condensational processes involved in PV production are the same in all cyclones. However, the number of moist trajectories ending in the diabatic PV production region varies with region and intensity class.

The uptake regions and the quantity of collected moisture are on average larger for intense cyclones. For weaker cyclones, the uptakes are more confined to the vicinity of the cyclones. The uptake regions are much larger for cyclones in the eastern parts of the oceans than for cyclones in the western parts of the oceans. Trajectories involved in PV production in cyclones in the eastern ocean basins spend more time over the ocean and are longer in contact with oceanic moisture sources. We have found no significant continental moisture sources for the investigated winter cyclones.

Finally, a sensitivity study with the COSMO model was performed to investigate the

influence of moisture in the environment of a developing cyclone. Moisture uptake regions were identified with the same Lagrangian method used in the second part of this thesis. In three synthetic model experiments, specific humidity, which was important for the cyclone development at different stages, was eliminated in low-tropospheric boxes around the regions of the oceanic moisture sources. This led to dramatically different outcomes.

Elimination of moisture in the boxes influenced cyclone development on all levels: at the surface, in the lower troposphere and at the tropopause. At the tropopause level, the ridge building downstream of the surface cyclone was weakened due to missing moisture and consequently weaker cross-isentropic lifting of air. The production of low-level PV was inhibited during the passage of the cyclone near or through the dry box. If the cyclone passes the dry box in the early phase of its development, it decays rapidly. When moisture was eliminated at a later stage, the surface cyclone strongly degraded, but still a weak signal remained. The propagation speed of the system was reduced. The weakening and delaying of the low-level cyclone led to a delayed or even missing interaction between the surface cyclone and the upper-level trough and therefore did not allow for a rapid intensification of the system.

This work provides many new insights into the structure of extratropical cyclones and the role of moisture for their development. At the same time, it poses several new question that would deserve further attention.

The variability in the relative importance of the three PV anomalies in determining cyclone intensity may present a significant forecasting issue. The correct representation and evolution of upper-level troughs should be particularly relevant for instance for the eastern North Atlantic; in contrast, diabatic processes in the lower troposphere and the formation of surface temperature anomalies crucially determine cyclone intensity in the western parts of the oceans. Considering the typical scales of these processes, one might hypothesize that cyclone intensity is particularly difficult to predict in the western ocean basins. A verification study would be rewarding to investigate this issue. However, the interaction of all three anomalies introduces the most of nonlinearity and therefore probably presents the largest problem for forecasting. The identification of processes in models that lead to false representations of disturbances contributing to cyclone development would enable improvements of forecasts of intense cyclones.

The Lagrangian diagnostics proved to be very useful in identifying evaporative moisture sources for the production of PV in the cyclone centre. The method could be further applied to identify moisture sources involved in PV production along the fronts or in a warm conveyor belt associated with cyclones.

In this work we focused only on PV structures in the centre of cyclones. The relative contribution of diabatic processes and PV production along the fronts, i.e., outside the cyclone center, to the intensification of cyclones compared to the processes in the cyclone centre itself, is one issue of basic dynamical understanding of cyclogenesis that would also deserve attention and should be further investigated.

Bibliography

Anthes, R. A., Y.-H. Kuo, and J. R. Gyakum, 1983: Numerical simulations of a case of explosive marine cyclogenesis. *Mon. Wea. Rev.*, **111**, 1174–1188.

Arakawa, A. and V. R. Lamb, 1981: A potential enstrophy and energy conserving scheme for the shallow water equations. *Mon. Wea. Rev.*, **82**, 75–96.

Balasubramanian, G. and M. K. Yau, 1994: The effects of convection on a simulated marine cyclone. *J. Atmos. Sci.*, **51**, 2397–2417.

Balasubramanian, G. and M. K. Yau, 1996: The life cycle of a simulated marine cyclone: Energetics and PV diagnostics. *J. Atmos. Sci.*, **53**, 639–653.

Baldwin, D., E.-Y. Hsie, and R. A. Anthes, 1984: Diagnostic studies of a two-dimensional simulation of frontogenesis in a moist atmosphere. *J. Atmos. Sci.*, **41**, 2581–2594.

Bauer, M. and A. D. D. Genio, 2006: Composite analysis of winter cyclones in a GCM: Influence on climatological humidity. *J. Climate*, **19**, 1652–1672.

Bishop, C. H. and A. J. Thorpe, 1994: Potential Vorticity and the electrostatics analogy: Quasi-geostrophic theory. *Quart. J. Roy. Meteor. Soc.*, **120**, 713–731.

Bjerknes, V. F., 1910: Synoptical representation of atmospheric motions. *Quart. J. Roy. Meteor. Soc.*, **36**, 267–286.

Bosart, L. F., 1981: The Presidents' Day snowstorm of 18-19 February 1979: A subsynoptic-scale event. *Mon. Wea. Rev.*, **109**, 1542–1566.

Bosilovich, M. G. and S. D. Schubert, 2002: Water vapour tracers as diagnostics of the regional hydrologic cycle. *J. Hydrometeorol.*, **3**, 149–165.

Bosilovich, M. G., Y. C. Sud, S. D. Schubert, and G. K. Walker, 2003: Numerical simulation of the large-scale North American monsoon water sources. *J. Geophys. Res.*, **108 (D16)**, 8614, doi:10.1029/2002JD003095.

Böttcher, M., 2010: Dynamik diabatischer Rossby-Wellen. Ph.D. thesis, University of Mainz.

Böttcher, M. and H. Wernli, 2011: Life cycle study of a diabatic Rossby wave as a precursor to rapid cyclogenesis in the North Atlantic—dynamics and forecast performance. *Mon. Wea. Rev.*, **139 (6)**, 1861–1878.

Böttcher, M. and H. Wernli, 2012: A 10-year climatology of diabatic rossby-waves in the northern hemisphere. *submitted to Monthly Wea. Rev.*

Browning, K. A., 1986: Conceptual models of precipitation systems. *Weather and Forecasting*, **1**, 23–41.

Brubaker, K. L., P. A. Dirmeyer, A. Sudradjat, B. S. Levy, and F. Bernal, 2001: A 36-yr climatological description of the evaporative sources of warm-season precipitation in the Mississippi River basin. *J. Hydrometeorol.*, **2**, 537–557.

Campins, J., A. Genovés, M. A. Picornell, and A. Jansà, 2011: Climatology of Mediterranean cyclones using the ERA-40 dataset. *Int. J Climatol.*, **31**, 1596–1614.

Carlson, T. N., 1980: Airflow through midlatitude cyclones and the comma cloud pattern. *Mon. Wea. Rev.*, **108**, 1498–1509.

Catto, J. L., L. C. Shaffrey, and K. I. Hodges, 2010: Can climate models capture the structure of extratropical cyclones? *J. Climate*, **23**, 1621–1635.

Chang, E. K. M. and S. Song, 2006: The seasonal cycles in the distribution of precipitation around cyclones in the western North Pacific and Atlantic. *J. Atmos. Sci.*, **63**, 815–839.

Charney, J. G., 1947: The dynamics of long waves in a baroclinic westerly current. *J. Met.*, **4**, 135–162.

Dacre, H. F. and S. L. Gray, 2009: The spatial distribution and evolution characteristics of North Atlantic cyclones. *Mon. Wea. Rev.*, **137**, 99–115.

Davies, H. C., 1976: Time splitting methods for elastic models using forward time schemes. *Quart. J. Roy. Meteor. Soc.*, **102**, 405–418.

Davies, H. C., C. Schär, and H. Wernli, 1991: The palette of fronts and cyclones within a baroclinic wave development. *J. Atmos. Sci.*, **48**, 1666–1689.

Davis, C. A., 1992: A potential-vorticity diagnosis of the importance of initial structure and condensational heating in observed extratropical cyclogenesis. *Mon. Wea. Rev.*, **120**, 2409–2428.

Davis, C. A. and K. A. Emanuel, 1991: Potential vorticity diagnostics of cyclogenesis. *Mon. Wea. Rev.*, **119**, 1929–1953.

Davis, C. A., E. D. Grell, and M. A. Shapiro, 1996: The balanced dynamical nature of a rapidly intensifying oceanic cyclone. *Mon. Wea. Rev.*, **124**, 3–26.

Dee, D. P. and Coauthors, 2011a: The ERA-Interim reanalysis: configuration and performance of the data assimilation system. *Quart. J. Roy. Meteor. Soc.*, **137**, 553–597.

Dee, D. P., E. Källén, A. J. Simmons, and L. Haimberger, 2011b: Comments on "Reanalyses suitable for characterizing long-term trends". *Bull. Amer. Meteor. Soc.*, **90**, 65–70.

Dee, D. P. and S. Uppala, 2009: Variational bias correction of satellite radiance data in the ERA-Interim reanalysis. *Quart. J. Roy. Meteor. Soc.*, **135**, 1830–1841.

Deveson, A. C. L., K. A. Browning, and T. D. Hewson, 2002: A classification of FASTEX cyclones using a height-attributable quasi-geostrophic vertical-motion diagnostic. *Quart. J. Roy. Meteor. Soc.*, **128**, 93–117.

Dickinson, M. J., L. F. Bosart, W. E. Bracken, G. J. Hakim, D. M. Schultz, M. A. Bedrick, and K. R. Tyle, 1997: The march 1993 Superstorm cyclogenesis: Incipient phase synoptic- and convective-scale flow interaction and model performance. *Mon. Wea. Rev.*, **125**, 3041–3072.

Dirmeyer, P. A. and K. L. Brubaker, 1999: Contrasting evaporative moisture sources during the drought of 1988 and the flood of 1993. *J. Geophys. Res.*, **104 (D16)**, 19 383–19 397.

Doms, G. and Coauthors, 2005: A description of the nonhydrostatic regional model LM. Part II: Physical parametrization. Tech. rep., Consortium for Small-Scale Modelling (COSMO).

Doms, G. and U. Schättler, 2002: A description of the nonhydrostatic regional model LM. Part I: Dynamics and numerics. Tech. rep., Consortium for Small-Scale Modelling (COSMO).

Drumond, A., R. Nieto, R. M. Trigo, T. Ambrizzi, and E. Souza, 2010: A Lagrangian identification of the main sources of moisture affecting northeastern brazil during its pre-rainy and rainy seasons. *PLoS ONE*, **5 (6)**, e11205, doi: 10.1371/journal.pone.001120.

Dudhia, J., 1993: A nonhydrostatic version of the Penn State-NCAR mesoscale model:Validation tests and simulations of an Atlantic cyclone and cold front. *Mon. Wea. Rev.*, **121**, 1493–1513.

Eady, E. T., 1949: Long waves and cyclone waves. *Tellus*, **1**, 33–52.

ECMWF, 2007: IFS documentation cy31r1. Tech. rep., European Centre for Medium-Range Weather Forecasts, Shinfield Park, U.K. [Available online at http://www.ecmwf.int/research/ifsdocs/CY31r1.].

Emanuel, K. A., M. Fantini, and A. J. Thorpe, 1987: Baroclinic instability in an environment of small stability to slantwise moist convection. Part I: Two-dimensional models. *J. Atmos. Sci.*, **44**, 1559–1573.

Ertel, H., 1942: Ein neuer hydrodynamscher wirberlsatz. *Meteorol. Zeitschr.*, **59**, 271–281.

Farrel, B. F., 1982: The initial growth of disturbances in a baroclinic flow. *J. Atmos. Sci.*, **39**, 1663–1686.

Farrel, B. F., 1984: Modal and non-modal baroclinic waves. *J. Atmos. Sci.*, **41**, 668–673.

Fehlmann, R., 1997: Dynamics of seminal pv elements. Ph.D. thesis, ETH Zürich.

Field, P. R. and R. Wood, 2007: Precipitation and cloud structure in midlatitude cyclones. *J. Climate*, **20**, 233–254.

Grams, C. M., et al., 2011: The key role of diabatic processes in modifying the upper-tropospheric wave guide: a North Atlantic case-study. *Quart. J. Roy. Meteor. Soc.*, **137**, 2174–2193, doi:10.1002/qj.891.

Gray, S. L. and H. F. Dacre, 2006: Classifying dynamical forcing mechanisms using a climatology of extratropical cyclones. *Quart. J. Roy. Meteor. Soc.*, **132**, 1119–1137.

Gulev, S. K., O. Zolina, and S. Grigoriev, 2001: Extratropical cyclone variability in the Northern Hemisphere from the NCEP/NCAR reanalysis data. *Climate Dyn.*, **17**, 795–809.

Gyakum, J. R., 1983a: On the evolution of the QE II storm. I: Synoptic aspects. *Mon. Wea. Rev.*, **111**, 1137–1155.

Gyakum, J. R., 1983b: On the evolution of the QE II storm. II: Dynamic and thermodynamic structure. *Mon. Wea. Rev.*, **111**, 1156–1173.

Gyakum, J. R., P. J. Roebber, and T. A. Bullock, 1992: The role of antecedent surface vorticity development as a conditioning process in explosive cyclone intensification. *Mon. Wea. Rev.*, **120**, 1465–1489.

Harrold, T. W., 1973: Mechanisms influencing the distribution of precipitation within baroclinic disturbances. *Quart. J. Roy. Meteor. Soc.*, **99**, 232–251.

Hoskins, B. J. and P. Berrisford, 1988: A potential vorticity perspective of the storm of 15-16 October 1987. *Weather*, **43**, 122–129.

Hoskins, B. J. and K. I. Hodges, 2002: New perspectives on the Northern Hemisphere winter storm tracks. *J. Atmos. Sci.*, **59**, 1041–1061.

Hoskins, B. J., M. E. McIntyre, and A. W. Robertson, 1985: On the use and significance of isentropic potential vorticity maps. *Quart. J. Roy. Meteor. Soc.*, **111**, 877–946.

Hoskins, B. J. and N. V. West, 1979: Baroclinic waves and frontogenesis. Part II: Uniform potential vorticity jet flows - cold and warm fronts. *J. Atmos. Sci.*, **36**, 1663–1680.

Hsie, E.-Y., R. A. Anthes, and D. Keyser, 1984: Numerical simulation of frontogenesis in a moist atmosphere. *J. Atmos. Sci.*, **41**, 2686–2700.

Huo, Z., D.-L. Zhang, and J. R. Gyakum, 1999: Interaction of potential vorticity anomalies in extratropical cyclogenesis. Part I: Static piecewise inversion. *Mon. Wea. Rev.*, **127**, 2546–2561.

James, P., A. Stohl, N. Spichtinger, S. Eckhardt, and C. Forster, 2004: Climatological aspects of the extreme European rainfall of August 2002 and a trajectory method for estimating the associated evaporative source regions. *NHESS*, **4**, 733–746.

Kessler, E., 1969: *On distribution and continuity of water substance in atmospheric circulations*. No. 32 in Meteorol. Monogr. Vol. 10, American Meteorological Society, Boston.

Kuo, Y.-H., J. R. Gyakum, and Z. Guo, 1995: A case of rapid continental mesoscale cyclogenesis. Part I: Model sensitivity experiments. *Mon. Wea. Rev.*, **123**, 970–997.

Kuo, Y.-H., M. A. Shapiro, and E. G. Donall, 1991: The interaction between baroclinic and diabatic processes in a numerical simulation of a rapidly intensifying extratropical marine cyclone. *Mon. Wea. Rev.*, **119**, 368–384.

Lambaerts, J., G. Lapeyre, and V. Zeitlin, 2012: Moist versus dry baroclinic instability in a simplified two-layer atmospheric model with condensation and latent heat release. *J. Atmos. Sci.*, **69**, 1405–1426.

Lim, E.-P. and I. Simmonds, 2007: Southern Hemisphere winter extratropical cyclone characteristics and vertical organization observed with the ERA-40 data in 1979-2001. *J. Climate*, **20**, 2675–2690.

Mak, M., 1982: On moist quasi-geostrophic baroclinic instability. *J. Atmos. Sci.*, **39**, 2028–2037.

Mak, M. and P. R. Bannon, 1984: Frontogenesis in a moist semigeostrophic model. *J. Atmos. Sci.*, **41**, 3485–3500.

Manabe, S., 1956: On the contribution of heat released by condensation to the change in pressure pattern. *J. Meteorol. Soc. Jpn*, **34**, 308–320.

Martin, J. E., 2006: *Mid-latitude atmospheric dynamics: A first course*. John Wiley & Sons.

Mass, C. and B. Dotson, 2010: Major extratropical cyclones of the Northwest United States: historical review, climatology, and synoptic environment. *Mon. Wea. Rev.*, **138**, 2499–2527.

Massacand, A., H. Wernli, and H. C. Davies, 1998: Heavy precipitation on the alpine southside: An upper-level precursor. *Geophys. Res. Lett.*, **25 (9)**, 1435–1438, doi:10.1029/98GL50869.

Moore, R. W. and M. T. Montgomery, 2004: Reexamining the dynamics of of short-scale, diabatic Rossby waves and their role in midlatitude cyclogenesis. *J. Atmos. Sci.*, **61**, 754–768.

Moore, R. W. and M. T. Montgomery, 2005: Analysis of an idealized, three-dimensional diabatic Rossby vortex: A coherent structure of the moist baroclinic atmosphere. *J. Atmos. Sci.*, **62**, 2703–2725.

Moore, R. W., M. T. Montgomery, and H. C. Davies, 2008: The integral role of a diabatic Rossby vortex in a heavy snowfall event. *Mon. Wea. Rev.*, **136**, 1878–1897.

Nieto, R., L. Gimeno, D. Gallego, and R. M. Trigo, 2007: Contributions to the moisture budget of airmasses over Iceland. *Meteor. Zeits.*, **16 (1)**, 37–44, doi: 10.1127/0941-2948/2007/0176.

Nieto, R., L. Gimeno, and R. M. Trigo, 2006: A Lagrangian identification of major sources of Sahel moisture. *Geophys. Res. Lett.*, **33**, L18707, doi:10.1029/2006GL027232.

Numaguti, A., 1999: Origin and recycling processes of precipitating water over the Eurasian continent: Experiments using an atmospheric general circulation model. *J. Geophys. Res.*, **104**, 1957–1972.

Parker, D. J. and D. J. Thorpe, 1995: Conditional convective heating in a baroclinic atmosphere: A model of convective frontogenesis. *J. Atmos. Sci.*, **52**, 1699–1711.

Petterssen, S. and S. J. Smebye, 1971: On the development of the extratropical cyclones. *Quart. J. Roy. Meteor. Soc.*, **97**, 457–482.

Pfahl, S. and H. Wernli, 2008: Air parcel trajectory analysis of stable isotopes in water vapor in the eastern Mediterranean. *J. Geophys. Res.*, **113**, D20104, doi: 10.1029/2008JD009839.

Raible, C. C., P. M. Della-Marta, C. Schwierz, H. Wernli, and R. Blender, 2008: Northern Hemisphere extratropical cyclones: A comparison of detection and tracking methods and different reanalyses. *Mon. Wea. Rev.*, **136**, 880–897.

Reale, O., L. Feudale, and B. Turato, 2001: Evaporative moisture sources during a sequence of floods in the Mediterranean region. *Geophys. Res. Lett.*, **28 (10)**, 2085–2088, doi:10.1029/2000GL012379.

Reed, R. J., 1990: Advances in knowledge and understanding of extratropical cyclones during the past quarter century: an overview. *Extratropical cyclones. The Erik Palmen Memorial Volume.*, C. Newton and E. O. Holopainen, Eds., American Meteorological Society, Boston, 27–45.

Reed, R. J., M. T. Stoelinga, and Y.-H. Kuo, 1992: A model-aided study of the origin and evolution of the anomalously high potential vorticity in the inner region of a rapidly deepening marine cyclone. *Mon. Wea. Rev.*, **120**, 893–913.

Reeves, H. D. and G. M. Lackmann, 2004: An investigation of the influence of latent heat release on cold-frontal motion. *Mon. Wea. Rev.*, **132**, 2864–2881.

Riviere, G., P. Arbogast, K. Maynard, and A. Joly, 2010: The essential ingredients leading to the explosive growth stage of the European wind storm *lothar* of Christmas 1999. *Quart. J. Roy. Meteor. Soc.*, **136**, 638–652, doi:10.1002/qj.585.

Riviere, G. and A. Joly, 2006: Role of the low-frequency deformation field on the explosive growth of extratropical cyclones at the jet exit. Part II: Baroclinic critical region. *J. Atmos. Sci.*, **63**, 1982–1995.

Roebber, P. J., 1984: Statistical and updated climatology of explosive cyclones. *Mon. Wea. Rev.*, **112**, 1577–1589.

Rogers, E. and L. F. Bosart, 1986: An investigation of explosively deepening oceanic cyclones. *Mon. Wea. Rev.*, **114**, 702–718.

Rossa, A. M., H. Wernli, and H. C. Davies, 2000: Growth and decay of an extratropical cyclone's PV-tower. *Meteorol. Atmos. Phys.*, **73**, 139–156.

Rudeva, I., 2008: On the relation of the number of extratropical cyclones to their sizes. *Izvestiya, Atmospheric and Oceanic Physics*, **44**, 273–278.

Rudeva, I. and S. K. Gulev, 2007: Climatology of cyclone size characteristics and their changes during the cyclone life cycle. *Mon. Wea. Rev.*, **135**, 2568–2587.

Rudeva, I. and S. K. Gulev, 2011: Composite analysis of North Atlantic extratropical cyclones in NCEP-NCARreanalysis data. *Mon. Wea. Rev.*, **139**, 1419–1446.

Sanders, F. and J. R. Gyakum, 1980: Synoptic-dynamic climatology of the "bomb". *Mon. Wea. Rev.*, **108**, 1589–1606.

Schär, C. and H. Wernli, 1993: Structure and evolution of an isolated semi-geostrophic cyclone. *Quart. J. Roy. Meteor. Soc.*, **119**, 57–90.

Schubert, M., J. Perlwitz, R. Blender, K. Fraedrich, and F. Lunkeit, 1998: North Atlantic cyclones in CO2-induced warm climate simulations: frequency, intensity, and tracks. *Climate Dyn.*, **14**, 827–837.

Shaw, W. N., 1903: The meteorological aspects of the storm of february 26-27, 1903. *Quart. J. Roy. Meteor. Soc.*, **29**, 233–262.

Simmonds, I. and K. Keay, 2000: Mean Southern Hemisphere extratropical cyclone behavior in the 40-year NCEP-NCAR reanalysis. *J. Climate*, **13**, 873–885.

Simmonds, I. and X. Wu, 1993: Cyclone behaviour response to changes in winter southern hemisphere sea-ice concentration. *Quart. J. Roy. Meteor. Soc.*, **119**, 1121–1148.

Sodemann, H., C. Schwierz, and H. Wernli, 2008: Interannual variability of Greenland winter precipitation sources: Lagrangian moisture diagnostic and North Atlantic Oscillation influence. *J. Geophys. Res.*, **113**, D03107, doi:10.1029/2007JD008503.

Sodemann, H. and A. Stohl, 2009: Asymmetries in the moisture origin of Antarctic precipitation. *Geophys. Res. Lett.*, **36**, L22803, doi:10.1029/2009GL040242.

Sodemann, H., H. Wernli, and C. Schwierz, 2009: Sources of water vapour contributing to the Elbe flood in August 2002 - A tagging study in a mesoscale model. *Quart. J. Roy. Meteor. Soc.*, **135**, 205–223, doi:10.1002/qj.374.

Sodemann, H. and E. Zubler, 2010: Seasonal and inter-annual variability of the moisture sources for Alpine precipitation during 1995–2002. *Int. J Climatol.*, **30**, 947–961, doi:10.1002/joc.1932.

Steppeler, J., G. Doms, U. Schättler, H.-W. Bitzer, A. Gassmann, U. Damrath, and G. Gregoric, 2003: Meso-gamma scale forecasts using the non-hydrostatic model LM. *Meteorol. Atmos. Phys.*, **109**, 18–36.

Stoelinga, M. T., 1996: A potential vorticity-based study of the role of diabatic heating and friction in a numerically simulated baroclinic cyclone. *Mon. Wea. Rev.*, **124**, 849–874.

Stohl, A., C. Forster, and H. Sodemann, 2008: Remote sources of water vapor forming precipitation on the Norwegian west coast at 60° N - a tale of hurricanes and an atmospheric river. *J. Geophys. Res.*, **113**, D05102, doi: 10.1029/2007JD009006.

Stohl, A. and P. James, 2004: A Lagrangian analysis of the atmospheric branch of the global water cycle. Part I: Method description, validation, and demonstration for the August 2002 flooding in Central Europe. *J. Hydrometeorol.*, **5 (8)**, 656–678.

Stohl, A. and P. James, 2005: A Lagrangian analysis of the atmospheric branch of the global water cycle. Part II: Moisture transport between Earth's ocean basins and river catchments. *J. Hydrometeorol.*, **6 (12)**, 961–984.

Thorncroft, C. D., B. J. Hoskins, and M. E. McIntyre, 1993: Two paradigms of baroclinic-wave life-cycle behaviour. *Quart. J. Roy. Meteor. Soc.*, **119**, 17–55.

Thorpe, A. J., 1986: Synoptic scale disturbances with circular symmetry. *Mon. Wea. Rev.*, **114**, 1384–1389.

Tiedtke, M., 1989: A comprehensive mass flux scheme for cumulus parameterization in large-scale models. *Mon. Wea. Rew.*, **117**, 1779–1800.

Trigo, I. F., T. D. Davies, and G. R. Bigg, 1999: Objective climatology of cyclones in the Mediterranean region. *J. Climate*, **12**, 1685–1696.

Turato, B., O. Reale, and F. Siccardi, 2004: Water vapor sources of the October 2000 Piedmont flood. *J. Hydrometeorol.*, **5**, 693–712.

Uccellini, L. W., 1990: Processes contributing to the rapid development of extratropical cyclones. *Extratropical cyclones. The Erik Palmen Memorial Vol-*

ume., C. Newton and E. O. Holopainen, Eds., American Meteorological Society, Boston, 81–105.

Uccellini, L. W., R. A. Petersen, K. F. Brill, P. J. Kocin, and J. J. Tuccillo, 1987: Synergistic interactions between an upper-level jet streak and diabatic processes that influence the development of a low-level jet and a secondary coastal cyclone. *Mon. Wea. Rev.*, **115**, 2227–2261.

Wang, C.-C. and J. C. Rogers, 2001: A composite study of explosive cyclogenesis in different sectors of the North Atlantic. Part I: Cyclone structure and evolution. *Mon. Wea. Rev.*, **129**, 1481–1499.

Warrenfeltz, L. L. and R. L. Elsberry, 1989: Superposition effects in rapid cyclogenesis - linear model studies. *J. Atmos. Sci.*, **46**, 789–802.

Wernli, H., 1997: A lagrangian-based analysis of extratropical cyclones. II: A detailed case-study. *Quart. J. Roy. Meteor. Soc.*, **123**, 1677–1706.

Wernli, H. and H. Davies, 1997: A lagrangian-based analysis of extratropical cyclones. I: The method and some applications. *Quart. J. Roy. Meteor. Soc.*, **123**, 467–489.

Wernli, H., S. Dirren, M. A. Liniger, and M. Zillig, 2002: Dynamical aspects of the life cycle of the winter storm 'Lothar' (24-26 December 1999). *Quart. J. Roy. Meteor. Soc.*, **128**, 405–429.

Wernli, H., R. Fehlmann, and D. Lüthi, 1998: The effect of barotropic shear on upper-level induced cyclogenesis: semigeostrophic and primitive equation numerical simulations. *J. Atmos. Sci.*, **55**, 2080–2094.

Wernli, H. and C. Schwierz, 2006: Surface cyclones in the ERA-40 dataset (1958-2001). Part I: Novel identification method and global climatology. *J. Atmos. Sci.*, **63**, 2486–2507.

Whitaker, J. S. and C. A. Davis, 1994: Cyclogenesis in a saturated environment. *J. Atmos. Sci.*, **51**, 889–907.

Whitaker, J. S., L. W. Uccellini, and K. F. Brill, 1988: A model-based diagnostic study of the rapid development phase of the Presidents' Day Cyclone. *Mon. Wea. Rev.*, **116**, 2337–2365.

Whittaker, L. M. and L. H. Horn, 1984: Northern Hemisphere extratropical cyclone activity for four mid-season months. *J. Climatol.*, **4**, 297–310.

Wicker, L. J. and W. C. Skamarock, 2002: Time splitting methods for elastic models using forward time schemes. *Mon. Wea. Rev.*, **130**, 2088–2097.

Winschall, A., S. Pfahl, H. Sodemann, and H. Wernli, 2011: Impact of North Atlantic evaporation hot spots on southern Alpine heavy precipitation events. *Quart. J. Roy. Meteor. Soc.*, doi:10.1002/qj.987, published online.

Xu, Q., 1988: Baroclinic waves and frontogenesis with an embedded zone of small moist symmetric stability. *Quart. J. Roy. Meteor. Soc.*, **114**, 1221–1251.

Xu, Q., 1990: Cold and warm frontal circulations in an idealized moist semi-geostrophic baroclinic wave. *J. Atmos. Sci.*, **47**, 2337–2352.

Acknowledgements

Aus Datenschutzgründen kann die Danksagung hier nicht komplett veröffentlicht werden.

This work was done within the Research Unit PANDOWAE (Forschergruppe - FOR896) sponsored by the German Research Council (Deutsche Forschungsgemeinschaft, DFG).